MICROSTRUCTURAL INFLUENCES

ON

FORMABILITY AND FRACTURE OF ALUMINUM ALLOY 2036

by

© Ian R. Dover, B.Sc.

A Thesis

Submitted to the School of Graduate Studies

in Partial Fulfillment of the Requirements

for the Degree

Master of Engineering

McMaster University

October, 1979

MICROSTRUCTURAL INFLUENCES

ON

FORMABILITY AND FRACTURE OF ALUMINUM ALLOY 2036

MASTER OF ENGINEERING
(Metallurgy and Materials Science)

McMASTER UNIVERSITY
Hamilton, Ontario

TITLE: Microstructural Influences on Formability and Fracture of Aluminum Alloy 2036

AUTHOR: Ian R. Dover, B.Sc. (Met.) (University of Queensland, Australia)

SUPERVISORS: Professor J. D. Embury
Professor J. L. Duncan

NUMBER OF PAGES: xi, 160

ABSTRACT

The mechanical deformation behaviour of the age-hardenable aluminum alloy 2036 was used to study the effects of differences in the microstructure due to (a) variations in commercial processing for one ageing condition (T4), and (b) variations in the ageing condition for one processing route. The effects of loading along different proportional straining paths have been considered with the aim of establishing correlations between the mechanical properties and formability, and for the case of (a) above, some rationalisation of selected press performance in terms of particular microstructural constituents has also been attempted. Changes in the fracture behaviour due to both (a) and (b) above are discussed. These changes emphasise the need to consider the role of fracture events in forming operations and their dependence on microstructure.

ACKNOWLEDGEMENTS

The author wishes to express his sincere thanks to all those whose help enabled completion of this thesis. In particular, the guidance and encouragement of Professors J.D. Embury and J.L. Duncan have been greatly appreciated. So too is the valuable academic and social input provided by the Rude Mechanicals research group during the author's time at McMaster.

Financial support from the Alcoa Foundation and the Natural Sciences and Engineering Research Council of Canada is gratefully acknowledged, and appreciation is directed towards the members of the A.D.D.R.G. for the supply of the alloy 2036 and for valuable discussions related to aspects of this study. Help provided by Alcoa and Alcan in the form of additional materials and the use of specific testing equipment is also much appreciated.

The author is also indebted to Horst Neumayer and Tom Bryner for their help in experimental details and photography, to Professor T.R. Ramachandran for his help with the transmission electron microscopy, and especially to Susan Saracini for her expert typing under pressure.

It is impossible to express the gratitude felt towards all the friends in Canada, and family in Australia whose support and tolerance have resulted in such an enjoyable time at McMaster. Thanks.

TABLE OF CONTENTS

Page

LIST OF FIGURES

LIST OF TABLES

CHAPTER 1

INTRODUCTION

The complexity of commercial aluminum alloys is such that studies of the influence of microstructural parameters upon mechanical properties have been restricted mainly to methods whereby controlled changes are made to chemistry and/or heat treatment in order to discern subsequent effects on some parameter such as the initial flow stress or some measure of the fracture toughness. As the microstructures of commercial alloys involve constituents associated with solidification and a sequence of solid state reactions, it is common to try to reduce the problem to one involving only those structural aspects which can be carefully controlled through the use of model systems based on high purity alloys. Thus, it is of value to try to link the basic concepts elucidated in the model systems to more complex engineering materials.

The current work was designed to elucidate some of the factors which determine the formability of one of the higher strength age-hardenable sheet aluminum alloys presently in use by some of the auto-makers as a material for body panel construction. In this introductory section the nature of the engineering problem of press formability will be presented, details of the materials utilised in the study will be given, and the objectives of the research project will be defined.

It is obviously impossible to attempt to correlate specific microstructural features directly to the formability of sheet material, however, it is sometimes possible to determine the influence of the microstructural features on definable mechanical parameters which can subsequently be correlated with some aspect of the formability. This approach is pursued further in this thesis in regard to the quench sensitivity of the 2036 alloy.

1.1 Engineering Problem

This study was instigated as a result of a production problem experienced by one of the auto-makers during press forming of a deck lid outer panel utilising the aluminum alloy 2036-T4 of nominal gauge 1 mm and with an organic millbond coating one side as an aid to handling and lubrication. It was found that the three "lots" (different sources) of this alloy which were available in the stamping plant exhibited different degrees of success in forming the component. These differences were observed after all the die-related parameters had been adjusted to achieve optimum production for each lot. For one lot, successful panels were achieved virtually all the time; for a second lot the success rate was approximately 80%, while the third lot managed a figure of only about 20%. It must be emphasised that the differentiation between materials on the basis of press performance does not represent a rigorous scientific differentiation, however, the objective of the present study was to elucidate some aspects of the formability of heat treatable aluminum alloys and to establish a more analytical and microstructural explanation of some possible causes why the differences in press performance were observed.

A view of a typical failure is shown in Figure 1-1. The small circular depression represents the keyhole in the final part, so it is

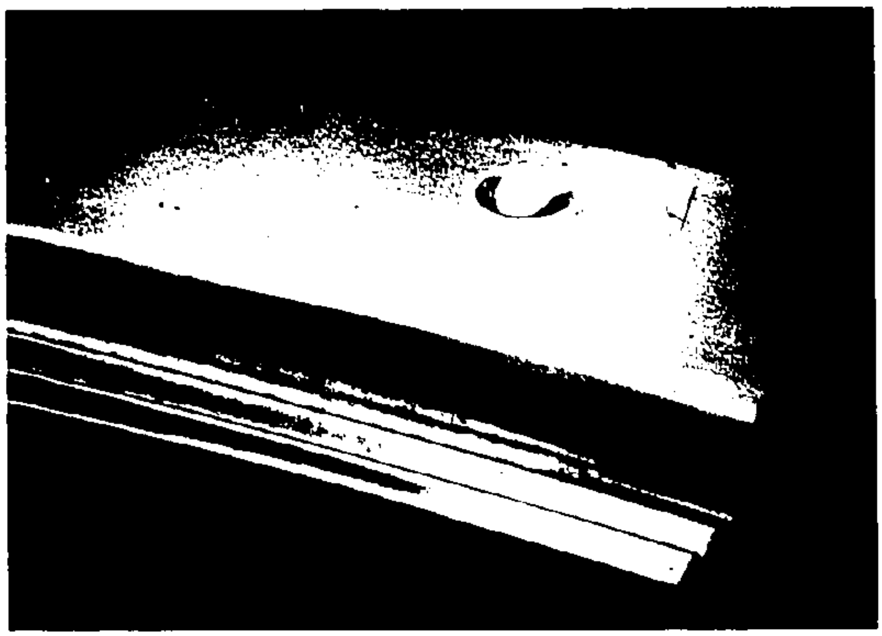

Figure 1-1 Failure of the deck lid panel during press forming.

seen that the failure has occurred along the rear side-wall of the stamping. Metal in the region of failure has been drawn into the die cavity through a series of draw-beads and is then stretched towards the punch corner across the trim line. Thus, the material in question has suffered a complex strain history consisting of reverse bending followed by plane strain tension. In some of the parts, failure also occurred along the side of the component, again after bending plus plane strain history. It is important to note that this type of failure is not one associated with the formation of a local neck in a region which is to be aesthetically attractive in the final panel, but one which depends solely on whether or not the material tears.

1.2 Materials

Aluminum alloy 2036 is a relatively new member of the 2XXX (Al-Cu) series of alloys and is used specifically for sheet forming applications in the T4 temper. The T4 designation indicates that the material has been solution treated, quenched and naturally aged to a stable condition. Chemical compositions derived for the three lots of 2036 are given in Table 1-1, together with the nominal composition of the material. Throughout this work, the following designations will be applied to the 2036 alloys used: material G signifies the material with good formability; material M is marginal, while material P indicates the material with poor formability.

Commercial production of 2036-T4 involves a series of operations outlined schematically in Figure 1-2. Up to the solution treatment stage, the material follows the route of strain-hardenable sheet

Table 1-1

Compositions of 2036 Al Alloys*

Element	Material G	Material M	Material P	Nominal Composition†
Cu	2.33	2.63	2.66	2.2 - 3.0
Mg	0.37	0.50	0.52	0.3 - 0.6
Fe	0.26	0.44	0.48	0.5 Max.
Si	0.32	0.38	0.36	0.5 Max.
Mn	0.24	0.18	0.25	0.10 - 0.40
Zn	0.04	0.15	0.18	0.25 Max.
Ti	0.060	0.019	0.018	0.15 Max.

* A.D.D.R.G. Aluminum Cooperative Group Averages

† Aluminum Association Standards

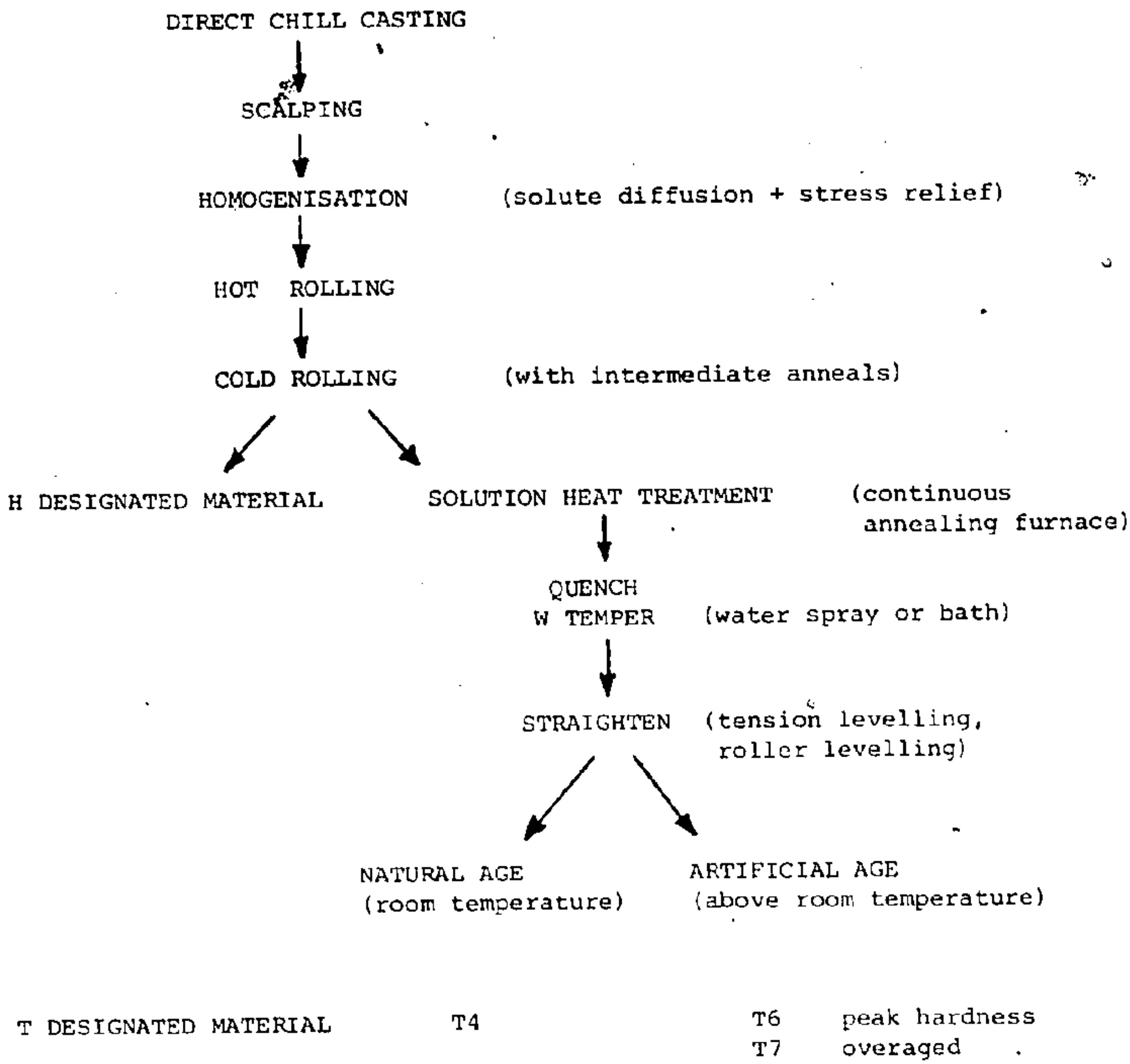

Figure 1-2 Schematic representation of the processing routes for sheet aluminum alloys.

alloy production; the solution treatment generally occurs in a continuous annealing furnace where the sheet is subjected to a temperature of 500°C (Aluminum Association, 1976) for a time of the order of minutes. Upon exiting this furnace a rapid quench is applied by either water spray or water tank, a straightening operation (usually tension or roller levelling) to remove warpage resulting from the quench follows, and the metal is then coiled and naturally aged before shipment. Natural ageing is essentially complete in a period of about two weeks. Further, the application of the millbond coating before the metal is received by the customer involves temperatures of approximately 200°C for 1/2 to 1 minute. The processing routes for each of the three lots of 2036-T4 are not known in detail beyond that described above; hence, the possibility exists for the variation of many of the processing parameters subsequent to the control of chemical composition. Reference to the different stages in processing will be made throughout this thesis when obvious correlations can be drawn between material properties or microstructure and material processing.

1.3 Objectives

The primary objective of the present study was to elucidate the factors which lead to the variability in press performance of the 2036 alloys. Basic tensile properties were clearly insufficient to explain the differences in forming behaviour, otherwise, quality control by the producer and customer would have revealed a problem before production of the body panel began. The dependence of material response upon the mode of deformation, i.e., the deformation path, was highlighted by this problem since it was the rigours of the complex forming operation which differentiated the materials on the basis of their success in forming the given component.

As alluded to previously, the success or failure of production of the deck lid depended upon the operative failure criterion. In this respect, it was thought that the behaviour of the materials at large strains approaching fracture might discriminate between the lots, and hence the hydraulic bulge test was used to extend the study of the mechanical response to strains unattainable in uniaxial tension. Work hardening characteristics at these strains were examined for the three lots of material. In addition, the influence of the fracture event upon formability was considered via the representation of a fracture map in strain space, this supplementing the approximate forming limit diagrams which were also determined.

The effects of microstructural differences on some basic aspects of formability were simulated through the materials' response to simple bending deformation and by fractographic features characteristic of different loading trajectories. Controlled modifications to one aspect of the microstructure, namely the extent of grain boundary precipitation, were effected for the T4 temper and the subsequent change in bendability was discussed in relation to commercial production practices.

Heat treatments designed to place one of the materials in a range of ageing conditions were established and the mechanical behaviour in uniaxial and equi-biaxial tension was studied as a function of ageing condition. The purpose of this was to determine work hardening characteristics in the strain regime beyond that of the uniaxial tension test.

CHAPTER 2

LITERATURE REVIEW

The purpose of this chapter is to provide a broad overview of the various topics covered in the thesis and to present a review of those topics whose theoretical and experimental bases are necessary for discussion of many of the results. Clearly, many of the topics are reviewed in depth in the existing literature and in the interests of brevity, reference will be made to the major reviews and texts where possible.

2.1 Physical Metallurgy

Wilm (1911) discovered that good combinations of strength and ductility were obtained from alloys of aluminum with 3-5% Cu, 0.5-1.0% Mg and 0.8% Mn: these age-hardening alloys became known as Duralumins and since that time, the development of Al-Cu alloys based on this and other compositions has occupied much of the history of aluminum alloys. The alloy 2036 is a relative newcomer to this list, and, as noted in Chapter 1, contains a number of elements other than Cu. Some of these are specific alloying additions (Mg, Mn, Ti), some are incidental impurities present in the refined alumina (Fe, Si), while some result from the utilisation of scrap material in the commercial production sequence (Fe, Zn). Because of the complexity of the commercial alloys, a discussion of their detailed metallurgy is beyond the scope of this review. Examples of the phases which can form in the Al-Cu-Fe-Mg-Mn-Si system are shown in Table 2-1, from Mondolfo (1976), who also provides details and references for the main binary, ternary and quaternary reactions contained within the commercial systems. Van Horn (1967) and Van Lancker (1967) also provide good reviews of the metallurgy of aluminum alloys.

To reduce the complexity of the commercial alloys, it is advantageous to consider separate types of reactions which produce intermetallic phases during solidification, homogenisation treatments, and precipitation of metastable and stable phases from solid solution during ageing processes. These reactions produce particles of widely differing sizes and in the final wrought product, sheet in this case, the range of sizes associated with each reaction is indicated in Table 2-2.

2.1.1 Solidification

Details on the solidification reactions in aluminum alloys may be found in the references cited above, together with Flemings and Mehrabian (1969) and Sperry (1955). It is during solidification that the Fe, Si and Mn-rich phases are formed, such as $Al_{15}(Fe\ Mn)_3Si_2$ and $Al_6(Fe\ Mn)$, which are virtually insoluble in the α-Al matrix and hence are unaffected by subsequent thermal treatments. The stoichiometry of these Al-Fe-Si-Mn phases are affected mainly by processing variables such as melt chemistry and solification rate, and it is likely that some non-equilibrium phases will be present. Soluble phases, such as $Cu\ Al_2$ and $Cu\ Mg\ Al_2$ may also be formed in the commercial Al-Cu-Mg alloys, the composition of the liquid determining the stoichiometry.

2.1.2 Homogenisation

The precipitation reactions occurring during the homogenisation

Table 2-1

Examples of Phases in the Al-Cu-Fe-Mg-Mn-Si System (after Mondolfo, 1976)

PHASES FORMED IN THE ALUMINUM-COPPER-IRON-MAGNESIUM-MANGANESE-SILICON SYSTEM AND PHASES WITH WHICH THEY CANNOT BE IN EQUILIBRIUM

Phase	*Cannot be in equilibrium*
Al	none
$CuAl_2$	Mg_2Al_3, $CuMg_4Al_6$, $FeAl_3$, $(MgMn)_3Al_{10}$
$FeAl_3$	$CuAl_2$, Si, $FeSiAl_5$, $(CuFeMn)_3Si_2Al_{15}$
Mg_2Al_3	$CuAl_2$, Si, $CuMgAl_2$, $Cu_2Mn_3Al_{20}$, $FeSiAl_5$, Fe_2SiAl_8 (?), $(CuFeMn)_3Si_2Al_{15}$, $Cu_2Mg_8Si_6Al_5$
$MnAl_6$	$CuAl_2$, Si, $(FeMn)Al_6$, Fe_2SiAl_8, $FeSiAl_5$, $(CuFeMn)Al_6$, $FeMg_3Si_6Al_8$
Si	$FeAl_3$, Mg_2Al_3, $MnAl_6$, $(CuFe)Al_6$, $CuMgAl_2$, $CuMg_4Al_6$, $(FeMn)Al_6$, Fe_2SiAl_8, $(MgMn)_3Al_{10}$, $(CuFeMn)Al_6$
$(CuFe)Al_6$	Mg_2Al_3, $MnAl_6$, Si, $(FeMn)Al_6$, $FeSiAl_5$, $(MgMn)_3Al_{10}$, $(CuFeMn)_3Si_2Al_{15}$, $(CuFeMn)Al_6$, $Cu_2Mg_8Si_6Al_5$
Cu_2FeAl_7	$FeAl_3$, Mg_2Al_3, $MnAl_6$, $CuMg_4Al_6$, $Cu_2Mn_3Al_{20}$, Fe_2SiAl_8, $(MgMn)_3Al_{10}$, $FeMg_3Si_6Al_8$, $(CuFeMn)_3Si_2Al_{15}$, $(CuFeMn)Al_6$, $Cu_2Mg_8Si_6Al_5$
$CuMgAl_2$	Mg_2Al_3, Si, Fe_2SiAl_8, $FeSiAl_5$, $(MgMn)_3Al_{10}$, $(CuFeMn)_3Si_2Al_{15}$, $(CuFeMn)Al_6$, $Cu_2Mg_8Si_6Al_5$, $FeMg_3Si_6Al_8$
$CuMg_4Al_6$	$CuAl_2$, Si, Fe_2SiAl_8, $FeSiAl_5$, $(CuFeMn)_3Si_2Al_{15}$, $Cu_2Mg_8Si_6Al_5$, $FeMg_3Si_6Al_8$
$(FeMn)Al_6$	$MnAl_6$, Si, $(CuFe)Al_6$, Cu_2FeAl_7, Fe_2SiAl_8, $FeSiAl_5$, $Cu_2Mg_8Si_6Al_5$, $FeMg_3Si_6Al_8$
Fe_2SiAl_8	Mg_2Al_3, $MnAl_6$, Si, $(CuFe)Al_6$, $CuMgAl_2$, $CuMg_4Al_6$, $Cu_2Mn_3Al_{20}$, $(FeMn)Al_6$, $(MgMn)_3Al_{10}$, $(CuFeMn)_3Si_2Al_{15}$, $(CuFeMn)Al_6$
$FeSiAl_5$	$FeAl_3$, Mg_2Al_3, $MnAl_6$, $(CuFe)Al_6$, $CuMgAl_2$, $CuMg_4Al_6$, $Cu_2Mn_3Al_{20}$, $(FeMn)Al_6$, $(MgMn)_3Al_{10}$, $(CuFeMn)Al_6$, $(CuFeMn)_3Si_2Al_{15}$
$Cu_2Mn_3Al_{20}$	$FeAl_3$, Si, Fe_2SiAl_8, $FeSiAl_5$, $(MgMn)_3Al_{10}$, $FeMg_3Si_6Al_8$, $(CuFeMn)_3Si_2Al_{15}$
$(MgMn)_3Al_{10}$	$CuAl_2$, $FeAl_3$, Si, $(CuFe)Al_6$, Cu_2FeAl_7, $CuMgAl_2$, $Cu_2Mn_3Al_{20}$, Fe_2SiAl_8, $FeSiAl_5$, $(CuFeMn)Al_6$, $Cu_2Mg_8Si_6Al_5$, $FeMg_3Si_6Al_8$, $(CuFeMn)_3Si_2Al_{15}$
Mg_2Si	none
$(CuFeMn)_3Si_2Al_{15}$	$FeAl_3$, Mg_2Al_3, $(CuFe)Al_6$, Cu_2FeAl_7, $CuMgAl_2$, $CuMg_4Al_6$, $(MgMn)_3Al_{10}$, $(CuFeMn)Al_6$
$(CuFeMn)Al_6$	Mg_2Al_3, $MnAl_6$, Si, $(FeMn)Al_6$
$Cu_2Mg_8Si_6Al_5$	Mg_2Al_3, $CuMgAl_2$, $CuMg_4Al_6$, $(MgMn)_3Al_{10}$, $(CuFeMn)_3Si_2Al_{15}$
$FeMg_3Si_6Al_8$	Mg_2Al_3, $MnAl_6$, $CuMgAl_2$, $CuMg_4Al_6$, $(FeMn)Al_6$, $FeSiAl_5$

Table 2-2

Approximate Size Ranges of Second Phase Particles Present in Aluminum Alloys

PARTICLE NAME	HOW FORMED	SIZE
Constituents	Solidification	1 - 30 μm
Dispersoids	Homogenisation of ingots	1000 Å - 0.5 μm
Hardening Precipitates	Low temperature ageing of sheet	20 Å - 1000 Å

treatments involve elements such as Cr, Mn, and Zr, which are added to control recrystallisation during wrought alloy production. These elements have exceedingly low solid solubilities and diffusivities in aluminum (Van Horn, 1967), and consequently, they are retained in solid solution during casting, forming regions of supersaturation at the centres of the primary dendrites (Boyd et al, 1972). During ingot homogenisation, the intermediate precipitates (also known as dispersoids), form in these regions and are considered stable with respect to coarsening or dissolution during subsequent thermal/mechanical processing. Since these precipitates tend to form in the centres of the primary dendrites, their distribution throughout the material can be very non-uniform. This non-uniform distribution persists during further processing and results in microstructural patterns in certain wrought products known as "banding". Examples of the dispersoid particles are

αAlFe(Cr Mn)Si (Munson, 1967),

$\alpha Al_8Mn_2Si_{1.8}$ (Cooper & Robinson, 1966),

Al_3Zr (Ryum, 1969).

The impurity elements (Fe, Si) which form the large constituents on solidification influence the character and distribution of the dispersoids (Boyd et al, 1972). For example, in Cr-bearing alloys, where Fe and Si are present, the dispersoids tend to be α(Al Fe Cr Si), whereas, in high purity alloys, the phase $Al_{18}Cr_2Mg_3$ forms (Holl, 1969).

In summary, to control the character and total distribution of the dispersoid particles, the following factors must be considered:

a) alloy chemistry (minor alloy additions and impurities),

b) solidification conditions (cooling rate, agitation, etc.),

c) diffusivities of minor alloy elements,

d) distribution of constituent particles,

e) ingot homogenisation treatment.

2.1.3 Low Temperature Ageing

The response of both high-purity and commercial Al-Cu alloys to ageing following solution treatment and quenching has been the subject of many investigations (see references listed in Mondolfo (1976), Van Horn (1967), and Van Lancker (1967)). Specifically, the Al-Cu-Mg system, upon which 2036 is based, has been studied by Hardy (1954-55), Silcock (1960-61), Weatherly (1967), and Wilson (1969), among others. In the comercial alloys, the ageing characteristics depend on the Mg and Si contents. At high ratios of Mg:Si, $CuMgAl_2$ produces substantial hardening by ageing at room temperature; in alloys in which this ratio is close to 1.7:1, $CuAl_2$ and, to a limited extent, Mg_2Si harden, and the ageing at room temperature is limited. At lower ratios, $Cu_2Mg_8Si_6Al_5$ together with $CuAl_2$ are the hardening constituents with artificial ageing required for best properties.

In the ternary system Al-Cu-Mg, the main hardening constituent depends on the Cu:Mg ratio, as can be seen from the phase diagram in Figure 2.1. For ratios >8:1, $CuAl_2$ is produced; between 8:1 and 4:1, both $CuAl_2$ and $CuMgAl_2$ are produced; between 4:1 and 1.5:1, $CuMgAl_2$ is the hardening phase. In alloys where hardening is due to the $CuAl_2$, small additions of Mg (0.1%) tend to accelerate the rate of ageing and counteract the retarding effect of Fe (Mondolfo, 1976).

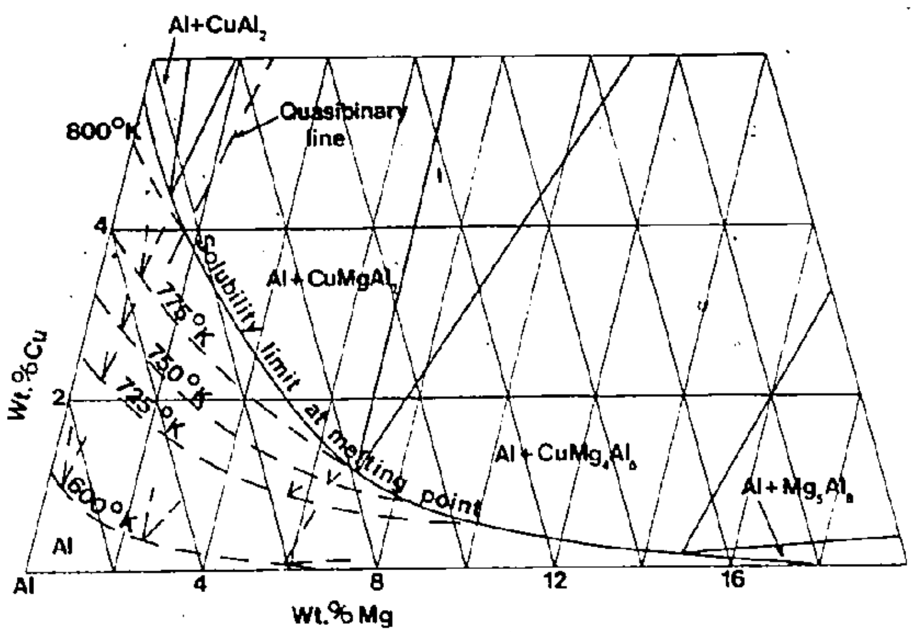

Figure 2-1 Aluminum corner of the Al-Cu-Mg phase diagram showing phase distribution in the solid and solid solubilities at various temperatures.

2.1.4 Alloy 2036

This alloy is quite low in Cu content and very low in Mg compared to most other 2XXX-series alloys, the majority of which are used in aerospace applications. Very little work has been published on the physical metallurgy of 2036. The roles of the different alloying elements are as follows (Beaver, 1978; Lloyd, 1979):

a) Cu and Mg promote hardening by precipitation in the solid state and by solid solution hardening; Cu tends to lower the recrystallisation temperature, especially at higher deformations, while Mg has little effect on the recrystallisation.

b) Mn is added to control recrystallisation and grain growth via the formation of Mn-rich particles during solidification and homogenisation; these particles also affect the plastic deformation behaviour of the final product.

c) Fe and Si are incidental impurities although both influence the ageing response due to the fine precipitates.

d) Ti is added to control grain size during solidification.

e) Zn is also an incidental impurity, but its influence on the properties of 2036 is not known.

Chaturvedi, Chung and Doucette (1979) have studied the effect of thermo-mechanical processing on the properties of 2036 and found that the θ type ($CuAl_2$) of precipitate only occurs. Their work did not involve the naturally aged material so that the structure of the G.P. zones was not identified. The Cu:Mg ratio in these authors' alloy was 5.7:1, suggesting that the additional alloying elements in the commercial material alter the ratios of Cu:Mg which give the phases described previously for the AlCuMg ternary system. The sequence of events which lead to the formation of the equilibrium phase from the supersaturated solid solution has been reviewed well by Kelly and Nicholson (1963). Five structures can be recognised: (1) supersaturated solid solution, (2) G.P.1 zones, (3) G.P.2 zones or θ", (4) θ', and (5) θ or $CuAl_2$.

Development of the aged microstructure proceeds in the sequence given above, but the starting point of the sequence may vary from place to place, depending on the nature of the defects present and the temperature. Hornbogen (1969) suggests that the transition from one metastable phase to the next occurs because the growing particle itself creates the defect which catalyses the formation of a more stable particle. For example, as a θ' particle grows, an increasing number of interfacial dislocations form that finally reach such a density that portions of the interface become noncoherent. As soon as this stage is reached, the conditions for θ nucleation are fulfilled, i.e., the presence of a noncoherent boundary. The same principle applies for the transition $\theta'' \rightarrow \theta'$ in regard to the elastic coherency stresses leading to the formation of a dislocation ring. Thus, grain boundaries, dislocations, and the interfaces of inclusions and dispersoids, as well as sites in the perfect lattice, can be considered as nucleation sites for different phases.

2.1.5 Quench Sensitivity

It has been recognised that quench sensitivity is the result of formation during cooling from the solution heat treatment temperature of coarse non-hardening precipitates that deplete the surrounding matrix of solute and hence inhibit hardening on subsequent ageing. There is also evidence (Kelly and Nicholson, 1963; Embury and Nicholson, 1963), that variation in the rate of quenching has a marked influence on the hardening precipitate, even though precipitation of the solute may not occur during the quench. Bryant (1966) has shown that the presence of small amounts of Cr and Mn in commercial Al-Zn-Mg alloys produce precipitates at elevated temperatures which act as nuclei for the formation of coarse $MgZn_2$-type precipitates at lower temperatures. Of course, the grain boundaries also act as preferential nucleation sites for coarse precipitates (Thomas and Nutting, 1953-54). Reduction of the quench sensitivity is an important area of current research in the aluminum industry and the avenues open for this involve the effect of alloy constitution and/or the replacement of elements such as Cr and Mn with alternative elements such as Zr.

2.2 Plastic Flow in Metallic Materials

The description of the mechanical deformation of a material may be divided into three regimes; the yield behaviour, the work hardening characteristics during plastic deformation, and the definition of the flow-limiting processes such as strain localisation and fracture. The magnitude of the yield stress in very simple systems can be readily obtained from tension or compression tests and it can be predicted quite well (to within about 20%), assuming a random distribution of obstacles (Foreman and Makin, 1966). However, it is more difficult to predict the yield stress of materials containing more than one distribution of obstacles of different strengths, as in the case of hardening precipitates in a matrix containing elements in solid solution (Brown and Ham, 1971). Work hardening studies have been limited mainly to the immediate post-yield regime, i.e., small strain region, and only recently has the effect of large strain deformation on work hardening been investigated; consequently, this subject is not well understood. The role of fracture related events has received much attention in relation to fracture toughness and fatigue damage, but the quantitative understanding of these events on the ductility of sheet materials is less well established. This aspect will be reviewed in Section 2.4.

2.2.1 Yield Behaviour

Brown and Ham (1971) have reviewed the effects of dislocation-particle interactions on the flow stress of materials. The contribution of precipitate particles to the flow stress depends upon the nature of their interaction with glide dislocations. "Particle cutting" or "dislocation looping" processes can be distinguished depending on the nature and energy of the particle-matrix interface, the size of the particle and its ability to support a shear loop, and the lattice structure and degree of order of the particle. With respect to age-hardening alloys, the following description can be given to account for the variation in strength with ageing time and temperature.

Initially, the strength of the alloy is that of the supersaturated solid solution. The zones which are characteristic of the T4 temper are small (<100 Å) and coherent with the matrix, and hence, they are sheared by the matrix glide dislocations. The yield stress at this stage is governed by the stress necessary to force dislocations through the precipitates and the rate of work hardening is essentially that of the matrix. The work to force dislocations through these obstacles may depend on a number of factors, eg., coherency stresses, internal order of the precipitates, and interface effects. As the precipitate particles increase in size and the nature of their interface with the matrix changes, the work done in cutting each particle increases and the dislocations are eventually forced between the particles resulting in the formation of shear loops around the particles by the Orowan mechanism.

In the case where precipitates are sheared by the dislocations, the strengthening increment is a function of

$$(f \cdot \frac{r}{b}) \qquad \text{(Brown \& Ham, 1971)}$$

where f is the volume fraction of particles of radius r, and b is the burgers vector of the dislocations. As the size of the shearable precipitates increases, the flow stress will rise. For looping of the particles, the flow stress increment is a function of

$$(\frac{b}{\lambda}) \sim b \cdot \frac{f^{1/2}}{r} \;;\; f \sim \frac{r^2}{\lambda^2} \qquad (2\text{-}1)$$

where λ is the interparticle spacing, so that growth of the particles by coarsening results in a decrease in yield strength. This description can be seen schematically in Figure 2-2 for two different volume fractions of precipitate. (The approximate locations of the ageing conditions of alloy 2036 which will be used in the present study are indicated on the diagram; it is expected that some of the small dispersoid

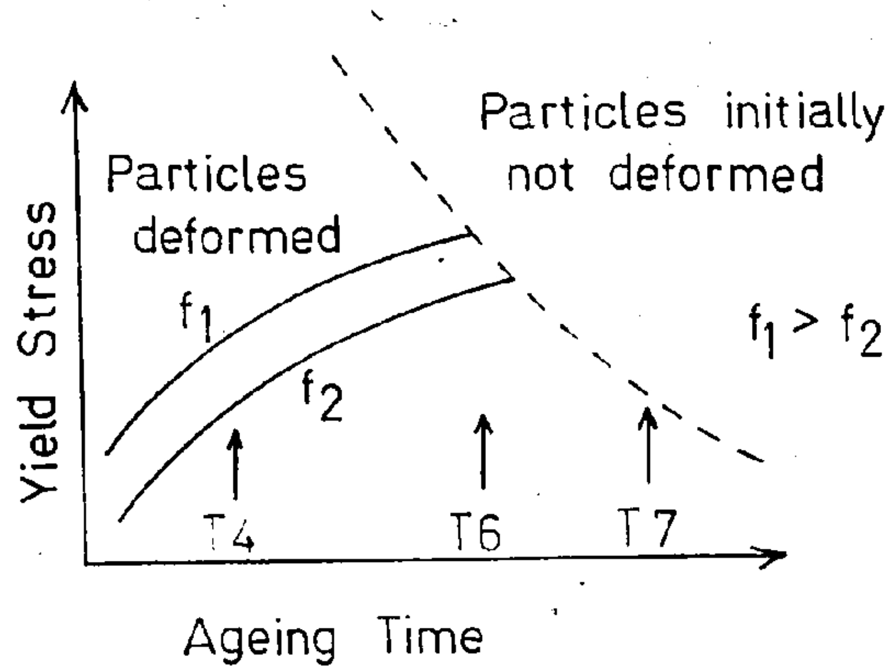

Figure 2-2 Schematic variation of yield stess with ageing time for typical age-hardening alloys with two different volume fractions of precipitate.

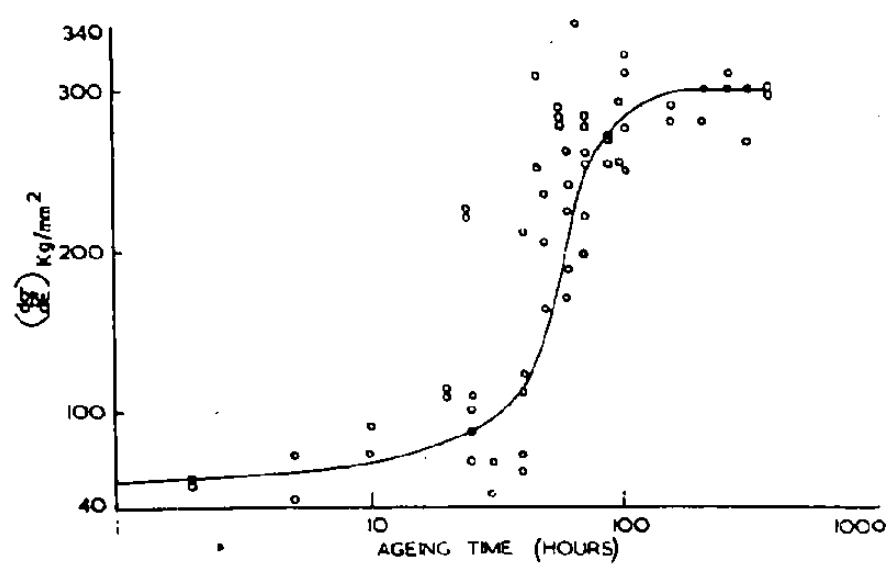

Figure 2-3 Plot of work hardening rate at 2% elongation of Al-1.6% Cu alloy as a function of ageing time at a temperature of 190°C (after Kelly & Nicholson, 1963).

particles will act as non-shearable particles at all ageing conditions). The initial work hardening rate as a function of ageing time at 190°C for an Al-1.6% Cu alloy is shown in Figure 2-3. It is generally accepted that the rapid increase in hardening rate arises when the material contains partially coherent and non-coherent particles which result in glide dislocations forming loops around the particles, effectively enlarging them, thus repelling subsequent glide dislocations (Fisher et al, 1953) and also in the secondary slip around the particles which generate further obstacles threading the slip planes (Ashby and Smith, 1960).

2.2.2 Work Hardening Behaviour

While the descriptions of the process of work hardening at modest plastic strains are capable of quantification in terms of the structural descriptions of dislocation accumulation and the rates and geometry of dislocation motion (Hirth and Weertman, 1968; Nabarro et al, 1964), the description of the plastic flow of both single crystals and polycrystals at large strains is much more empirical in form. Lücke and Mecking (1972) have pointed out the importance of dynamic recovery events which occur simultaneously with the hardening processes to gradually decrease the net work hardening rate at large strains.

Lloyd et al (1978) and leRoy (1978) have examined the progressive decrease of the work hardening rate at large plastic strains approaching fracture via the use of hydraulic bulge tests and tensile tests corrected to account for the necking process, and have presented their results in the form of the instantaneous work hardening rate, θ (=$d\bar{\sigma}/d\bar{\varepsilon}$) plotted as a function of either $\bar{\sigma}$ or $\bar{\varepsilon}$. This representation provides a better description of the work hardening characteristics than the more commonly used n-value derived from a constitutive equation of the form

$$\bar{\sigma} = K\bar{\varepsilon}^n \qquad (2\text{-}2)$$

where K and n are assumed constant over the strain range considered; and $\bar{\sigma}$ and $\bar{\varepsilon}$ are the effective stress and effective strain respectively. Values of n are derived from strains only up to the maximum load in a tensile test, and this portion of the strain history is not sufficient to describe the competition between continued plastic flow and flow localisation events determined by material instabilities (Embury, 1979a). The maximum load in the tensile test is given by the condition

$$\frac{1}{\sigma}\frac{d\sigma}{d\varepsilon} = 1 \qquad (2\text{-}3)$$

and the subsequent rate of development of a diffuse neck depends upon such factors as the strain rate sensitivity $(\frac{d\sigma}{d\dot{\varepsilon}})$ and the rate of change with strain of the work hardening rate in the neck $(\frac{\partial\theta}{\partial\varepsilon})$.

leRoy (1978) has discussed the relationship between work hardening rates observed at large plastic strains and such variables as the yield stress, structural parameters (solid solution, second phase particles), strain path, and strain rate sensitivity. The forms of the work hardening vs stress curves for a variety of aluminum alloys are shown in Figure 2-4. Here, it can be seen that for the precipitation hardened alloys which developed higher yield strengths, the rate of work hardening is not sustained but drops precipitously, leading to an increased tendency to the development of localised necking and rapid failure. For continued deformation to occur without localised necking,

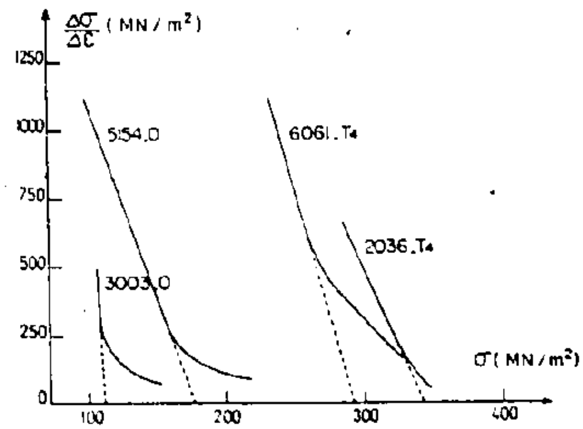

Figure 2-4 Variation of the work hardening rate vs. stress for four aluminum alloys with quite different strength levels (after Lloyd et al, 1978).

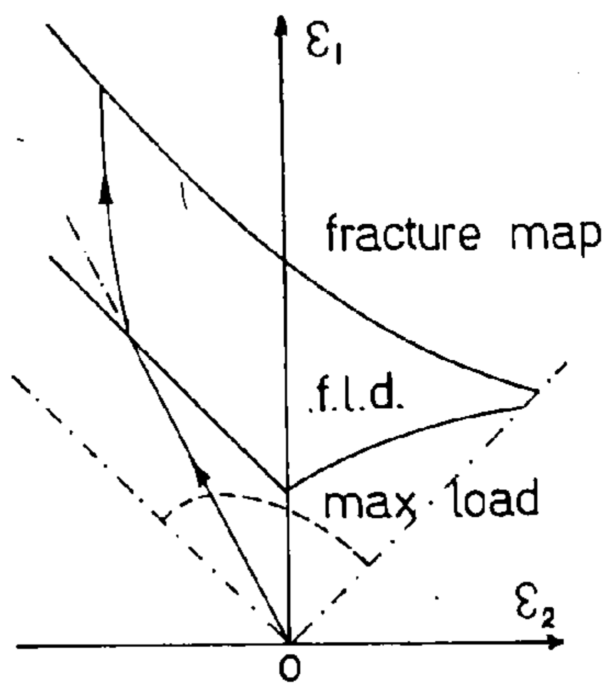

Figure 2-5 Schematic representation of the forming limit and fracture strains in strain space. After reaching the limit strain in proportional loading, the deformation tends towards plane strain up to the fracture strain.

it is vital to maintain the work hardening rate above a critical value since the condition for the stability of plastic flow is usually expressed in terms of the relative values of the flow stress and work hardening rate, i.e.,

$$\frac{1}{\sigma}\frac{d\sigma}{d\varepsilon} \geq \frac{1}{z} \qquad \text{(Generalised Considère condition)} \qquad (2\text{-}4)$$

In simple tension, localised necking is represented by $z = 2$.

The decreased work hardening rate at large plastic strains may result from the accumulation of damage within the material and/or the occurrence of dynamic softening events. leRoy (1978) suggests that this can be explained in terms of the influence of structural variables on the rate of dynamic recovery, eg., the decrease in distance over which the recovery events operate (as the substructure scale decreases), or the possibility that the rate of decrease of work hardening is structure sensitive. It is clear, then, that the development of a structural description of the events accompanying the decrease in hardening rate would help elucidate the critical events occurring in large strain deformation and their influence on forming processes.

2.3 Formability Concepts

The concept of the Forming Limit Diagram (F.L.D.) has provided an important tool for the assessment of sheet metal formability (Keeler, 1965; Goodwin, 1968). These diagrams indicate the manner in which the limiting value of the imposed surface strains vary with the ratio of the major to minor strains, $\varepsilon_1/\varepsilon_2$. leRoy (1978) has reviewed the important aspects in the experimental determination, theoretical prediction, and effect of inhomogeneities on the general F.L.D., while Embury (1979a) has summarised the interpretation of the F.L.D. in regard to the formability of aluminum alloys.

The schematic F.L.D. depicted in Figure 2-5 shows that the range of strains of importance is greater than that recorded up to the maximum load in the tensile test. Theoretical interpretations of the F.L.D. have been attempted by a variety of authors wherein the prediction of the curve is premised by the assumption of proportional straining and the representation of material plasticity by parameters such as n, the strain hardening coefficient, and r, the plastic anisotropy ratio, which are assumed to be invariant with strain history. A comparison between the theoretical and observed F.L.D. for the region where $\varepsilon_2 < 0$ has been produced by Painter and Pearce (1972) who find the form of the diagram is in accord with the criterion of Hill (1952) for the development of a localised neck. In the region of the diagram $\varepsilon_2 > 0$, theoretical interpretation is much more complicated since strain localisation should not develop in a homogeneous material. However, the concept of geometric and material inhomogeneities postulated by Marciniak and Kuczynski (1967) provides a method of assessing the right-hand side of the diagram.

It is important to distinguish between geometric defects in which local cross-sectional differences exist, and material defects in which local flow stress or hardening rate changes occur. The relationship of material and geometric defects has been attempted with respect to the local inclusion content of a material (Haberfield and Boyles, 1975) but it was found that the magnitude of the geometric defect needed to make the Marciniak and Kuczynski theory coincident with experiment was one-third of that provided by assuming that groups of coarse inclusions are equivalent to the geometric defect. In general, the effect on the F.L.D. of defects and heterogeneities initially present in the material (or which develop during deformation) is not yet clear, but Minh, Sowerby and Duncan (1975) have considered a statistical approach to the variation of the F.L.D. which may provide a basis for more detailed microstructural studies which relate to the development of inhomogeneities as a function of strain history.

2.3.1 Microstructural Features

Microstructural inhomogeneities in sheet material can be introduced at various stages of thermal/mechanical processing and correspond to different scales on the microscopic level. Examples of these are elongated colonies of grains of different size or orientation, strings of inclusions resulting from interdendritic segregation, regions of differing concentrations of second phase particles precipitated during homogenisation, and local variations in the distribution of fine scale hardening precipitates (especially near grain boundaries). For in-plane forming operations with $\varepsilon_2 < 0$, the effects of such inhomogeneities are adequately accounted for by a change in the (continuum) mechanical properties of the sheet, provided the distribution of heterogeneities is reasonably uniform, but in the case of biaxial stretching ($\varepsilon_2 > 0$), quite the opposite is true. The problem becomes one of understanding how particular microstructural defects can trigger the macroscopic localisation of strain, and the complexities of this problem have been pointed out by Wilson and Acselrad (1978) who note that there are many more internal (microscopic) than external (macroscopic) constraints, although in some instances (eg., thin sheet), these may be related (Tadros and Mellor, 1978).

Some of the defects which can be produced during forming operations as a result of microstructural inhomogeneities include the "orange peel" effect; roping lines (Wycliffe, 1977); various surface roughening effects resulting from production (Tadros and Mellor, 1978); voiding and microcracks nucleated at second phase particles; and grain boundary cracks due to either the presence of grain boundary precipitates or of a precipitate-free zone adjacent to the boundary. Wilson and Acselrad (1978) suggest that second phase particles are the principal sources of plastic inhomogeneity in commercial materials with grain sizes in the range 20 - 45 mm, while in larger grained materials, the grain size itself appears to exert the dominating influence, as shown in Figure 2-6. These authors investigated the effect of some types of inhomogeneities on the onset of strain localisation in biaxial stretching by introducing artificial defects (indentations) in the sheet prior to stretching. They found significant influences on strain localisation only when the defects could interact to form some sort of Marciniak "trough", as evidenced in Figure 2-7. This series of experiments emphasised the deleterious effect of microstructural inhomogeneities resulting from the rolling process, eg., strings of inclusions or elongated grains.

2.3.2 Fracture Maps

In addition to the forming limit curve, there is also a second envelope which can be drawn in principle strain space, and this is shown schematically by the upper curve in Figure 2-5. This indicates

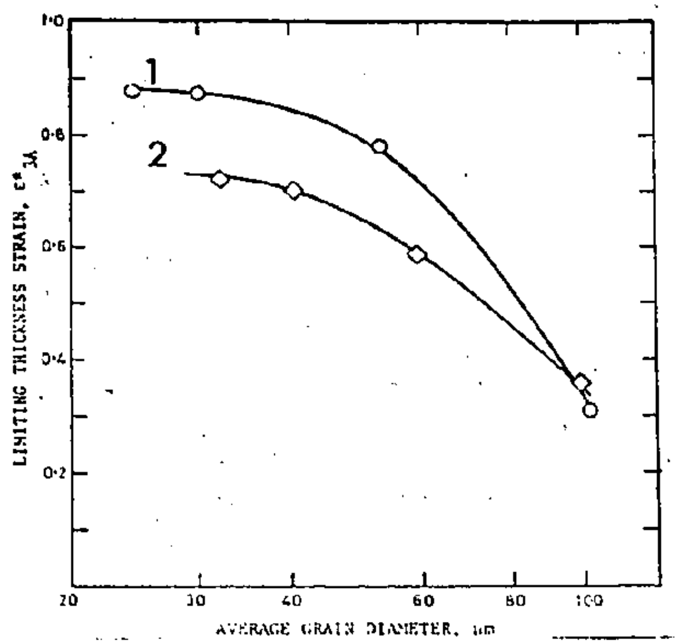

Figure 2-6 Effect of grain size on limiting thickness strains in equi-biaxial stretching for 1, EDD quality low-C steel; and 2, an experimental steel containing large inclusion particles (after Wilson and Acselrad, 1978).

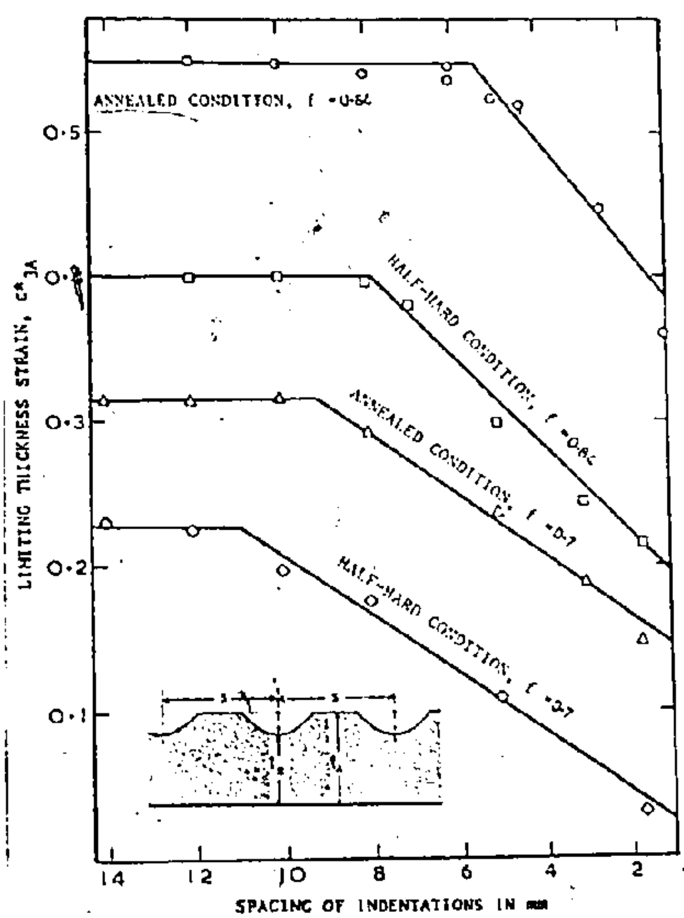

Figure 2-7 The effect of defect spacing on limiting thickness strains in equi-biaxial stretching, for aluminum with rows of equally spaced axisymmetric indentations. Tests made with two depths of indentation and in two material conditions (after Wilson and Acselrad, 1978).

the strain in the material at fracture, and lies at major strains greater than the F.L.D. due to the additional non-uniform plastic strain associated with the localised necking process. The straining process after the limit tends towards plane strain (Azrin and Backhofen, 1970) so that the strain path is curved as shown. If a simple loading trajectory is assumed, it is possible to construct the instability and fracture criteria in stress as well as strain space (Glover et al, 1977; leRoy and Embury, 1977a) and the relative shapes and positions of the F.L.D. and fracture map can be used to better interpret sheet metal formability.

leRoy and Embury (1977b) have considered the application of the fracture maps to a variety of aluminum alloys. As an example, curves in stress and strain space for alloy 5154-0 are shown in Figure 2-8. This alloy fails by a void nucleation and growth process where the extent of necking systematically decreases as the loading path approaches balanced biaxial stretching (Figure 2-8(a)). In stress space, the relative separation of the yield locus and limit map reflects the work hardening capacity of the material at modest strains, while the separation of the limit and fracture maps reflects the ability to sustain work hardening at large strains and also the influence of the strain rate sensitivity on the hardening rate. The operative failure criterion is consistent with one of constant thickness strain. On the other hand, alloy 2036-T4 appears to exhibit failure which is consistent with a maximum shear stress criterion (Figure 2-9). This process can severely limit the utilisation of material deformed by in-plane shear and is thus an important example of materials where the work hardening exponent may be sufficient but formability is terminated by the onset of failure at

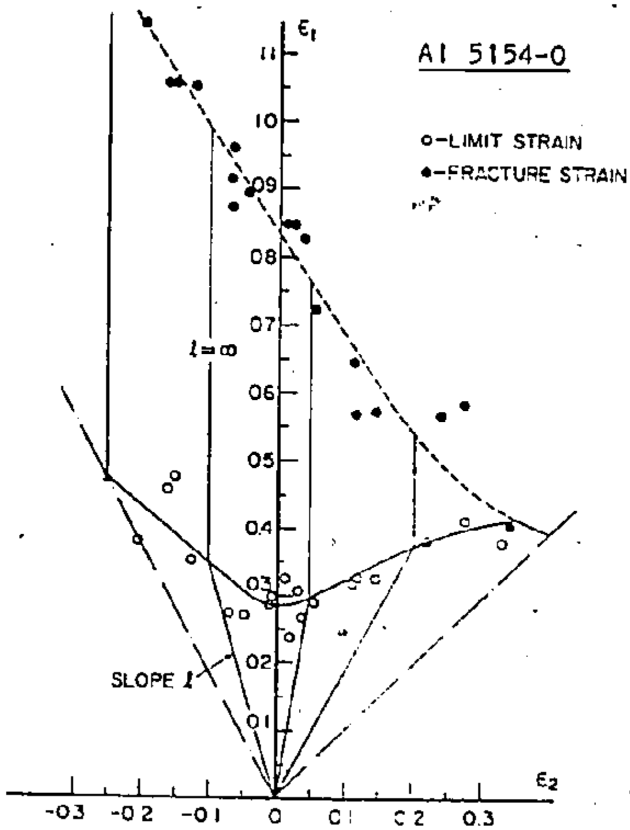

Figure 2-8(a) F.L.D. and fracture map determined for commercial Al-Mg alloy 5154-0. Straight lines (slope ℓ) illustrate the choice of strain paths.

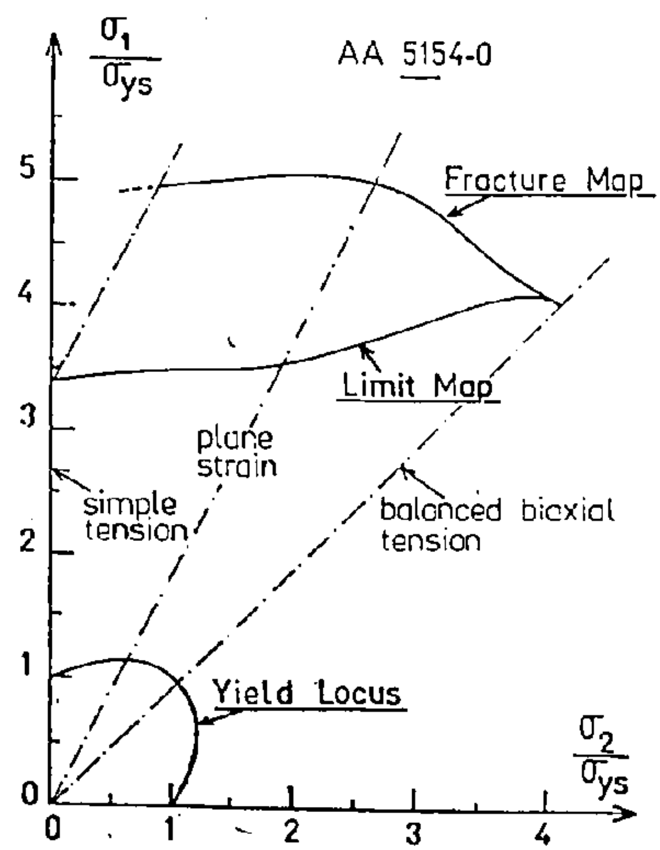

Figure 2-8(b) F.L.D. and fracture map in stress space with axes normalised by the magnitude of the yield stress. Dashed lines illustrate the loading paths.

(after leRoy & Embury, 1977b)

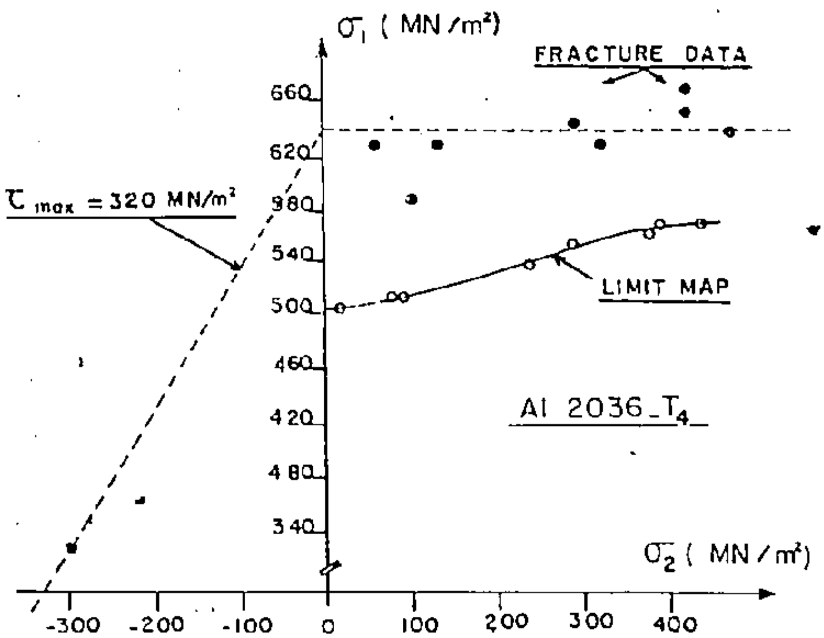

Figure 2-9 F.L.D. and fracture map in stress space for Al-alloy 2036-T4. (after leRoy and Embury, 1977b)

a critical stress level. These examples indicate the consideration which must be given to both the F.L.D. and fracture map of sheet materials.

2.3.3 Bending Deformation

The high proportion of sheet metal failures which occur in a plane strain mode of deformation (bending and flanging) suggests the importance of being able to characterise the response of materials to this type of loading. It has been recognised (Wang and Wenner, 1974) that minimum bend radii for plane strain bending provide useful data for the comparison of alloys, and are also of great assistance in the design of tooling. The mechanics of bending have been described by Hoffman and Sachs (1953) and other authors (Datsko and Yang, 1960; Rolf and Patrick, 1977) have attempted to correlate the bendability of materials with their tensile properties.

From consideration of the definition of the true strain at fracture (ε_f) in terms of the percent reduction in area (Ar), i.e.,

$$\varepsilon_f = \ln \left(\frac{100}{100-Ar}\right). \tag{2-5}$$

Datsko and Yang (1960) obtained formulae for the minimum bend radius to thickness ratio (R/t) based on the premise that failure in bending occurs when the outermost fibre of material reaches its fracture strain determined from a uniaxial tension test.

For the case where the neutral axis of the bend does not remain in the mid layer of the material, it was determined that

$$\frac{R}{t} = \frac{(100 - Ar)^2}{200Ar - Ar^2} \tag{2-6}$$

i.e., plots of R/t versus Ar are hyperbolic and asymptotic to the R/t axis. A variety of sheet and plate materials (Al-alloys, Mg-alloys, Cu-alloys, steel) were tested and found to conform quite well to this relationship. Thus, it was concluded that comparisons between the tensile reductions in area of different materials could be used as a measure of the bendability.

The critical nature of deformation close to plane strain has led to the development of the Limiting Dome Height (L.D.H.) test (Ghosh, 1975) to elucidate formability in this regime. The critical parameter measured is the displacement of the punch at maximum load, and since the load continues to rise until fracture (Gricus and Drittler, 1977), this parameter is actually one of fracture. Examples of L.D.H. curves determined by Gricus and Drittler for four aluminum alloys are shown in Figure 2-10 together with the corresponding F.L.D.'s determined by grid strain measurements on the L.D.H. specimens. Clearly, the differences between these alloys are more easily resolved for the L.D.H. test. Note also for alloy 2036-T4 that the minimum in L.D.H. occurs slightly to the right of plane strain deformation; the reason for this is not known.

2.3.4 Heat-Treatable Aluminum Alloys

Bryant (1969) has reviewed the metallurgical factors affecting the properties of formed heat-treatable aluminum alloys under the principal headings of the condition of the materials before forming, their behaviour during forming, and the performance in service of the formed product. With respect to their initial condition, these alloys are not usually formed in the fully aged condition because of insufficient duc-

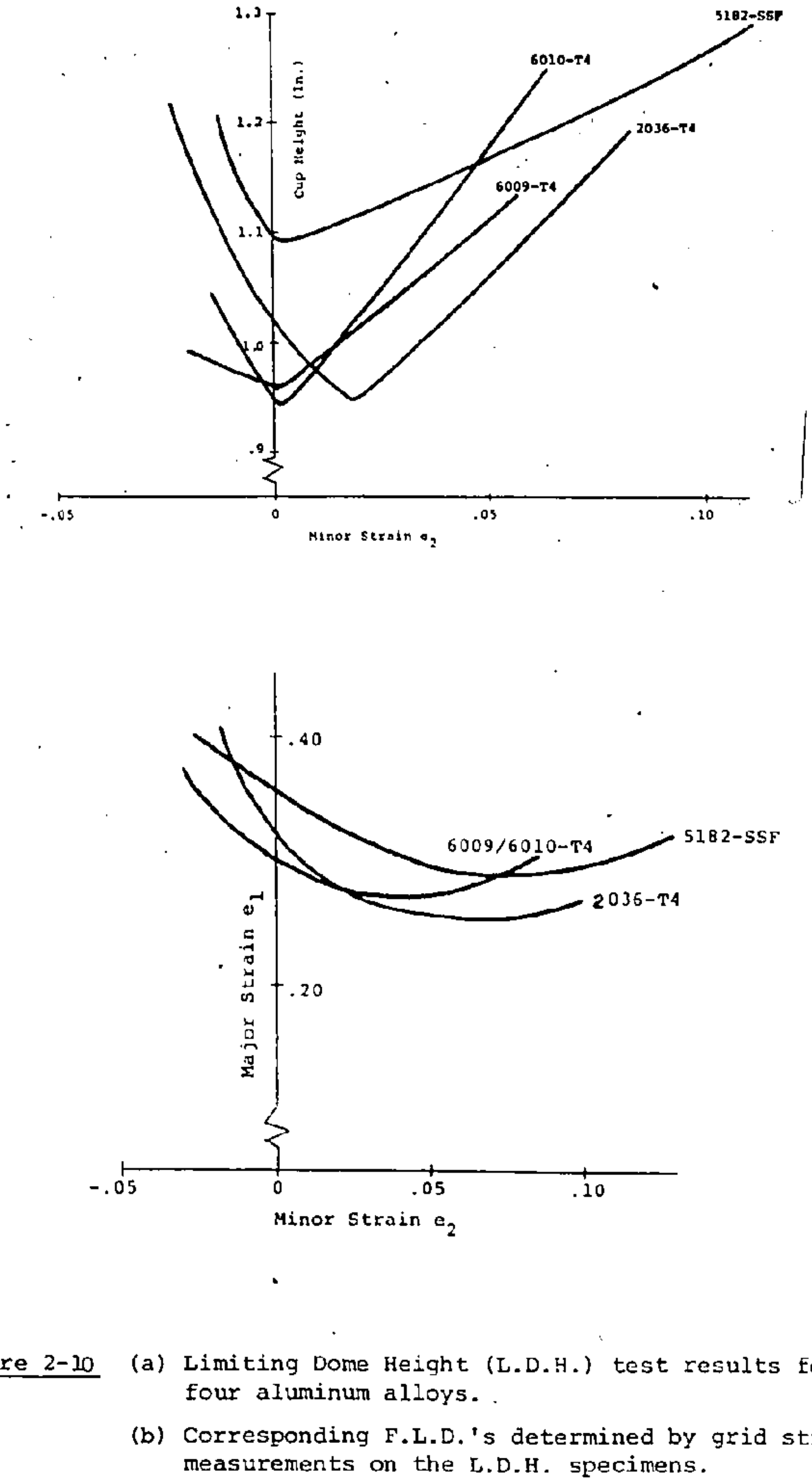

(a)

(b)

Figure 2-10 (a) Limiting Dome Height (L.D.H.) test results for four aluminum alloys.

(b) Corresponding F.L.D.'s determined by grid strain measurements on the L.D.H. specimens.

(after Gricus and Drittler, 1977)

tility, but the final properties expected of the formed component determine the initial condition of the material. Possible initial conditions are:

a) fully annealed,

b) solution-treated and naturally aged,

c) freshly quenched after solution treatment,

d) reverted after natural ageing,

e) refrigerated immediately after solution treatment,

f) heated above room temperature.

2.4 Ductile Fracture

Ductile fracture in commercial materials involves either or both of a fibrous mode and a shear mode, as present in the well-known "cup and cone" fracture. The fibrous mode results from the transverse linking of internal cavities while the shear mode results from some shearing instability which is generally superimposed upon the formation of internal cavities. Although the fundamental understanding of the relationship of microstructure to fracture is not nearly so complete as for the microstructure/strength relationship, much has been learned in the past decade and a number of articles (Rosenfield, 1968; leRoy, 1978; Goods and Brown, 1979) exist which provide excellent reviews of this recent work. Thus, the present review is limited to sketching the occurrence of various fracture modes in relation to the behaviour of commercial aluminum alloys.

2.4.1. The Fibrous Mode

The fracture strain (ε_f) of a material can be expressed in an approximate manner as the sum of the macroscopic strains associated with each of the void nucleation (ε_N), void growth (ε_g) and void linking (ε_ℓ) stages of fibrous fracture, i.e.,

$$\varepsilon_f = \varepsilon_N + \varepsilon_g + \varepsilon_\ell . \qquad (2\text{-}7)$$

Most models of fibrous fracture make use of this equation, although it often appears necessary to allow for continuous nucleation, i.e., the nucleation of some voids during the growth stage of others. Furthermore, the linking strain (ε_ℓ) is usually set equal to zero because of the extreme localisation of this process once void linkage begins. Homogeneous nucleation of voids is not applicable to complex commercial alloys and will not be considered in this survey. Goods and Brown cover this aspect in their review.

Experimental determination of the heterogeneous void-nucleation strain reflects both the characteristics of the material system and the sensitivity of the technique used. The previous experimental evidence indicates that this nucleation strain is affected by a number of parameters including particle shape and distribution, interfacial strength, and hydrostatic pressure. The conditions which aid void formation are:

a) high strain levels or local stress concentrations to provide the necessary interfacial decohesive stresses,

b) a lack of operative relaxation mechanisms (elongated particles, low temperature, coarse slip in the matrix), and

c) a low interfacial energy (poorly bonded or brittle inclusions).

Once internal cavities are nucleated, they can expand during continued plastic deformation of the matrix. Many authors (Ashby, 1966; McClintoch, 1968; Rice and Tracey, 1969; Brown and Embury, 1973) have treated the problem of void growth and there is reasonably good agreement with the experimental evidence. For the case of uniform tensile deformation, the models of Ashby, and Brown and Embury, who assume that the cavity size increases in proportion to the macroscopic strain of the specimen, provide a sufficiently accurate description of the void growth strain.

Perhaps the least documented aspect of ductile failure is the final void linking process. The normal contact of growing cavities, shown in Figure 2-11(a), has been observed (Rogers, 1960), but so too has the concentration of shear strain into sharply defined bands (Figure 2-11(b)) within which voids can link (Chin et al, 1964). Brown and Embury (1973) have proposed a quite successful criterion for void linking; they suggest, as shown in Figure 2-11(c), that the plastic constraint of the matrix between voids can be removed by extremely localised shear events if the void length equals the void spacing. Once the slip line field can be drawn between the voids, fracture ensues immediately by local multiple internal necking.

2.4.2 The Shear Mode

Localised shear failure has been observed in single crystals at low temperature (Chin et al, 1964), high strength aluminum alloys (Herø, 1978) and high strength steels (Chakrabarti and Spretnak, 1975) at ambient temperatures. It is generally observed after extensive plastic

(a)

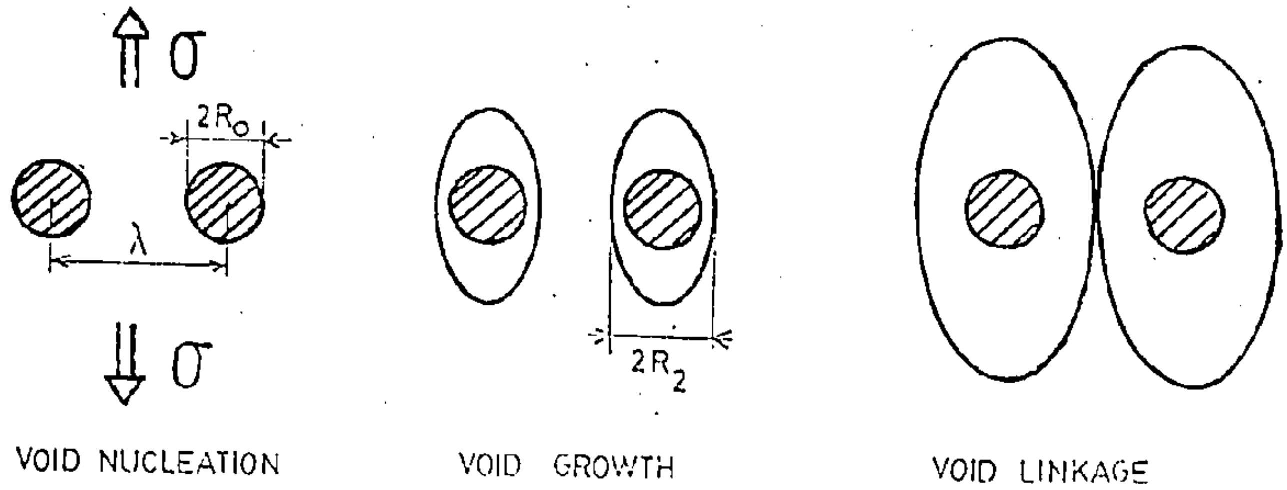

(b)

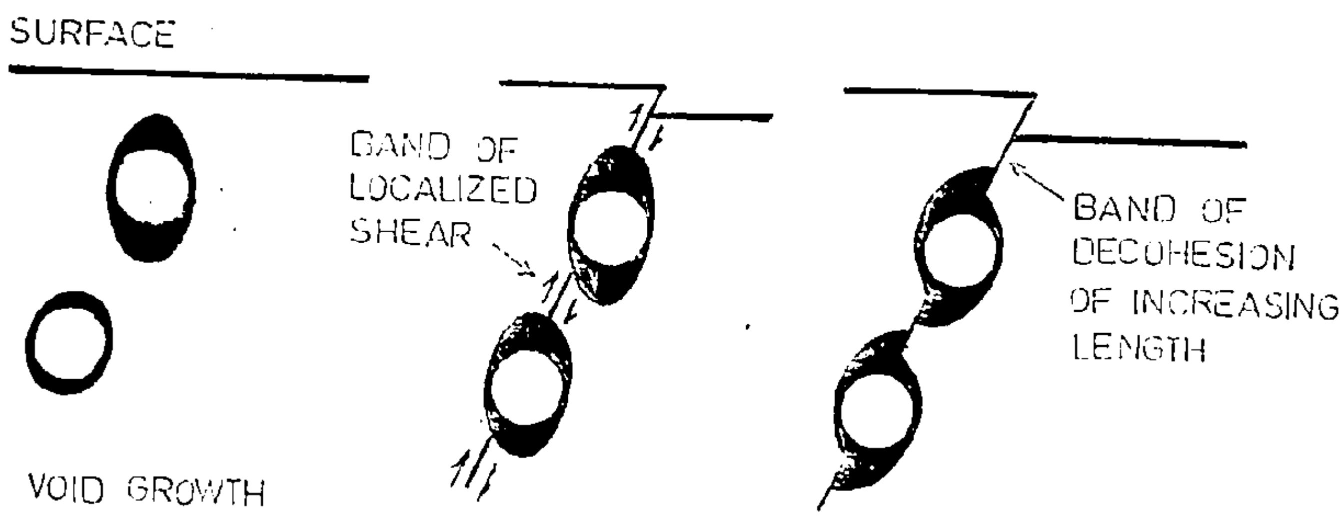

(c)

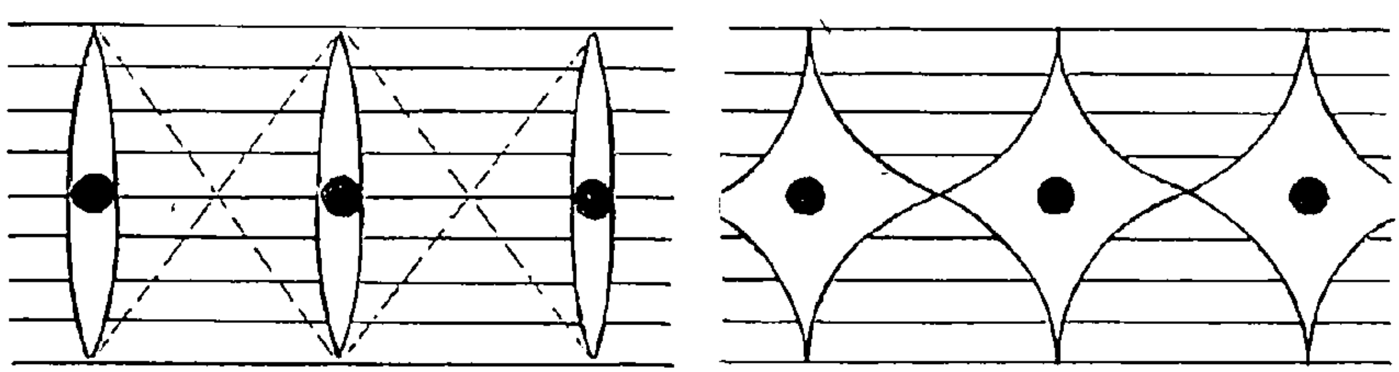

Figure 2-11 Schematic diagrams showing different void linking conditions:
(a) transverse linking (McClintoch, 1968),
(b) linking within narrow band of shear,
(c) local multiple necking (Brown and Embury, 1973).

deformation and initiates in the form of narrow shear bands within which further deformation tends to be localised. There appears to be no unique origin of macroscopic shear failure, but it can generally be regarded as a result of the extreme localisation of plasticity which occurs when the work hardening rate approaches zero and the material assumes ideally plastic behaviour. Beevers and Honeycombe (1962) have described shear failure in terms of a critical stress condition, however, the extensive plastic flow prior to failure together with the nature of the fracture surfaces suggest that consideration of this failure as a macroscopic strain localisation event initiated by the decreased work hardening rate may be more appropriate.

To achieve this type of unstable behaviour, there must exist conditions for both the nucleation of localised deformation and the growth of the instability (Embury and Nes, 1974). The nucleation event must develop due to some strain softening event, such as the shearing of coherent precipitates, the nucleation and growth of voids, or the development of surface irregularities, since there is no ascribable first order change in stress due to area reduction. The growth condition is generally expressed as a transition from the work hardening state to the ideal plastic state (Chakrabarti and Spretnak, 1975; Chung et al, 1977):

$$d\sigma \leq 0 \tag{2-8}$$

where σ is the flow stress in the material. If

$$\sigma = \sigma(\varepsilon, \dot{\varepsilon}, T) \tag{2-9}$$

then, the above condition becomes:

$$d\sigma = \left(\frac{\partial\sigma}{\partial\varepsilon}\right)d\varepsilon + \left(\frac{\partial\sigma}{\partial\dot{\varepsilon}}\right)d\dot{\varepsilon} + \left(\frac{\partial\sigma}{\partial T}\right)dT \leq 0 \qquad (2\text{-}10)$$

where the final two terms are potentially negative. Evidence supporting the validity of this condition has been discussed by leRoy (1978).

French and Weinrich (1979) have recently described the sequence of events associated with the shear failure of a spheroidised steel. A diagonal crack first forms near the centre of the specimen thickness as a result of the combined shear and tensile deformation. This is depicted in Figure 2-12, where voids develop by separation of the carbide-matrix interface within a colony of closely spaced carbides (b). These voids grow by shear in the manner of (c) until final coalescence occurs (d) to form a crack roughly parallel to the shear zone. Several of these local cracks join to form the initial diagonal crack linking the large voids previously nucleated at non-metallic inclusions. Shear deformation then becomes concentrated towards the specimen surfaces and growth of the crack along the dominant zone occurs in a manner similar to that depicted in Figure 2-12.

2.4.3 Role of Microstructure in the Fracture of Aluminum Alloys

The fracture mode exhibited by commercial wrought aluminum alloys at ambient temperatures appears to be primarily related to the strength level of the alloy and secondarily related to whether the alloy system is heat-treatable or strain-hardenable. Low strength alloys, including the 1XXX-, 3XXX- and some 5XXX-series generally fail by the fibrous mode following the nucleation and growth of voids around the constituent particles. However, the heat-treatable 2XXX-, 6XXX-, and 7XXX-series

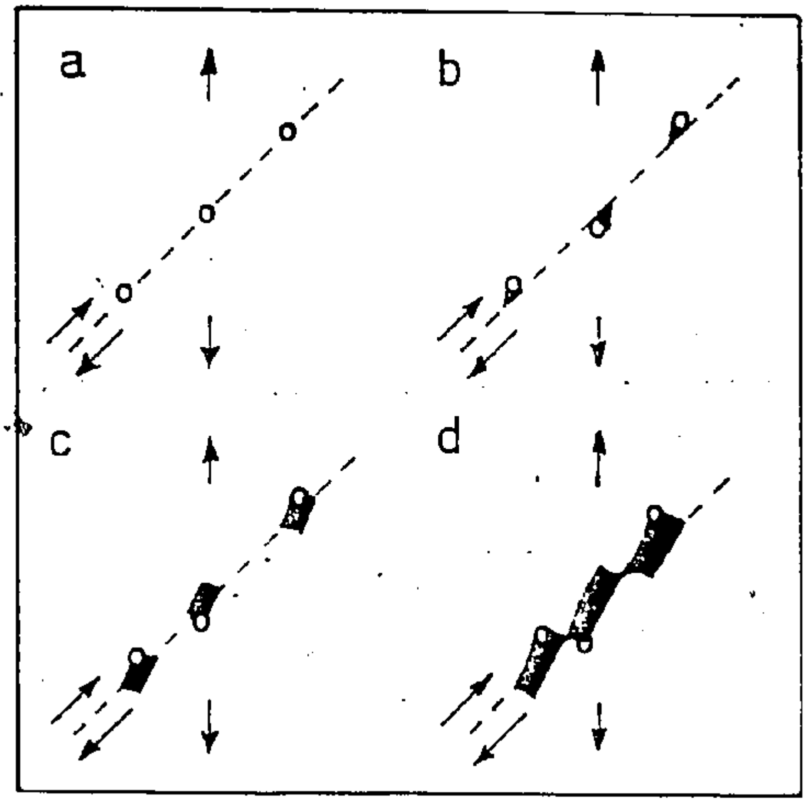

Figure 2-12 Schematic representation of the sequence of events associated with shear failure in a spheroidised steel (after French and Weinrich, 1979).

alloys (in the T4 and T6 conditions), together with the high-Mg 5XXX-series alloys exhibit differing proportions of fibrous and shear failure. Because the heat-treatable alloys are the subject of the present investigation, the following section will be concerned with the microstructural features of these alloys.

As described in Section 2.1, the heat treatable alloys contain particles of different scales, i.e., the constituents, the dispersoids, and the fine-scale hardening precipitates, and these have separate roles in the deformation and fracture behaviour of these alloys. Hahn and Rosenfield (1975) and Staley (1975) have provided excellent reviews on this subject, especially with regard to fracture toughness considerations. Broek (1971) and Low et al (1972) established that voids are initiated primarily by the cleavage fracture of constituent particles at low strains (<7% in uniaxial tension) which can then nucleate voids that grow with the imposed plastic strain to become the large dimples evident on the fracture surfaces. Broek further suggests that the cracking of the small, dispersoid particles is the critical event determining fracture. In contrast, however, Hahn and Rosenfield (1975) contend that these particles are incidental to the critical fracture event as they fail subsequent to the localisation of deformation. Van Stone and Psioda (1975) suggest that the final fracture event involves the coalescence of voids (initiated at large constituents) by the formation of voidsheets initiated by interface decohesion at the dispersoids. The hypothesis of Hahn and Rosenfield is generally supported by Garrett and Knott (1978) who consider the role of the dispersoids as primarily influencing the nature and distribution of the slip process within the matrix.

The most influential factor governing the nature of slip in the matrix of age-hardening alloys is the presence of the fine-scale coherent precipitates. It is well known (Boyd et al, 1972; Hahn and Rosenfield, 1975; Garrett and Knott, 1978) that the presence of these precipitates promotes planar slip as the dislocations find increased difficulty for cross-slip. Such planar slip can result in the formation of superbands of deformation (Hahn and Rosenfield, 1975) especially in plane strain bending, which promote microcracking within the bands, and decohesion of grain boundaries and particles upon which the bands impinge. In these cases, failure is characterised by extensive shear throughout the grains reflecting the loss of local work hardening rate associated with the planar slip (Griffis and Spretnak, 1969). There still remains the important problem of how these local events condense into the final fracture event and evidence will be given later in this thesis which suggests that particular microstructural features may influence this process.

The effect of ageing condition on fracture toughness is well known (Staley, 1975; Hahn and Rosenfield, 1975; Garrett and Knott, 1978) and it is pertinent to consider this in relation to the present situation of relatively low strain rate deformation. On going from the underaged through the peak-aged, and into the overaged condition, changes in toughness (Figure 2-13) accompany changes in the nature of the fracture surface. The underaged conditions exhibit extensive shear, while the overaged material shows a tendency (depending on the alloy, its purity, and grain size) towards intergranular failure. Attempts have been made to correlate the toughness parameter with the strain hardening exponent (n)

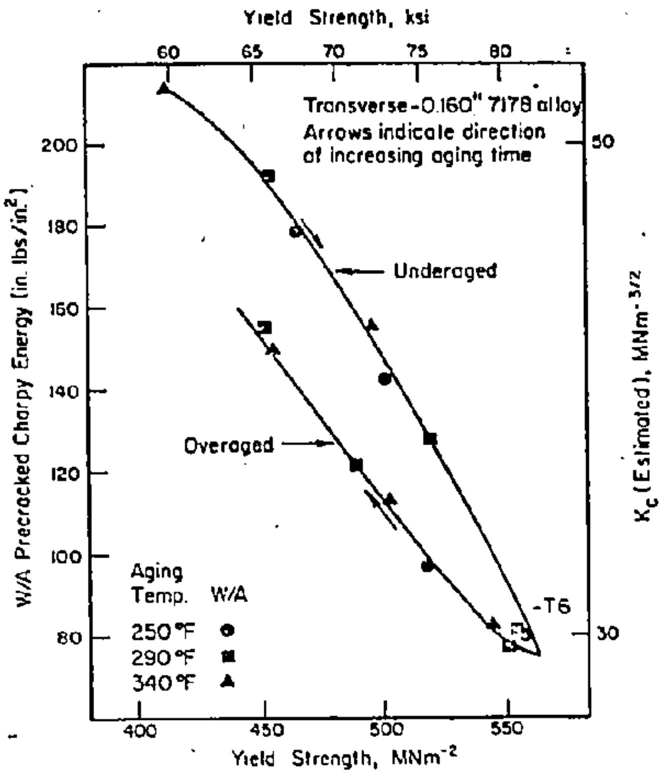

Figure 2-13 The effect of ageing on the fracture toughness of a 7XXX-series alloy (after Zinkham et al, 1968).

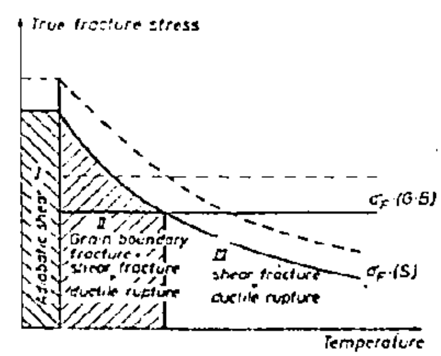

A schematic diagram showing the expected mode of failure as a function of temperature. The mode of failure in region II will depend on factors such as orientation, inclusion content, etc. The effects of metallurgical improvements are shown by the broken lines. The grain boundary fracture stress σ_F (G.B) can be increased by a) removal of impurities, b) reduction of the areal fraction of grain boundary precipitates, c) grain refinement, d) removal of the elongated fibrous grain structure. The stress for shear failure σ_F (S) can be raised by promoting an increase in strain hardening rate.

Figure 2-14 The effect of temperature on the fracture mode of a high strength Al alloy (after Embury and Nes, 1974).

of the aged materials. However, this is indeed speculative since many aluminum alloys exhibit a marked strain dependence of n. Possibly, a more influential factor is the degree of grain boundary precipitation. Although the distinction between the effects of the precipitate-free zone and the boundary precipitates themselves is difficult to resolve in many instances, the overall result of the presence of grain boundary precipitates is known (Embury and Nes, 1974). It was found that the critical fracture stress in tension increased with decreasing ageing temperature, suggesting that the critical condition for fracture depends on the amount of grain boundary precipitate.

2.4.4 Generalised Fracture Mechanisms

The various conditions which describe changes in the fracture mode of aluminum alloys can be represented by a schematic diagram such as Figure 2-14. In this diagram, the essential effect of metallurgical improvements are also indicated: the grain boundary fracture stress can be improved by the removal of impurities, the reduction of the areal fraction of grain boundary precipitates, grain refinement, and removal of an elongated grain structure. Similarly, the stress for shear failure can be increased by promoting increases in local work hardening rate, thus reducing the tendency to localised plastic flow.

In commercial aluminum alloys, as in many complex systems, it is necessary to consider if damage events such as void nucleation, cleavage of constituent particles, etc. occur, and if so, into what volume does the condensation of the damage events occur? This damage condensation process is offset by strain hardening of the matrix. Hence, the correlation of microstructural events and a description of the relevant volume of the material remains difficult to define because it is dependent on the details of the alloy system, the applied stress state, and temperature. However, the ability to define both fracture criteria and the microstructural events which promote fracture are very relevant aspects needed for the optimisation of formability in heat-treatable aluminum alloys.

CHAPTER 3

CHARACTERISATION OF MATERIALS

The different batches of alloy 2036-T4 were initially characterised with respect to their microstructural features and their basic uniaxial tensile properties. In addition, attempts were made to characterise the materials in relation to their strain rate sensitivity determined from changes in cross-head speed during uniaxial tensile testing and these data are also included in this chapter.

3.1 Microstructure

Microstructural characterisation of the three lots of 2036-T4 involved utilisation of the following optical and electron microscope techniques:

a) sectioning and polishing to reveal the extent and distribution of the large constituent particles,

b) appropriate etching to reveal the grain structure and the presence of any large grain boundary precipitates,

c) transmission electron microscopy to determine features of the dispersoid particle distributions and the distributions of metastable hardening precipitates, and

d) energy dispersive x-ray analysis carried out on a S.T.E.M. (scanning transmission electron microscope) of some of the particles observed in the microstructure to determine their composition.*

---

* Courtesy of Alcan Research Laboratories, Kingston, Ontario

The metallographic preparation technique which gave the best optical microscopy results involved grinding to 600 grit paper, followed by rough polishing with 5 μm alumina powder on billiard cloth, and finally a two-stage polish using MAGOMET magnesium oxide powder with distilled water on a synthetic cloth. Division of the final polishing stage was made to allow hand-polishing of the samples on a thick slurry of the MAGOMET/distilled water, as it was found that even the polishing cloth could scratch the surface under slight pressure. This technique differs slightly from that recommended in the A.S.M. Metals Handbook. The etchants used in this study were Keller's etch to reveal the grains, and a solution of 25% HNO_3 in water heated to 70°C to reveal the presence of grain boundary precipitates.

Figure 3-1 shows the as-polished (unetched) longitudinal sections of the different lots of 2036. The particles visible are the constituent particles which originate during solidification and are broken up and rearranged by the subsequent mechanical processing. It is obvious that the volume fraction of these constituents increases qualitatively in the order G-M-P, which is in accord with the chemistry of these materials, as tabulated in Table 1-1, especially regarding the total of the Cu, Fe, Si, and Mn additions. Close examination of the microstructures after etching with Keller's reagent indicated that material P had the highest concentration of particles of the soluble phase $CuAl_2$. These particles are not darkened by a light etch with this reagent. In all cases, the maximum size of the constituent particles is approximately 10 μm, and in this (longitudinal) section, there is very little evidence of strings of particles along the rolling direction.

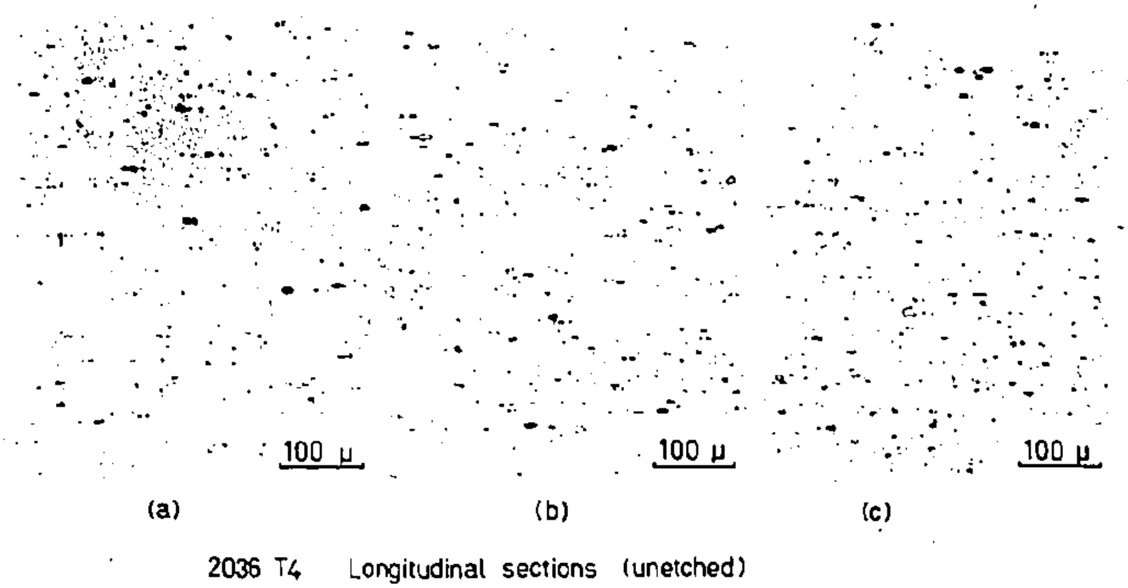

Figure 3-1 Longitudinal (unetched) sections of 2036-T4 materials (a) G, (b) M, and (c) P.

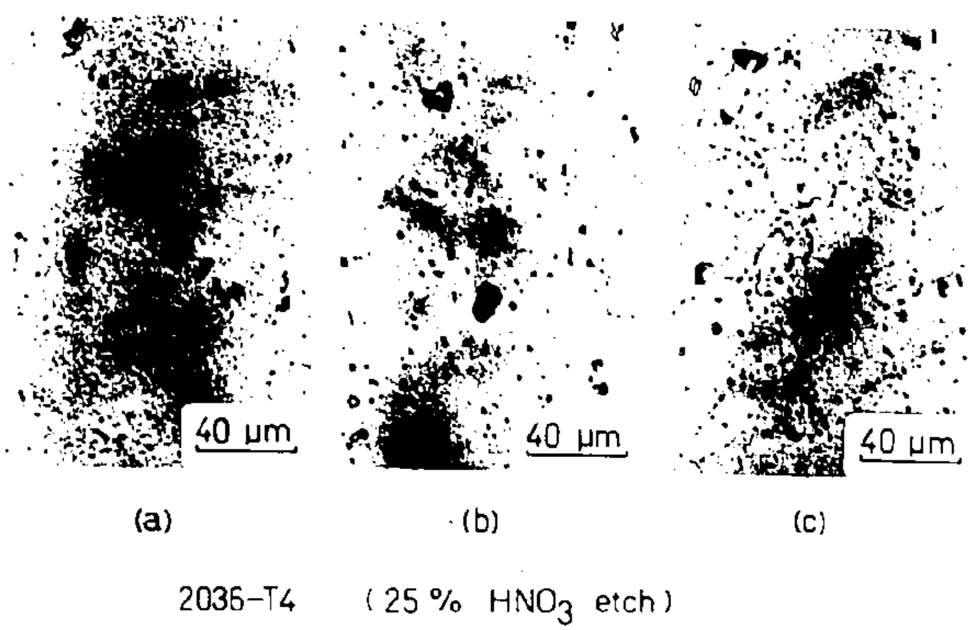

Figure 3-2 Microstructures in the plane of the sheet of (a) G, (b) M, and (c) P materials following an etch designed to reveal grain boundary precipitation.

The extent of discontinuous grain boundary precipitation is shown in Figure 3-2. These micrographs clearly indicate that material P has experienced a slack quench from the solution heat treatment temperature, allowing particles of the equilibrium phase to nucleate and grow on the grain boundaries. It is suggested that these particles are probably of the $CuAl_2$ phase, although no attempt was made to confirm this by analytical techniques.

A comparison of the through-thickness longitudinal grain structure is shown in Figure 3-3(a). Measurements of the grain size across the thickness show that G and M have grain sizes of $\sim$15 μm, while P has grains of $\sim$10 μm. The in-plane microstructures are shown in Figure 3-3 (b). Two aspects to note are the distribution of grain sizes and the tendency of the constituent particles to form strings along the rolling direction. Both G and M have a fairly uniform grain size of $\sim$45 μm, but P exhibits a marked variation in grain size which recurs periodically across the sheet width. Bands of small grains with diameters $\sim$20 μm lie between regions with grains of >30 μm diameter. The bands of small grains follow the strings of constituent particles which are separated by spacings typical of 200 μm. Strings of constituent particles were also noted in material M, however, there was no associated grain size variation. All the microstructures in Figure 3-3 result from the application of Keller's reagent for 15 seconds following a 3-minute etch in the 25% HNO_3 solution.

Transmission electron micrographs of the different batches of 2036-T4 as-received are shown in Figure 3-4. Foils were prepared in a TENUPOL machine using an electrolyte of 30/70 mixture of nitric acid

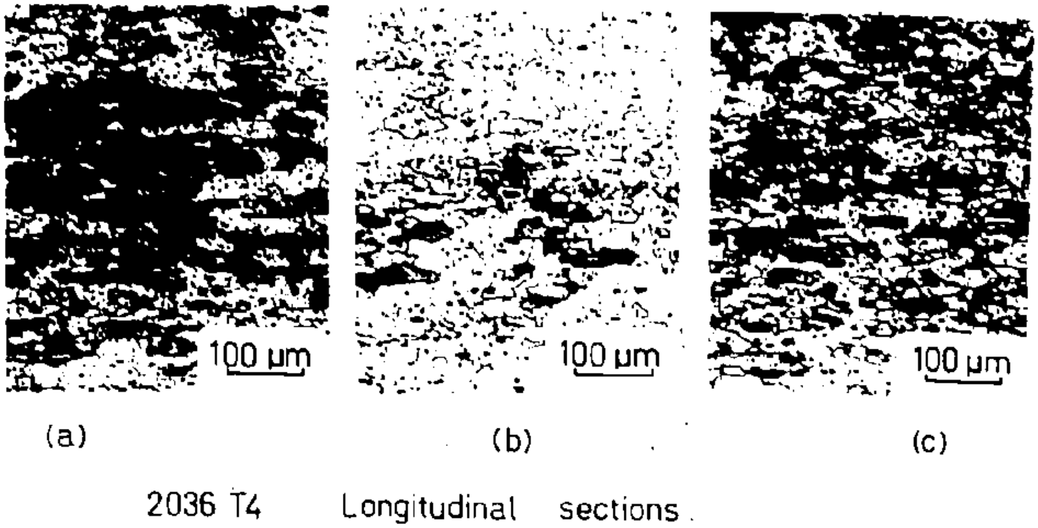

Figure 3-3(a) Through-thickness longitudinal grain structures of materials (a) G, (b) M, and (c) P. (Kellers etch)

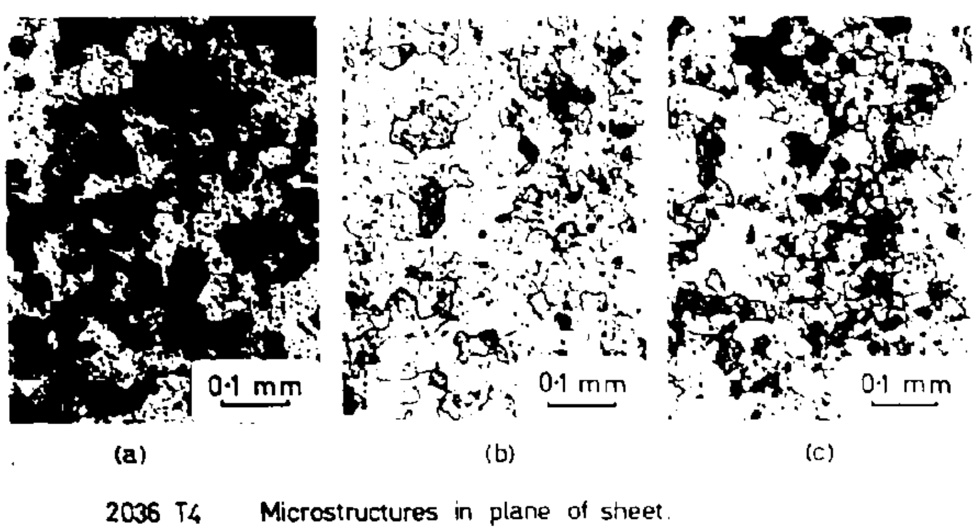

Figure 3-3(b) In-plane microstructures of materials described in Figure 3-3(a).

Figure 3-4(a) T.E.M. Material G

Figure 3-4(b) T.E.M. Material M

Figure 3-4(c) T.E.M. Material F

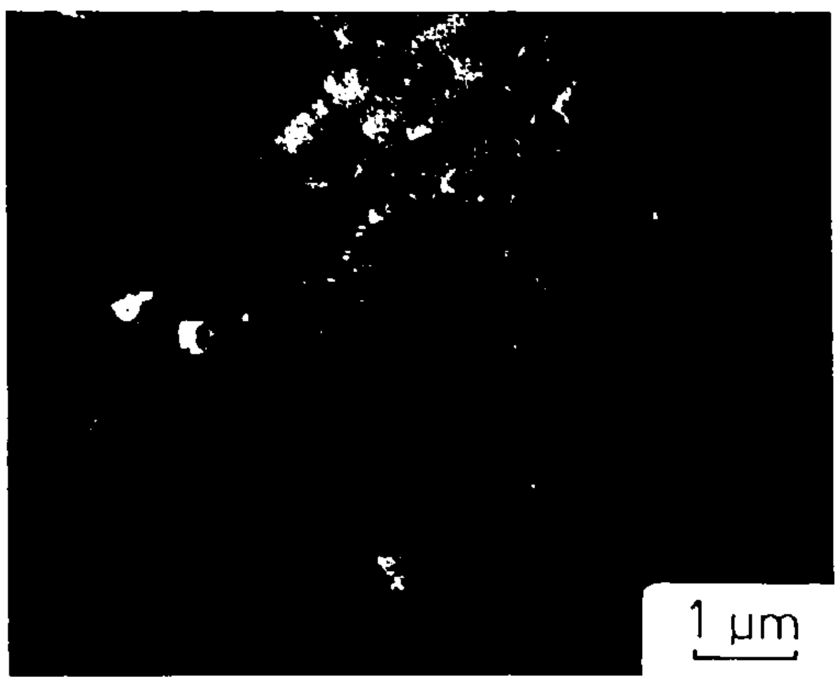

Figure 3-5 S.T.E.M. Material F
(Courtesy Alcan Research
Laboratories)

in methanol at a temperature of -30°C. The materials can be compared with respect to the extent of grain boundary particles. Materials G and M showed a few small particles (consistent with the dimensions of the dispersoids) in the boundaries while material P exhibited a relatively large number of particles in the grain boundaries. Many of these have dimensions and shapes unlike the dispersoids, and were thus assumed to be the precipitates of the $CuAl_2$ phase which nucleated during the slack quench. The presence of these precipitates confirms the effect noted previously in the optical metallography. No detailed electron diffraction analysis of these particles was performed.

Within the matrix of these materials, three different types of particles were observed whose extents and distributions varied from batch to batch. One group of particles exhibited dimensions typical of 0.1 μm with interparticle spacings of $\sim$1 μm. Many of these particles appeared to have hexagonal cross-sections and it is probable that these were the dispersoids, which is in accord with the observations of Chaturvedi et al (1979). Examination of these particles in the S.T.E.M. showed that they contained both Al and Mn, and hence, could possibly be the phase $Al_{20}Mn_3Cu_2$ (Staley, 1975). Figure 3-5 shows a number of these particles which were examined in one field of view. The large particle marked A was determined to be a Al-Mn-Fe phase formed on solidification.

Also appearing in the matrix were platelets of maximum dimension $\sim$0.5 μm which appeared to be associated with either some other particle or with the matrix dislocations. It was not possible to identify these particles or those associated with the platelets. However, since this type of particle was found almost exclusively in material P, it was concluded that it was the metastable form (θ') of the equilibrium precipitate $CuAl_2$, nucleated during the slow quench. Support for this is given by the fact that re-solution treatmeht and rapid quenching of the same material (see Chapter 4) removed these particles from the matrix.

Details of the dispersoid distribution in material P in the as-received condition were obscured by the presence of the platelets, so qualitative characterisation of the dispersoids was performed on the re-solution treated/rapidly quenched material. Materials G and M were studied in the as-received condition only. Although it is difficult to quantify with selected area microscopy, there appears to be fewer dispersoids in material G than in either M or P. It was not possible to distinguish between M and P on this basis.

Before discussing the fine scale precipitates associated with the hardening processes, it is pertinent to describe the dislocation structures present in the materials. The number of dislocations present is higher than expected from a simple quenching step because of the straightening operation which precedes the final coiling and natural ageing. This introduces additional dislocations which can form helices (Kelly and Nicholson, 1963) due to vacancy condensation following the quench and also assist the (heterogeneous) nucleation of the hardening precipitates during natural ageing (Hornbogen, 1969).

Natural ageing of heat treatable aluminum-copper alloys involves the homogeneous nucleation of coherent GP 1 zones (Kelly and Nicholson, 1963) and the heterogeneous nucleation of θ'' precipitates (Hornbogen, 1969). These can be resolved in transmission electron microscopy of thin foils by contrast effects due to elastic straining of the matrix surrounding a precipitate or to the difference in extinction distances between the precipitate and matrix (Hirsch et al, 1965). Difficulties in characterising these particles in the present materials were experienced due to surface effects resulting from thin foil preparation and also due to the effect of the Millband coating application, described in Chapter 1. Although the time for this processing step is short, the temperature is sufficient to cause some reversion of the GP I zone structure and nucleation of θ" (Byrne et al, 1961). Figure 3-6(a) shows the contrast effects associated with some form of zones in the matrix and the precipitate particles on the dislocations. Also noticeable are some needle-like structures which appear to be either platelets of θ' in cross-section, or s', and a region adjacent to the grain boundary in which the contrast effects are less distinct, signifying reduced precipitation. The complex arrangement of dislocations in the same material can be better seen in Figure 3-6(b), where the foil has been tilted to bring the dislocations into a strong diffracting condition.

In the present study, little attention was given to the detailed identification of precipitates in the T.E.M. Attempts to identify structural aspects of the T4 condition were not successful. However, in the T6 condition (see Chapter 6), diffraction evidence was obtained in the form of extra spots and streaks in the {100} spot patterns, eg., Figure 3-7. Chaturvedi et al (1979) report that the precipitates in 2036-T6 are of the θ' type, i.e., $(100)_{\theta'} \parallel (100)_{Al}$. It is also possible, however, that some form of S' can occur as laths which are parallel to <100>. Without extensive investigation of foil orientations other than (001), it is difficult to distinguish these possibilities and in this thesis, it has

Figure 3-6(a) T.E.M. - Material P showing contrast effects due to precipitates.

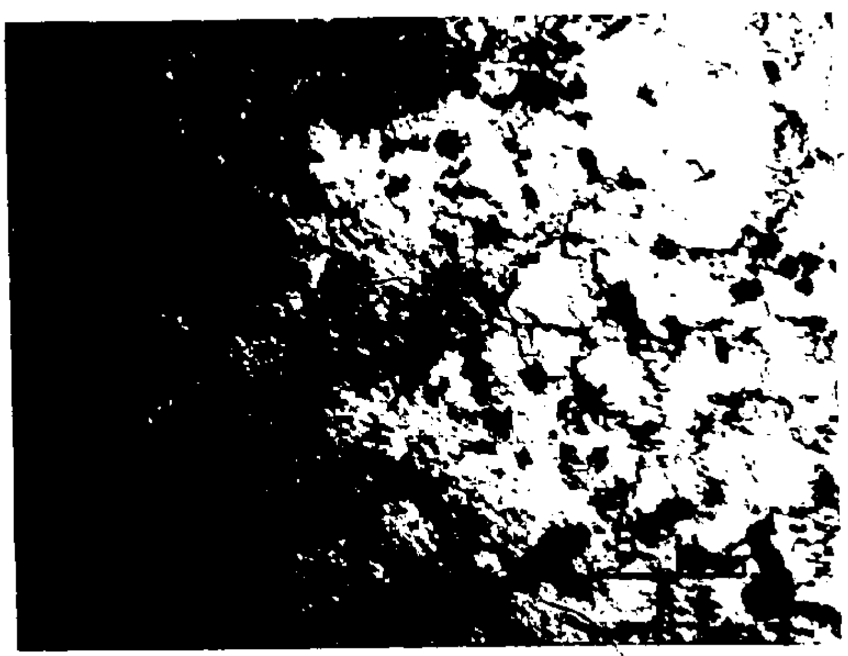

Figure 3-6(b) T.E.M. - Material P (tilted to bring the dislocations into a strong diffracting condition).

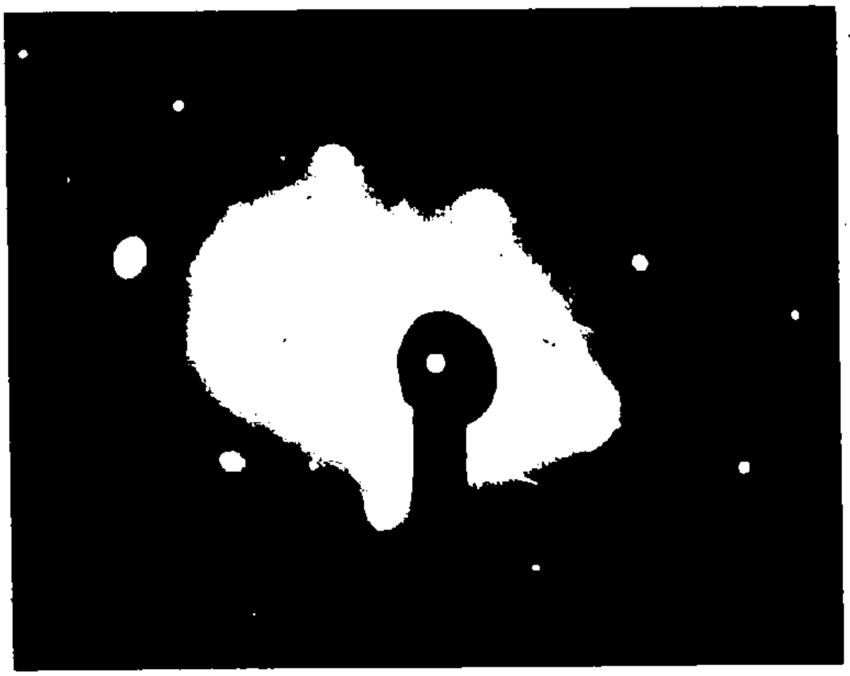

Figure 3-7 Diffraction pattern obtained from material G in the T6 condition. Pattern is $\{100\}$ type with streaks in $\langle 100 \rangle$ directions.

been assumed that the precipitate sequence is in accord with that proposed by Chatuvedi et al. However, additional work is needed to clearly identify the precipitation sequence and the relationship between the T4, T6 and T7 structures.

3.2 Mechanical Properties

Basic uniaxial tensile parameters for the three materials are given in Table 3-1. Included in this table are average values for the work hardening exponent derived from the Ludwik equation $\sigma = K\varepsilon^n$, as determined by members of the A.D.D.R.G. On a strength level basis, the materials rank in increasing order G ÷ P – M, while a comparison of uniform and total elongations (50 mm gauge length) indicates a ranking M – G – P in decreasing order. Clearly, the strength and ductility parameters are not simply inversely related. Comparison of the average n-values shows that both G and M are superior to P, but offers no explanation for the formability differences between G and M. In all cases, the tensile properties lie within the limits set by the Aluminum Association (1976).

3.2.1 Strain Rate Sensitivity

Instantaneous strain rate change tests were employed to determine the strain rate sensitivity of the three lots of 2036-T4. This type of test was chosen over the continuous test (at different strain rates) because it has been suggested (Kocks et al, 1975) that the latter does not provide a true indication of the effect of an imposed change in strain rate. Structural differences can arise due to the development of

Table 3-1

Uniaxial Tensile Parameters for 2036-T4

	MATERIAL		
	G	M	P
Longitudinal			
Yield Stress (MPa)	199	227	212
Ultimate Stress (MPa)	347	390	363
Total Elongation (%)†	22.6	24.2	21.2
Uniform Elongation (%)†	20.3	22.2	19.1
n-value*	.242	.240	.232
Transverse			
Yield Stress (MPa)	192	221	205
Ultimate Stress (MPa)	344	383	357
Total Elongation (%)†	25.6	25.9	23.2
Uniform Elongation (%)†	22.3	22.7	19.8
n-value*	.241	.243	.234

† 50 mm gauge length used

* A.D.D.R.G. Aluminum Cooperative Group average

substructure at different strain rates, whereas, for the present situation, the effect of the change at constant structure is important. Of course, the structure developed at the testing strain rate may differ from that developed at the (higher) production rate, but it is assumed that the sign of the flow stress change is independent of the reference strain rate. However, to provide a more comprehensive view, it would be preferable to use a variety of strain rates and temperatures.

Strain rate change tests on 2036-T4 were found to produce some ambiguities because of this alloy's tendency to unstable flow following any increase in strain rate. The occurrence of this type of flow depends upon the strain (and stress level) at which the change is made. Hence, rate sensitivity data was collected for "down-changes" only, and then with only one change per test, since reverting to the original strain rate constituted an "up-change" resulting in unstable flow. Results of the tests are shown in Figure 3-8, as a plot of $(\Delta \ln\sigma/\Delta \ln\dot{\varepsilon})$ vs ε. The rate sensitivities of the three materials appear to diverge slightly with increasing strain, and near the U.T.S. of the materials, G has the least negative value and P the most negative. Unfortunately, the rate sensitivity of the yield stress could not be determined because the zero suppression adjustment on the Instron did not allow the yield point to be clearly obtained.

3.3 Discussion of Materials Characterisation

The difficulties in correlating the scale of microstructural features with uniaxial tensile properties in complex materials are apparent in the present study. Although many obvious differences in

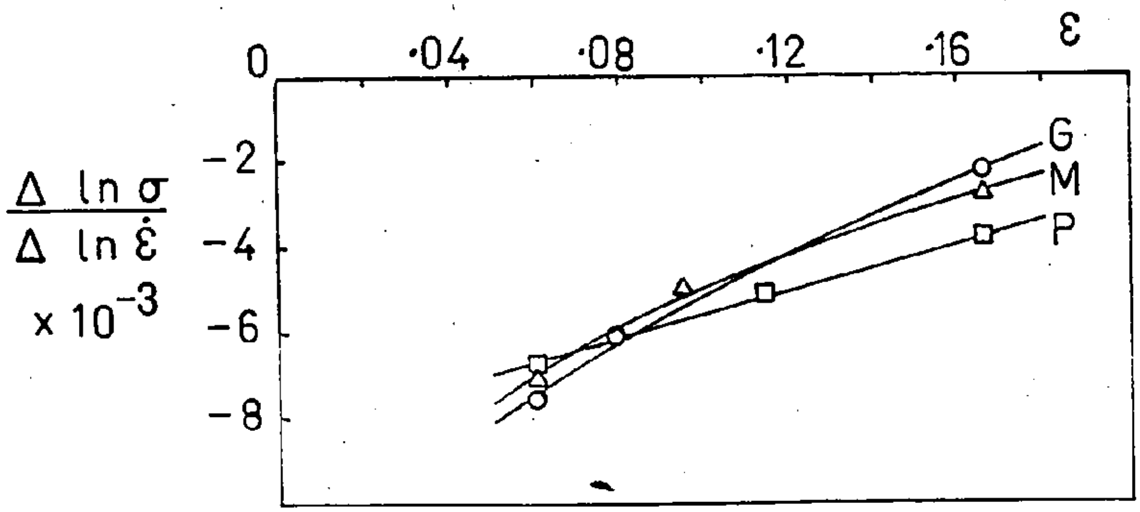

Figure 3-8 Strain rate sensitivity as a function of imposed strain during tensile testing of the three 2036-T4 materials.

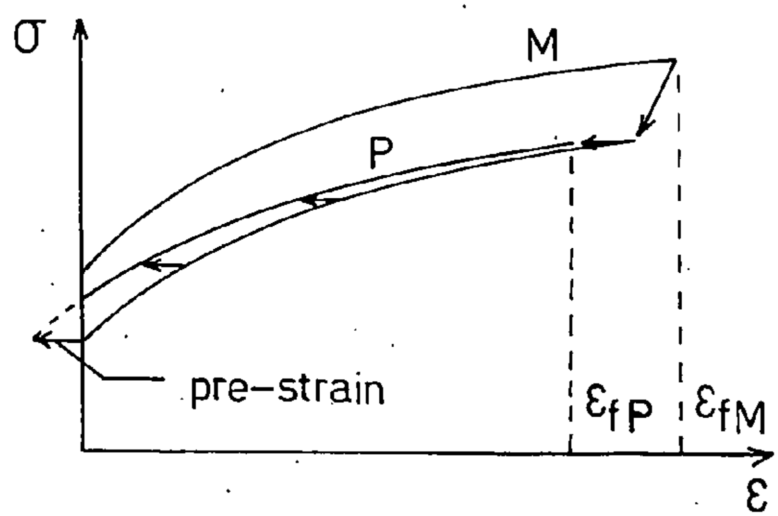

Figure 3-9 Schematic illustration in σ-ε space of a possible explanation for the properties of material P in comparison to material M.

Initial decrease in strength level is due to the decrease in volume fraction of zones.

microstructure occur among the three materials, their effect on the mechanical parameters is, for the most part, subtle enough to go unnoticed during routine quality control tests, and even the present, more detailed study does not allow unambiguous correlations to be made to explain the influence of all the microstructural constituents present.

The yield stress of a material is influenced by many factors, eg., grain size, solid solution level, ageing condition, and degree of prior strain hardening. Thus, to try to correlate the combined influence of all these variables with the observed differences in yield strength (approximately 15% between G and M) of the present materials is highly speculative. However, if it is assumed that the degree of solid solution hardening is equivalent in all three materials, then it is possible to make some order of magnitude estimates on the effects of grain size strengthening and precipitation hardening. Table 3-2 indicates the magnitudes of these strength increments. Obviously, the contribution by the grain size in aluminum alloys is very small, and the difference in grain size between the materials is insignificant compared to the effects of the hardening precipitates.

Theoretical estimates of the differences in shear stress due to the volume fraction of hardening precipitates (assumed to be mainly GP 1 zones) are of similar magnitude to the yield strength differences observed in Table 3-1. Note that materials M and P have the same strengthening increment, as expected from the similar Cu contents, but different observed yield strengths. It is suggested that this is partly due to the reduction in effective volume fraction of zones by the slack quench which introduced the grain boundary precipitates. No estimate of this

Table 3-2

Theoretical Contributions to the Critical Shear Stress (MPa)

MATERIAL	GRAIN SIZE EFFECT (a)	PRECIPITATION EFFECT (b)
G	14	108
M	15	123
P	16	123

(a) Based on grain size strengthening in pure Al with

$$\tau_G = 8 + 1.1\ d^{-1/2}\ \text{MPa} \qquad \text{(Embury, 1971)}$$

where d is the average grain size in mm.

(b) Based on the theory of Mott and Nabarro (1948), where

$$\tau_p = 2\ G|\varepsilon|f$$

where G is the shear modulus of the zone

ε is the coherency strain

f is the volume fraction of zones (as determined from the results of Beton and Rollason (1957-58) on the GP zone solvus in the Al-Cu system)

Note that this theory exhibits marked differences (at low volume fractions) from the theory of Brown and Ham (1971) where τ is a function of $f^{1/2}$.

reduction in yield stress was attempted because of the difficulties associated with determining the effective volume fraction of zones. It is also possible that small differences in the amount of pre-strain imparted by the straightening operation will cause minor variations in the yield stress, especially during the initially high work hardening regime. However, the transmission electron microscopy performed was not sufficiently elaborate to resolve such minor differences in dislocation content. Note that for typical initial work hardening rates of ≥ 2000 MPa, a yield stress increase of 20 MPa may result from a pre-strain of $\leq .01$.

Significant differences in the tensile strengths occur. This parameter reflects variations in the work hardening rate which could be due to differences in the type of hardening precipitate (i.e., the presence of non-deformable particles) or differences in the amount of pre-strain due to the straightening operation. It is likely that both these influences affect material P since electron microscopy revealed the presence of some large precipitates within the matrix, and the low uniform elongation of this material supports the pre-strain hypothesis. The similar n-values shown by materials G and M indicate that the volume fraction of deformable precipitate particles affects the yield strength much more than the work hardening rate (which is determined by the matrix characteristics as suggested in Chapter 2). A schematic illustration of the possible history of material P is shown in Figure 3-9. Further information on the effect of slack quenching will be provided later in this chapter.

The post-uniform ductility, and hence the total elongation, is influenced by the type and distribution of second phase particles. Table

3-1 indicates that the post-uniform ductility, as determined from the crude measurement of uniform elongation, is approximately constant (2%) for all materials. However, measurements of fracture strains give a more accurate estimate of this parameter and it will be seen (Chapter 4) that material P has the lowest post-necking strains, followed by M and then G. The low total elongation of material P is significantly affected by the presence of the grain boundary precipitates which supplement the already high volume fraction of constituent particles and lead to premature fracture compared to materials G and M. The higher constituent content of M (compared to G) will also be seen to affect the post-uniform ductility of this material. From the tensile test results, it appears that the presence of strings of constituent particles in materials P and M and variations in grain size of P, do not result in inferior transverse tensile properties, but these microstructural features may well have an influence on other deformation modes.

It is interesting to note that the regions of small grain size in material P follow the strings of constituents, i.e., the original interdendritic regions, while the large grains occur near the primary dendrite centres where the dispersoid concentration is expected to be highest. This suggests that the strings of broken constituent particles are more effective than the dispersoids in controlling the nucleation and growth of recrystallised grains. If the variations in chemistry between the materials are considered in relation to the grain structure, it is possible that a major influence on the uniformity of grain size and constituent particle distribution in material G can be traced back through the steps of thermal and mechanical processing to the influence of the high Ti content and the solidification conditions on the grain structure of the cast ingot.

It was shown earlier in this section that differences in the amount of grain boundary precipitate can arise as a consequence of variations in quenching rate. To elucidate the effects of slack quenching on uniaxial tensile parameters, tension tests were performed on specimens of materials G and P which had been re-solution treated, quenched at different rates, and subsequently aged to the T4 condition. Table 3-3 gives details of the thermal treatments employed to "modify" the structures of these materials. Table 3-4 gives their major tensile parameters. The primary purpose of these thermal modifications was to induce grain boundary precipitation in material G and remove it from material P. Further structural information, including micrographs, regarding these modifications can be found in Chapter 4.

Comparison of Tables 3-1 and 3-4 shows that the thermal treatment had little effect on material G but a significant effect on material P. Both the strength levels and elongation values increased following removal of the grain boundary precipitates from material P. This indicates the deleterious effects of these precipitates on elongation and suggests that their volume fraction can influence the strength level presumably by reducing the volume fraction of fine scale precipitates in the matrix. It is suggested that the absence of an appreciable change in the properties of material G could be the result of one or both of the following:

a) the thermal treatment used here did not adequately represent that experienced by material P during production,

Table 3-3

Thermal Treatments Employed
to Modify Structures of Materials G and P

	G	P
SOLUTION TREATMENT:		
Temperature (°C)	500	500
Time (hrs)	1	1
QUENCH	furnace door opened to allow air temp. to drop to 400°C in 1 minute	immediate quench into cold water from 500°C
NATURAL AGEING TIME	17 days	17 days

Table 3-4

Uniaxial Tensile Parameters (Longitudinal)
For Modified Materials

PARAMETER	G	P
Yield Stress (MPa)	197	217
Ultimate Stress (MPa)	350	385
Total Elongation (%)	22.9	23.6
Uniform Elongation (%)	21.2	22.0

b) due to some other factor, such as composition, the quench sensitivity of material G is not as high as for material P.

Both the uniform and post-uniform strains are affected by the strain rate sensitivity of a material (Hart, 1967; Ghosh, 1974), i.e., materials which possess significant positive rate sensitivity have increased ability to distribute strains. Values of the strain rate sensitivity parameter for the present alloys (Figure 3-8) are close to zero near the end of uniform deformation, and, although differences occur which are in qualitative agreement with elongation parameters, these differences are difficult to distinguish from the effects of the second phase particles within the materials.

CHAPTER 4

ASPECTS OF FORMABILITY

The formability of 2036-T4 is considered in terms of its uniform deformation and strain localisation effects in three proportional straining modes of deformation. Fractographic analysis provides evidence of the influence of microstructural features on the fracture event. The effect of a basic microstructural modification on the behaviour in bending is also discussed.

4.1 Forming Limit Diagrams and Fracture Maps

4.1.1 Experimental Techniques and Results

Approximate forming limit diagrams for each batch of 2036-T4 were determined from a uniaxial tension test, a hydraulic bulge test with a circular die, and a Hecker-type punch test designed to achieve deformation close to plane strain tension. Although the punch test introduced friction as an additional variable in the plane strain deformation, resulting in a higher limit strain than would have been achieved by a frictionless plane strain test, it was assumed that consistent lubrication conditions would not affect the relative ranking of the materials in this strain path, and, thus, the production of an approximate F.L.D. would allow viable comparisons to be drawn between the materials investigated. Prior to testing, the specimens were gridded with either 2.18 mm or 0.83 mm (nominal) diameter circles by the use of a diazo (photogrid) technique. Determination of surface strains was accomplished with a toolmakers microscope. The sources of error associated with the development of F.L.D.'s; i.e., circle position, original gauge length, and strain gradient; have been discussed by Wycliffe (1977) and will not be included in the present discussion. In this study, the limit strains were determined by measurements of deformed circles as close as possible to, but not inside, any necked region. Thus, the curves presented are lower limits to the actual F.L.D.

Fracture maps for each of the materials were determined by measuring the minor surface strain at fracture (ε_2), the thickness strain at fracture (ε_3), and then computing the major strain (ε_1), assuming constant volume deformation;

$$\text{i.e.,} \qquad \varepsilon_1 + \varepsilon_2 + \varepsilon_3 = 0. \qquad (4\text{-}1)$$

For fractures in uniaxial and equi-biaxial tension, the fracture thickness was measured by viewing the fracture surface normal to the sheet thickness direction and averaging the observed thickness, as shown in Figure 4-1(a). Plane strain fracture thicknesses were measured by metallographic preparation of cross-sections of the fracture (Figure 4-1(b)) for tests with the 2.18 mm grid circles, and by measuring the minimum thickness observed in the method of Figure 4-1(a) for tests with the 0.83 mm grid circles. These methods were adopted to indicate the differences obtained by different measuring techniques. It was found that the method of Figure 4-1(a) could sometimes lead to significant inaccuracy for the rigid punch (plane strain) tests because the nature of the fracture often resulted in the formation of a lip of material in region A of Figure 4-1(b), which gave a false indication of the fracture thickness.

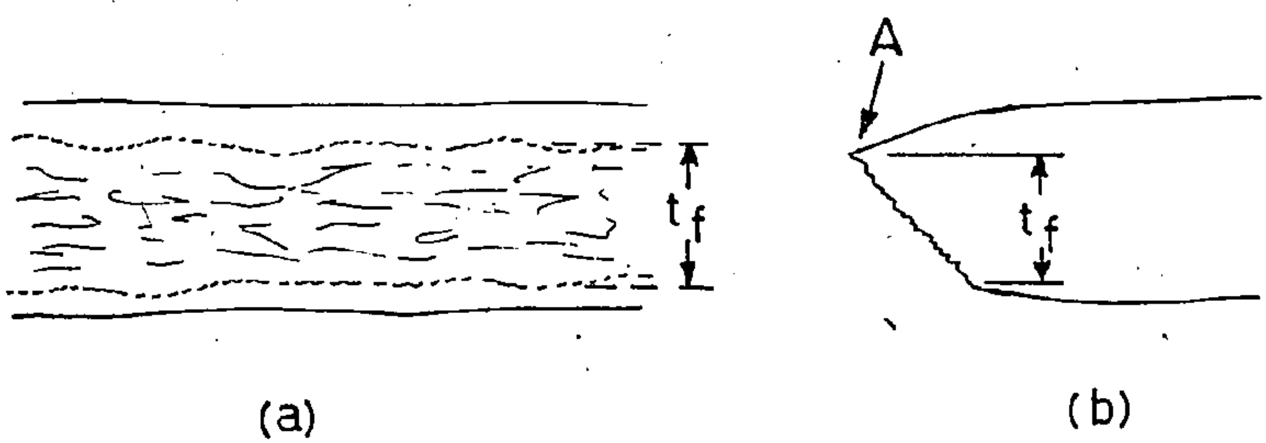

Figure 4-1 Schematic diagram illustrating the methods of measurement of fracture thickness.

Figure 4-2(a) illustrates the approximate F.L.D. and fracture map for each of the three 2036-T4 materials gridded with 2.18 mm diameter circles. Each point is the average of measurements of strain on at least two tests in uniaxial tension and plane strain, and up to five tests in equi-biaxial tension. The range of major and minor limit strains measured indicates that these points are accurate only to within approximately ±5-6%. Hence, the range of the approximate F.L.D. for each material is similar to the range over which the three materials vary. The range of minor strains at fracture is smaller (±2%), but the range of thickness strains is ~±6%, hence, the accuracy of the points in the fracture maps is slightly less than for the F.L.D. The data have also been plotted to indicate the direction of the fracture for the plane strain and bulge testing, and the orientation of the tension test relative to the rolling direction of the sheet. This was found to be necessary as the direction of fracture had a significant influence on the fracture thickness strain, especially for bulge testing.

A further complication arises in regard to the bulge test. The major strain in the polar region was always in the rolling direction regardless of which direction the fracture occurred. Hence, the points in the fracture maps denoted "||RD" represent local values of strain which differ from the limit strains in terms of their major and minor directions.

The important point to note in this diagram is the relative separation of data in the F.L.D.'s and the fracture maps. There is little distinction between the F.L.D.'s for the three materials, although it is clear that material P lies on the lower side of the band.

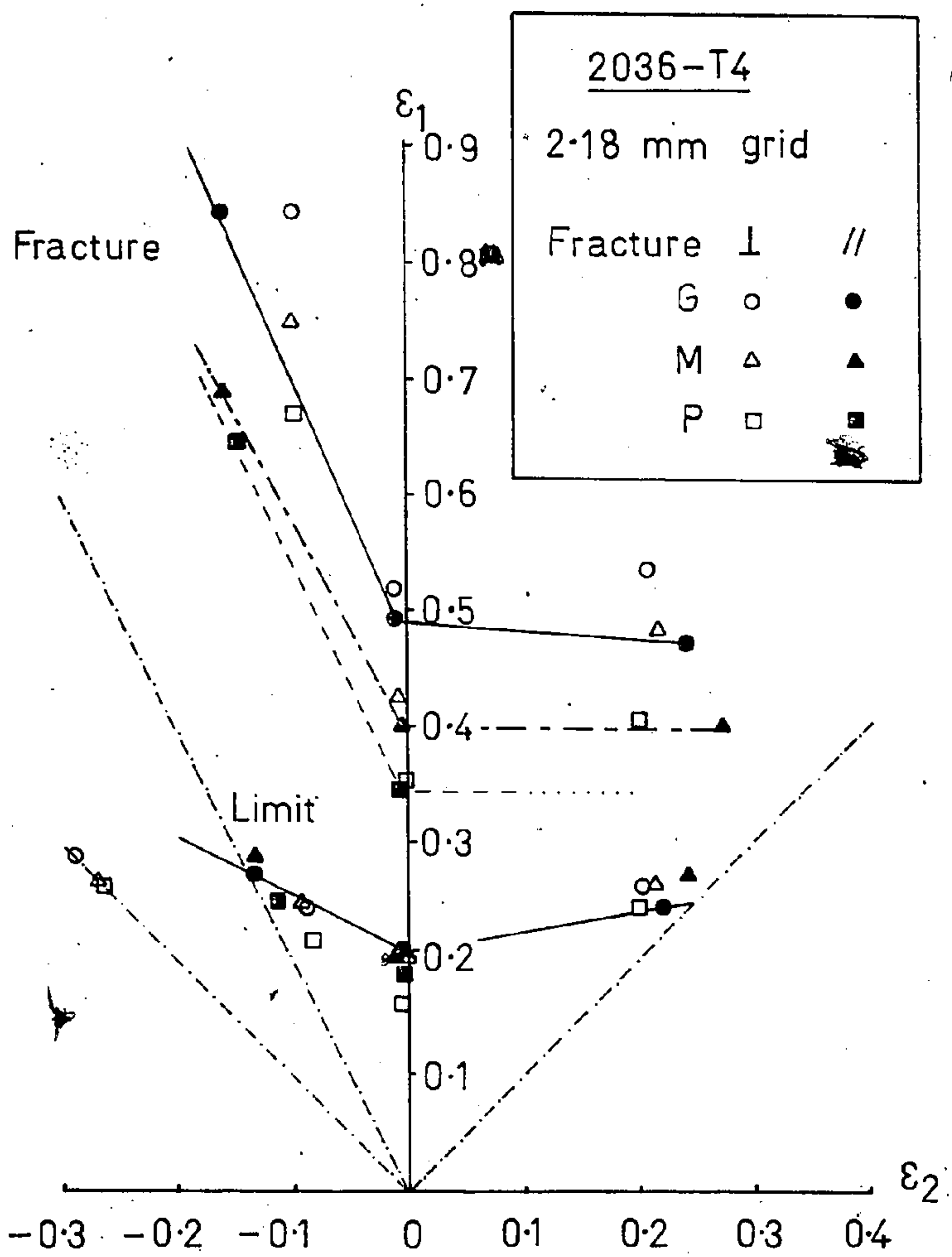

Figure 4-2(a) Approximate F.L.D.'s and fracture maps for 2036-T4 materials gridded with 2.18 mm diameter circles. Points represent average strains measured on specimens with fractures parallel (//) or perpendicular (⊥) to the rolling direction. For tensile tests, these symbols imply that the tensile axis is perpendicular and parallel to the rolling direction respectively. Fracture maps have been drawn only through (//) data points. Note that material P exhibited no (//) fractures.

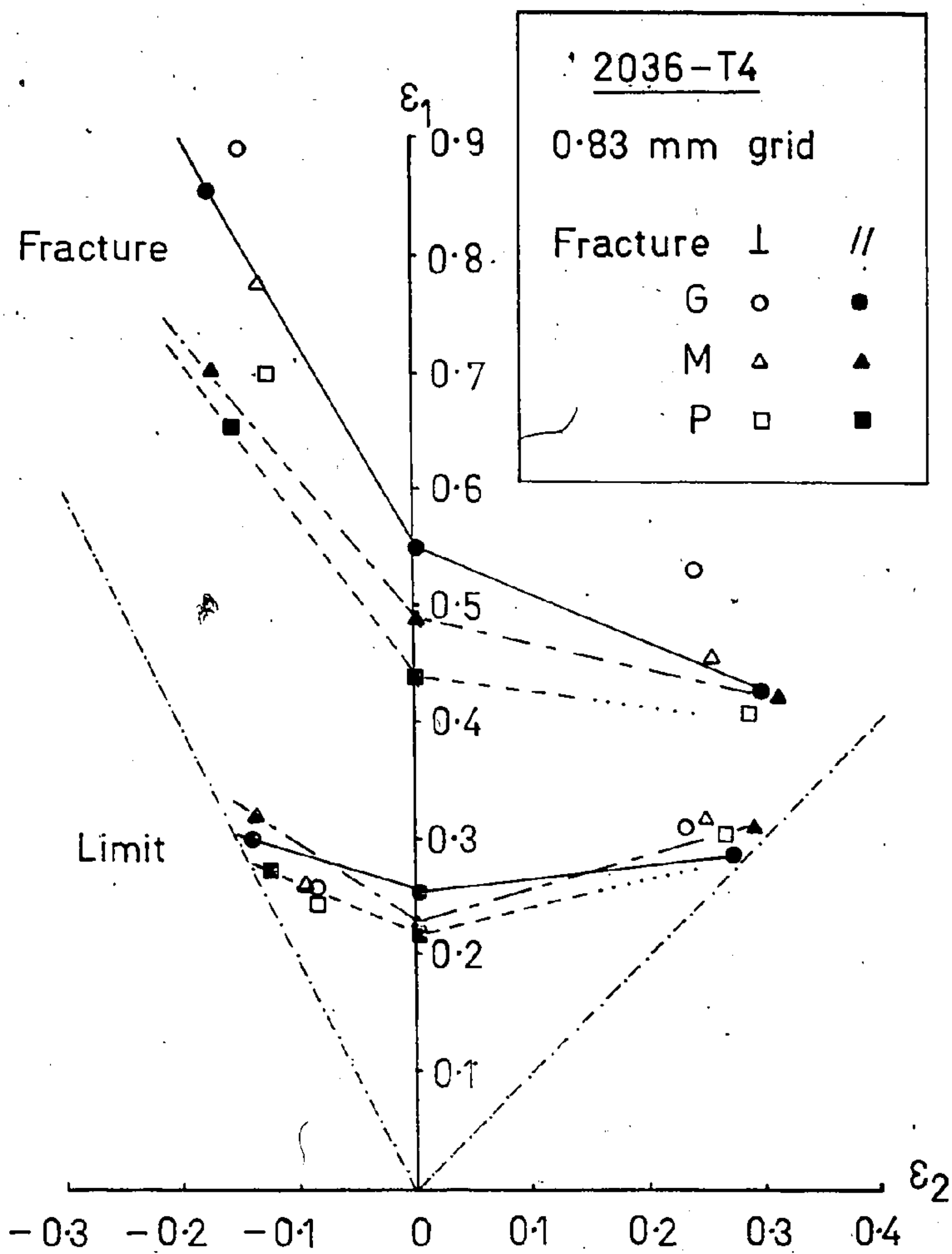

Figure 4-2(b) Approximate F.L.D.'s and fracture maps for 2036-T4 materials gridded with 0.83 mm diameter circles. Points represent average strains measured on specimens with fractures parallel (//) or perpendicular (⊥) to the rolling direction. For tensile tests, these symbols imply that the tensile axis is perpendicular and parallel to the rolling direction respectively. Fracture maps have been drawn only through (//) data points. Note that material P exhibited no (//) fractures.

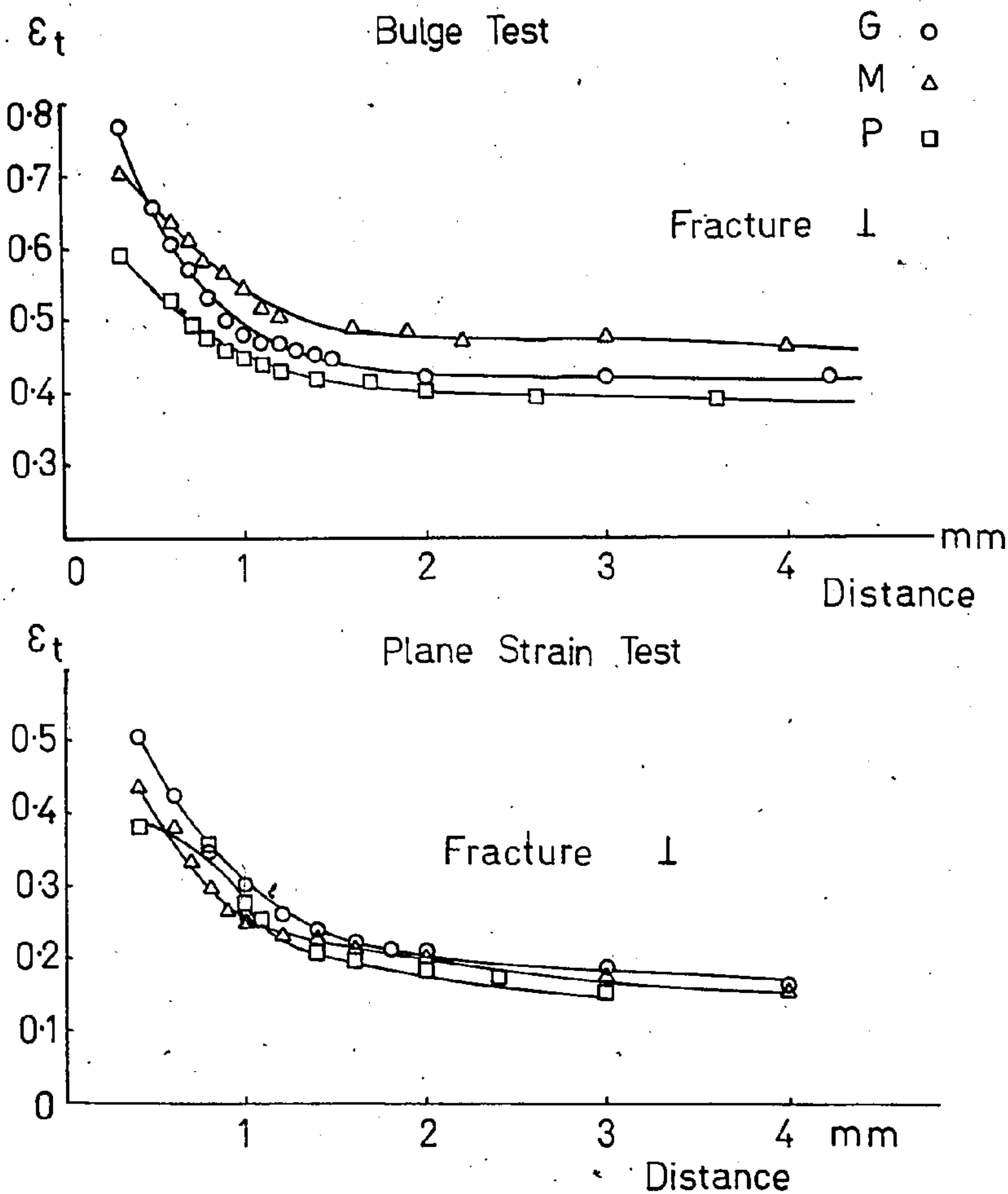

Figure 4-3 Thickness strain profiles at fracture for bulge test and plane strain test specimens of 2036-T4.

However, the fracture maps clearly distinguish between the materials in all modes of deformation; material G exhibits the largest strains to fracture and material P the smallest. The separation of the F.L.D.'s and fracture maps reflects the amount of post-necking ductility associated with each material. It is significant to note that, during bulge testing, material P did not fracture parallel to the rolling direction, while materials G and M showed approximately equal division between parallel and transverse fractures. Average fracture strains associated with in-plane shear (torsion) deformation (Marciniak, 1974) are also shown in Figure 4-2(a) which indicate the low resistance to shear deformation of alloy 2036-T4, but do not provide an effective distinction between the three lots of material being studied.

Figure 4-2(b) shows the F.L.D.'s and fracture maps determined with grid circles of 0.83 mm diameter. The use of these smaller grid circles allows more accurate determination of surface strains in regions of high strain gradient, and results in an increase in the general level of the F.L.D.'s. The fracture maps indicate similar trends to those in Figure 4-2(a), and need no further comment. However, the F.L.D.'s now show a feature which was not evident when using the larger grid circles. It appears that the F.L.D.'s for materials G and M cross each other, and, although this tends to be supported by the thickness strain profiles of Figure 4-3, it is impossible to correlate this to any structural evidence. Hence, this feature is not considered to be significant to the present comparison of materials.

4.1.2 <u>Discussion</u>

Clearly, the three lots of alloy 2036-T4 are most easily distinguished on the basis of their fracture maps, while the F.L.D.'s, particularly those determined with the larger diameter grid circles, show little difference in comparison with the observed differences in press performance. The fact that the levels of the fracture maps correlate with the relative ratings of press performance suggests that the press performance in this case is dependent on the fracture properties and the post-uniform ductility of the materials, rather than the limit strain characteristics. In this respect, it is suggested that those microstructural features which influence the localisation of strain is one of the factors which determine the success or failure of production of the component. Attempts to delineate these microstructural features will be the subject of subsequent sections of this chapter.

The limited ability of 2036-T4 to sustain deformation in pure shear has been noted previously (leRoy, 1978), and there is evidence to suggest that this is a failure mode in many age-hardenable aluminum alloys in the naturally aged and peak-aged conditions (Embury, 1979a). The value of including fracture data from torsion tests is evident here because without these additional points on the fracture map, it is very difficult to distinguish between the fracture criteria of maximum principal stress, maximum shear stress, and constant thickness strain (Glover et al, 1977).

Hydraulic bulge testing of the materials gave evidence of a particular form of inhomogeneous deformation which was manifest only at large strains (approaching fracture). The extent of this mode was dependent on the material tested. This inhomogeneous deformation occurred as small variations in sheet thickness about 1-2 mm in width, parallel to the rolling direction as shown in Figure 4-4. Qualitative observation of the extent of the "roping" phenomenon showed that material G contained the most roping while material P contained virtually none. Fractures which occurred along the rolling direction tended to follow one or more of these roping lines. However, the presence of roping did not preclude transverse fractures. Nevertheless, it is pertinent that material P, which contained the least amount of roping, did not exhibit fracture in the folling direction. Roping phenomena have also been observed in pure aluminum sheet (Tadros and Mellor, 1978), Al-Mn alloys (Wycliffe, 1977), and in Al-Mg-Si alloys by the present author, but the origin of these lines is uncertain. Optical metallography performed on the deformed material showed nothing to which the roping could be attributed.

The observation that the major surface strain in the vicinity of the pole of the bulge test always occurred in the rolling direction, has been noted also by others (Bird, 1979) for aluminum alloys. Tadros and Mellor (1978) observed that soft aluminum sheet exhibited slightly higher limit strains when the material was stretched in an elliptical die with its rolling direction along the minor axis of the ellipse; i.e., limit strains were higher in the rolling direction; but that steel and brass sheets were hardly affected by changing specimen alignment. It is possible that this effect is due to the development of planar anisotropy by textural changes during straining. However, the influence of inhomogeneous deformation such as occurs in roping, cannot be disregarded, and further investigation will be needed in this respect.

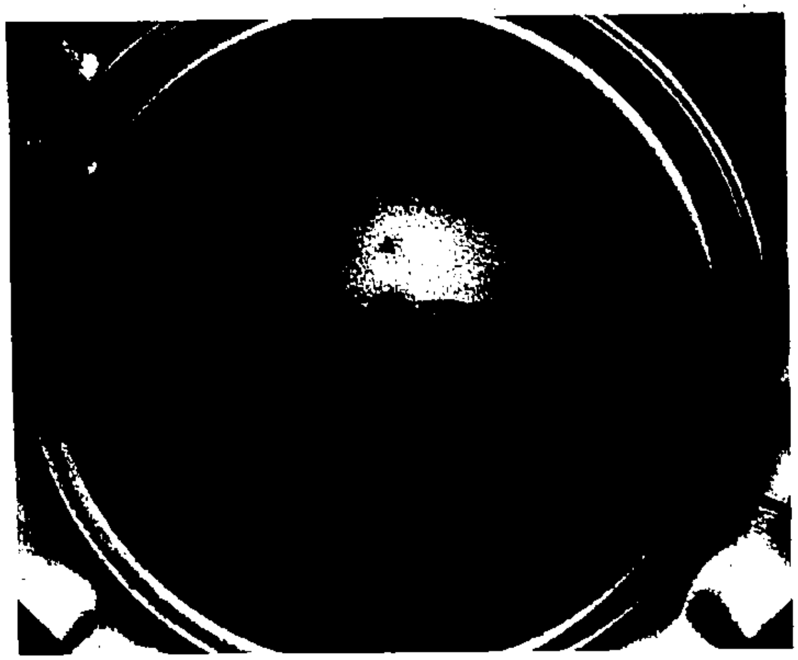

Figure 4-4 "Roping" phenomenon parallel to the rolling direction in 2036-T4 sheet deformed by hydraulic bulging. Fracture is also parallel to the rolling direction in this case.

4.2 Fractography

Fractography of the 2036-T4 materials was performed on a Cambridge scanning electron microscope. It was found that there were significant effects on the details of the fracture surfaces due to the strain path and the material, although in all cases, the 2036-T4 failed in a macroscopic shear mode.

The microstructural effects on fracture may be observed by reference to Figure 4-5, which illustrates typical uniaxial tensile fracture surfaces for each of the three 2036-T4 materials. Large, deep dimples correspond to voiding around the large constituent particles, while the numerous small, shallow dimples represent void sheets formed by decohesion or cracking of the dispersoid particles. Both materials G and M exhibit relatively large dimples indicating significant growth of these voids prior to fracture, but material P shows only limited void growth prior to fracture. This suggests that the high volume fraction of constituent particles allows relatively little void growth before the linking condition is reached, that some event other than void linkage (eg., grain boundary separation) determines the fracture event, or that a combination of these conditions is operative.

Fracture surfaces of bulge test specimens and plane strain specimens exhibited regions of both predominant shear and fibrous failure in any given specimen. An example of this is shown in Figure 4-6, taken from a bulge test fracture of material G. It appears that the final shear failure occurs between heavily voided regions of locally high constituent volume fraction. Figure 4-7 shows regions of extensive void growth from bulge test fractures of materials G and P. Note again the

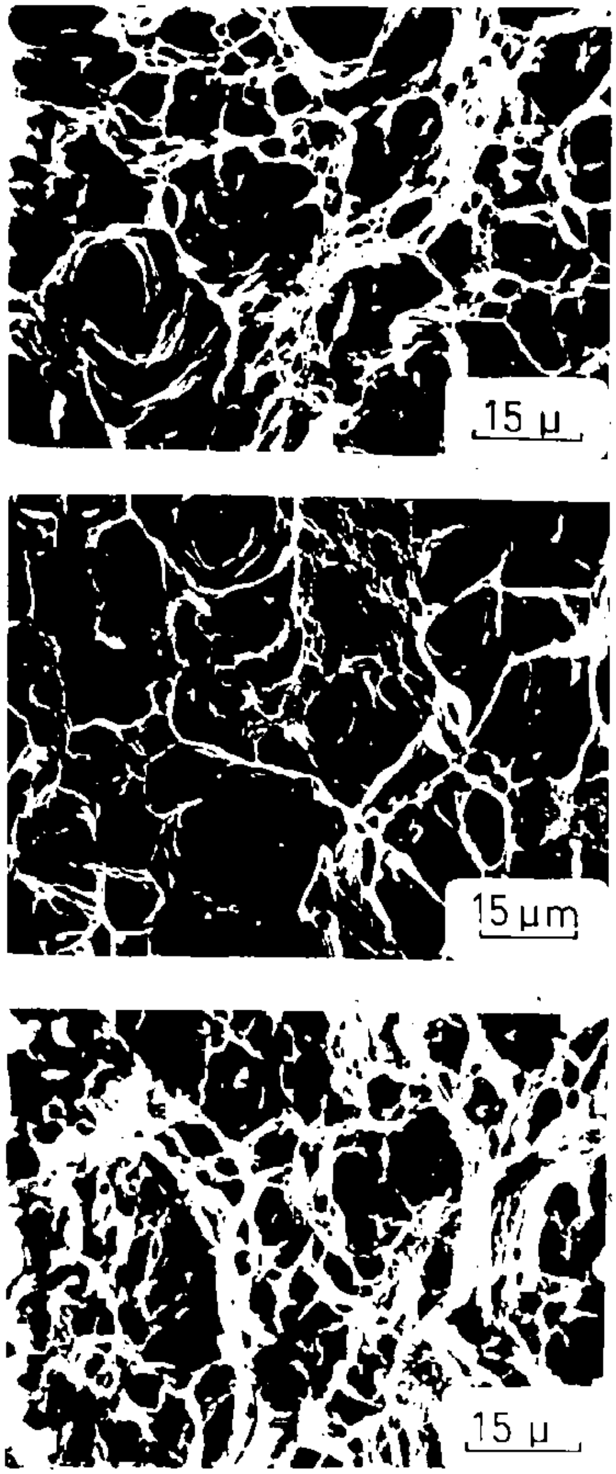

(a)

2036 T4

Tensile

Fractographs

(b)

(c)

Figure 4-5 Tensile fractographs for 2036-T4 materials (a) G, (b) M, (c) P.

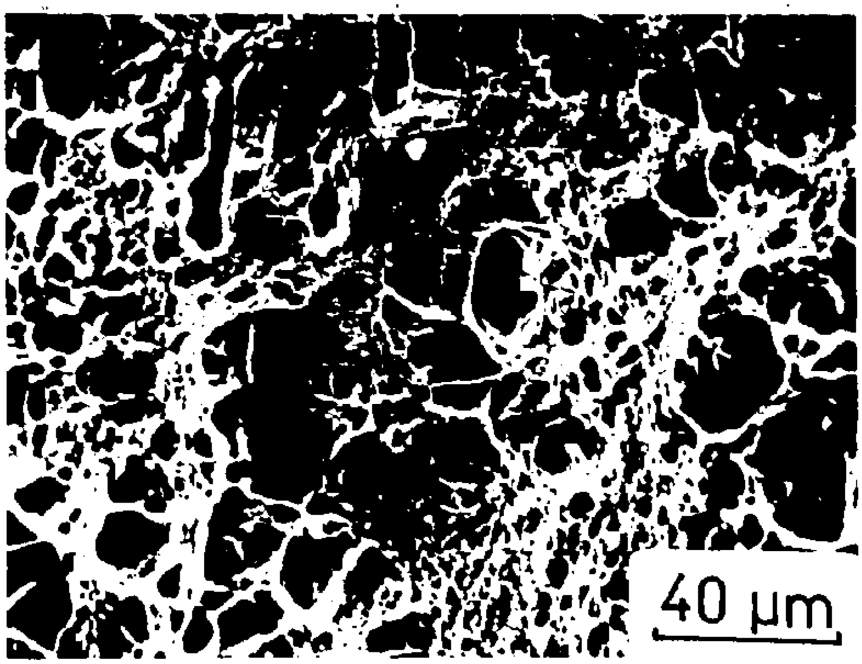

Figure 4-6 Bulge test fractograph of material G. Shear failure has occurred between regions of extensive void formation.

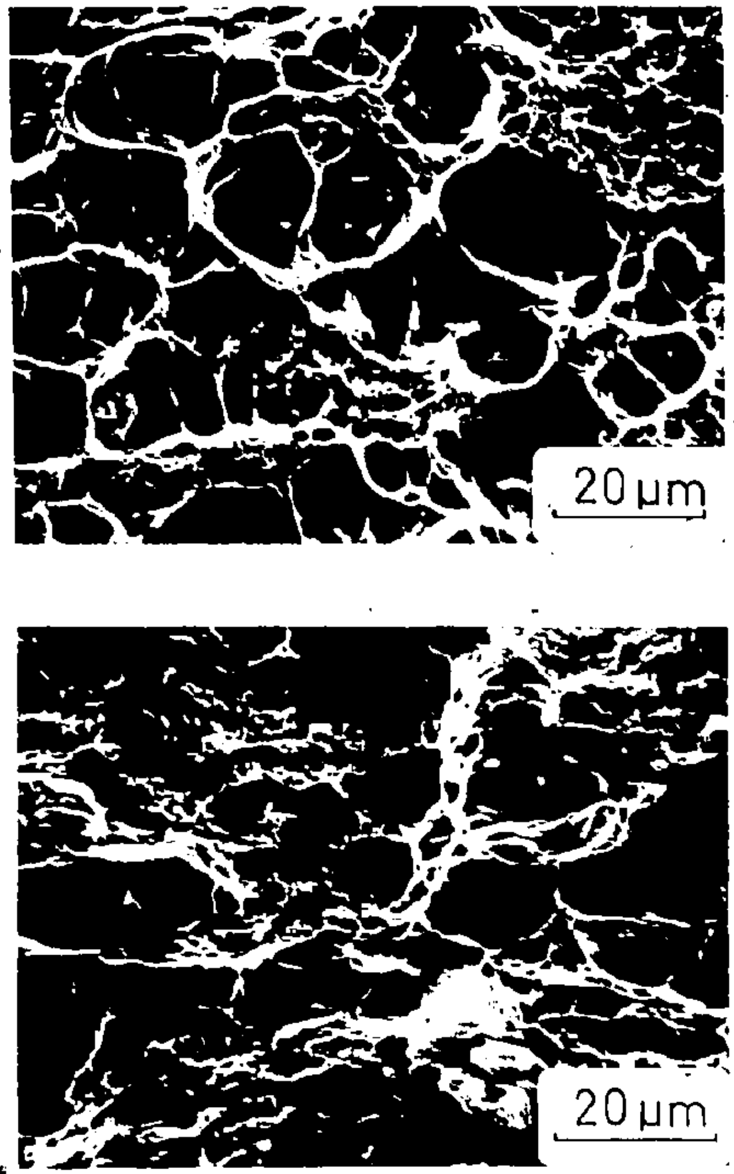

2036 T4.

(a)

Bulge Test

Fractographs

(b)

Figure 4-7 Regions of extensive voiding from bulge test fractures of materials (a) G and (b) P.

absence of void sheeting in material P and the generally smaller size to which the voids grow. The extent of local shear failure in material P also appeared to be higher.

Observation of the plane strain fracture surfaces of materials G and M showed the types of features described above. For material P, however, there were additional regions of a type illustrated in Figure 4-8(a). These regions had the appearance of intergranular failure. Thus, one possible implication is that the grain boundary precipitation in this material plays a significant role in determining its fracture characteristics, particularly when fracture occurs in plane strain deformation. A portion of the plane strain fracture surface of material M is shown for comparison in Figure 4-8(b).

It is generally accepted (Embury and Nes, 1974) that grain boundary precipitation influences fracture by a maximum principal stress criterion. However, in the present case, it is impossible to distinguish any effect of this criterion on the nature of the fracture map since both the maximum principal stress criterion and the maximum shear stress criterion have similar shapes in both stress and strain space between the limits of uniaxial tension and equi-biaxial tension (Glover et al, 1977). Thus, any change in the level of the fracture map could be attributed to either the presence of grain boundary precipitates or increased susceptibility to shear failure within the matrix.

Previous mention has been made of the fact that the fracture direction in the bulge test markedly influenced the fracture thickness strain. Fractures along the rolling direction were associated with smaller thickness strains than fractures in the transverse direction,

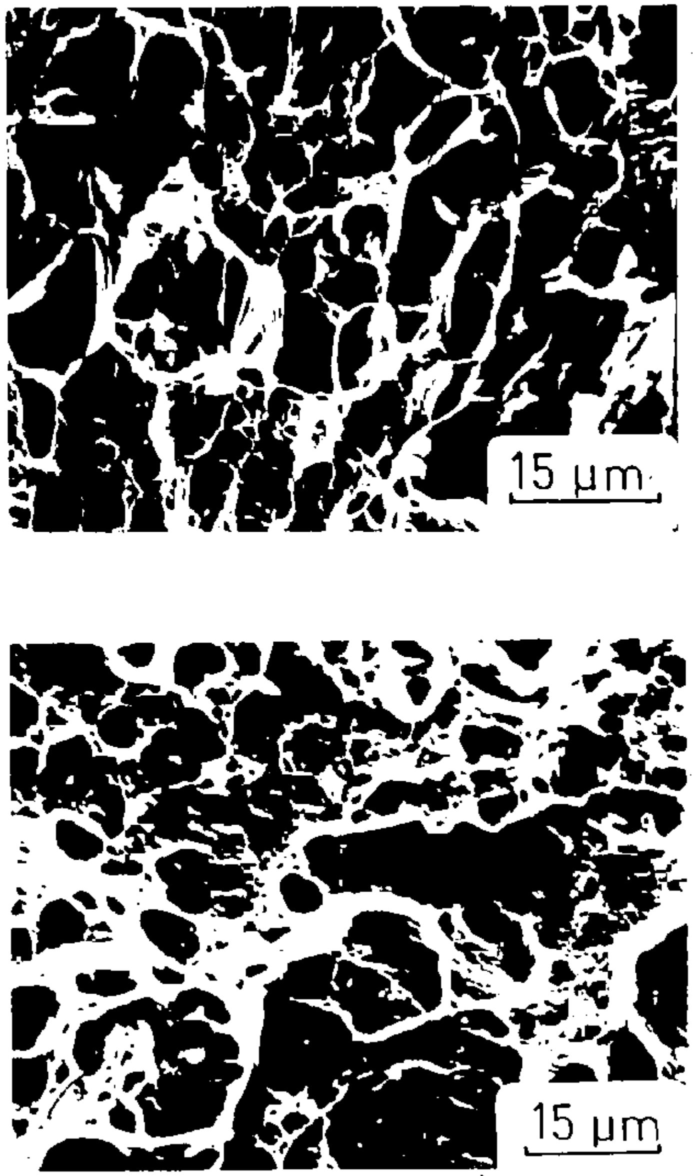

2036 T4

(a)

Plane Strain

Fractographs

(b)

Figure 4-8 Plane strain test fractographs, (a) material P; sheet-thickness direction horizontal; (b) material M; sheet thickness direction vertical.

and this was assumed to be due to the influence of the roping phenomenon on fracture. Fractographic analysis of failures in both directions in material G indicated that the longitudinal fractures showed more evidence of shear failure than the transverse fractures. Figure 4-9 shows portions of these fracture surfaces. Hence, it is suggested that the material within one of these roping lines is more susceptible to shear failure than adjacent material. The origin and consequences of this type of inhomogeneous deformation is clearly an area in need of further investigation.

4.3 Simple Bending Deformation of 2036-T4

The significance of bending deformation on the formability of sheet materials, and the correlation of "bendability" parameters with other mechanical properties has been discussed in Chapter 2. In this section, the results of simple bend tests are presented, together with the influence on bendability of a simple microstructural modification. In all cases, the bending deformation was achieved by a manual wrap-around operation with the angle of bend being 180°.

Figure 4-10 indicates the qualitative differences between the three lots of as-received 2036-T4 after the bending operation described above. Severe localisation of deformation occurs in material P, resulting in the formation of a single, deep crack parallel to the axis of the bend. On the other hand, material G appears to be able to distribute the deformation around the circumference of the bend, thus preventing the nucleation of a crack at the outer surface. Material M also exhibits the localisation of deformation, but not to the extent shown

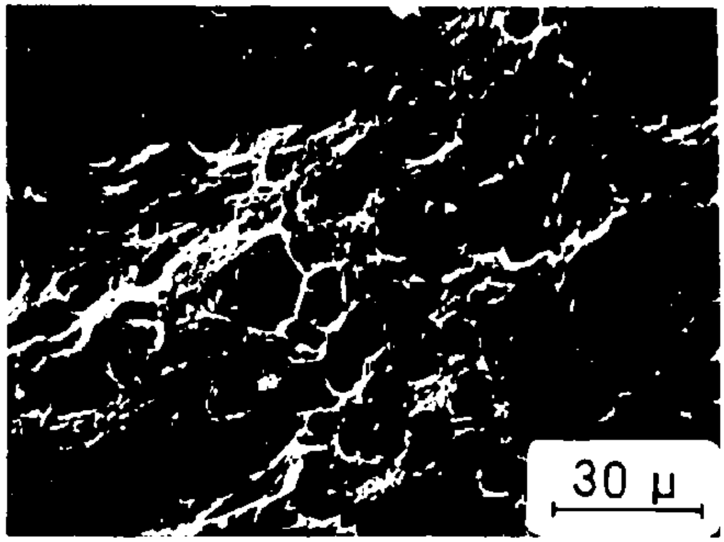

Parallel to Rolling Direction

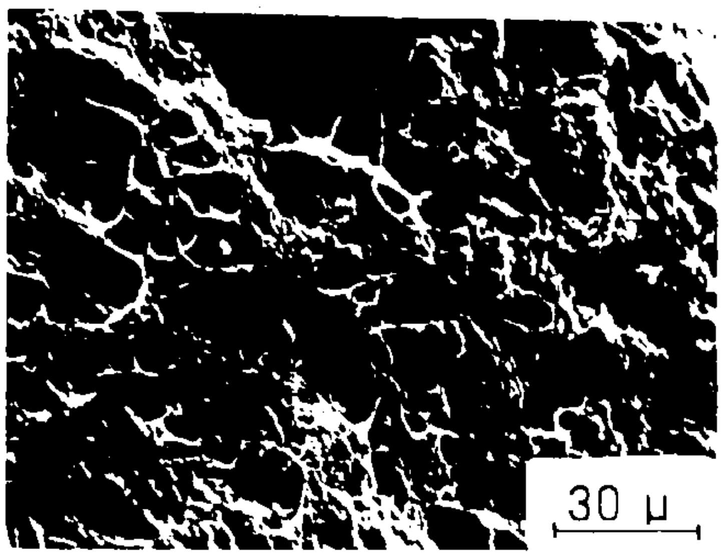

Perpendicular to Rolling Direction

2036-T4 , G .

Bulge Test Fracture Surfaces

Figure 4-9 Bulge test fracture surfaces, material G.

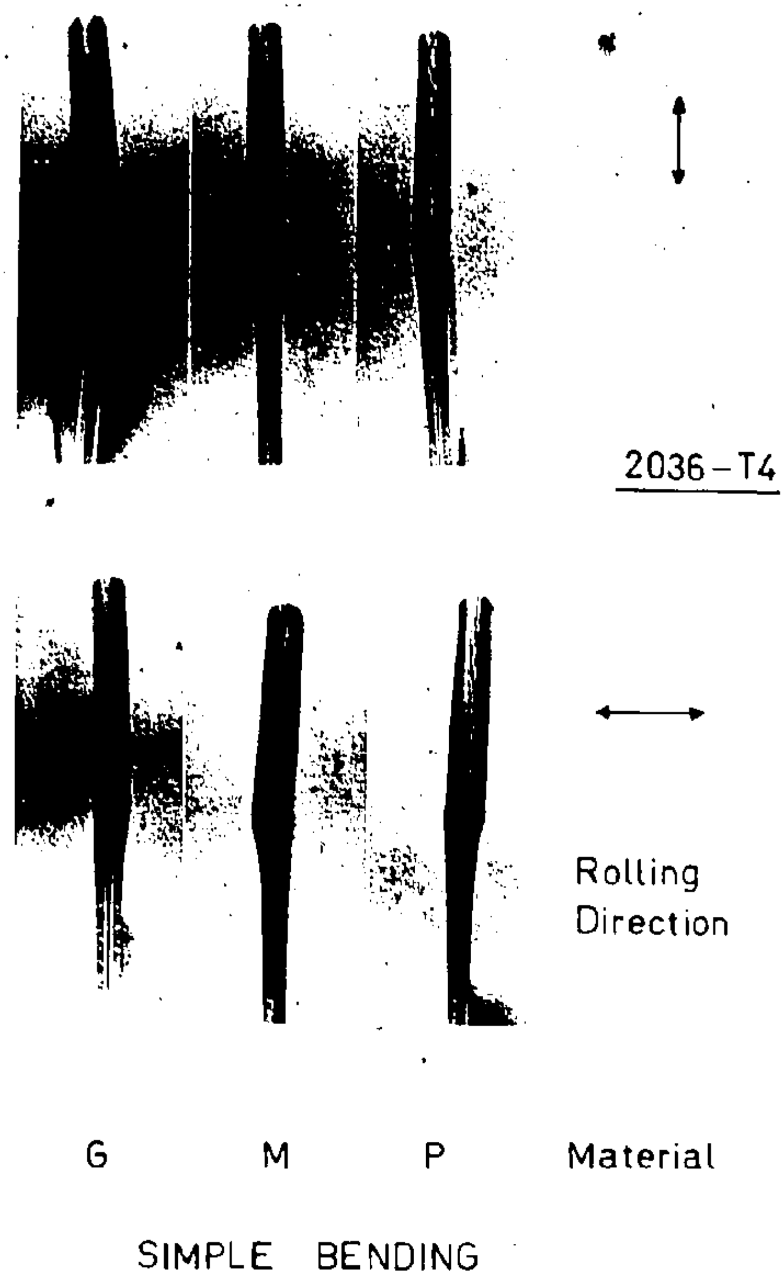

Figure 4-10 Surface appearance of 2036-T4 materials subjected to a simple bending operation.

by material P. This simple test can thus provide a useful qualitative indication of the bendability of these materials.

During bending deformation, the outer surface of the specimen experiences plane strain tension deformation provided the width to thickness ratio of the specimen exceeds approximately 10:1. If minimum bend radius tests are carried out under such conditions that the development of a major surface flaw constitutes failure of the material to form the bend, it may be possible to correlate the plane strain tension fracture characteristics and the minimum bend radius achieved. To check this hypothesis with the current materials, it was decided to incorporate plane strain fracture data into the formulation developed by Datsko and Yang (1960) for the prediction of the minimum bend radius. Because the basis for this equation is simply a maximum tensile strain criterion applied to the outermost fibre of the bend specimen, any definition of this true fracture strain is a valid starting point and hence, plane strain tension reduction in area/thickness parameters can be substituted directly into Equation 2-6 in place of the uniaxial tensile reduction in area used by the above authors.

Results of the calculations are shown in Table 4-1, where extra data available from Alcoa and Alcan research laboratories have been utilised to aid in the comparison of the materials. Average values of area reduction parameters from Alcoa laboratories and thickness reduction parameters from McMaster laboratories were used to determine the minimum bend radii for the three materials. These were then compared to the bend test results determined by Alcan laboratories. This test incorporated a bend angle of 135°, and a failure criterion of surface

Table 4-1

Calculation of Minimum Bend Radius (R/t)
From Fracture Strain Data

TEST	MATERIAL					
	G		P		M	
	Redn.	R/t	Redn.	R/t	Redn.	R/t
*Alcoa Tensile	59	0.20	56	0.24	54	0.27
*Alcoa Plane Strain	38	0.62	28	1.08	32	0.86
†McMaster Tensile	51	0.32	40	0.56	42	0.51
†McMaster Plane Strain	41	0.53	30	0.96	33	0.81
Alcan Min. Bend (135°)		0.6		1.0		0.6

* percent reduction in area (method of determination unknown)

† percent reduction in thickness (based on data in Figure 4-2(a))

cracking in the specimen. It is obvious that the plane strain fracture data predict more accurate values of the minimum bend radius than do the tensile reduction data, hence, it is suggested that the plane strain ductility may provide a useful formability index, particularly where small radius bending is critical, eg., in hemming operations.

The effects of structural modifications of materials G and P in terms of their uniaxial tensile parameters have been discussed in Chapter 3. The effects of these modifications on the microstructures of these materials are clearly seen in Figure 4-11. The thermal treatment has basically changed the amount of grain boundary precipitation in each material. Figure 4-12 illustrates the change in the surface features of small radius bend specimens as a result of the structural modifications. Pairs of specimens were bent together so that both received and same degree and rate of deformation. Clearly, the introduction of grain boundary precipitation in material G, and its associated decrease in the local volume fraction of zones in the T4 condition, has promoted the development of severe localisation of deformation in the form of a single major surface crack. Conversely, the removal of these precipitates from material P has allowed a more uniform distribution of strain around the circumference of the bend, although it has not entirely removed the tendency to localise strain. The mechanism by which strain can condense into a very localised region, such as a surface crack in a bend specimen, will be discussed in the next section. However, it is germane to note the implications of such a simple test as this in the study of quench sensitivity of age-hardenable aluminum alloys. The development of a small radius bend test with an accurate determination of the failure

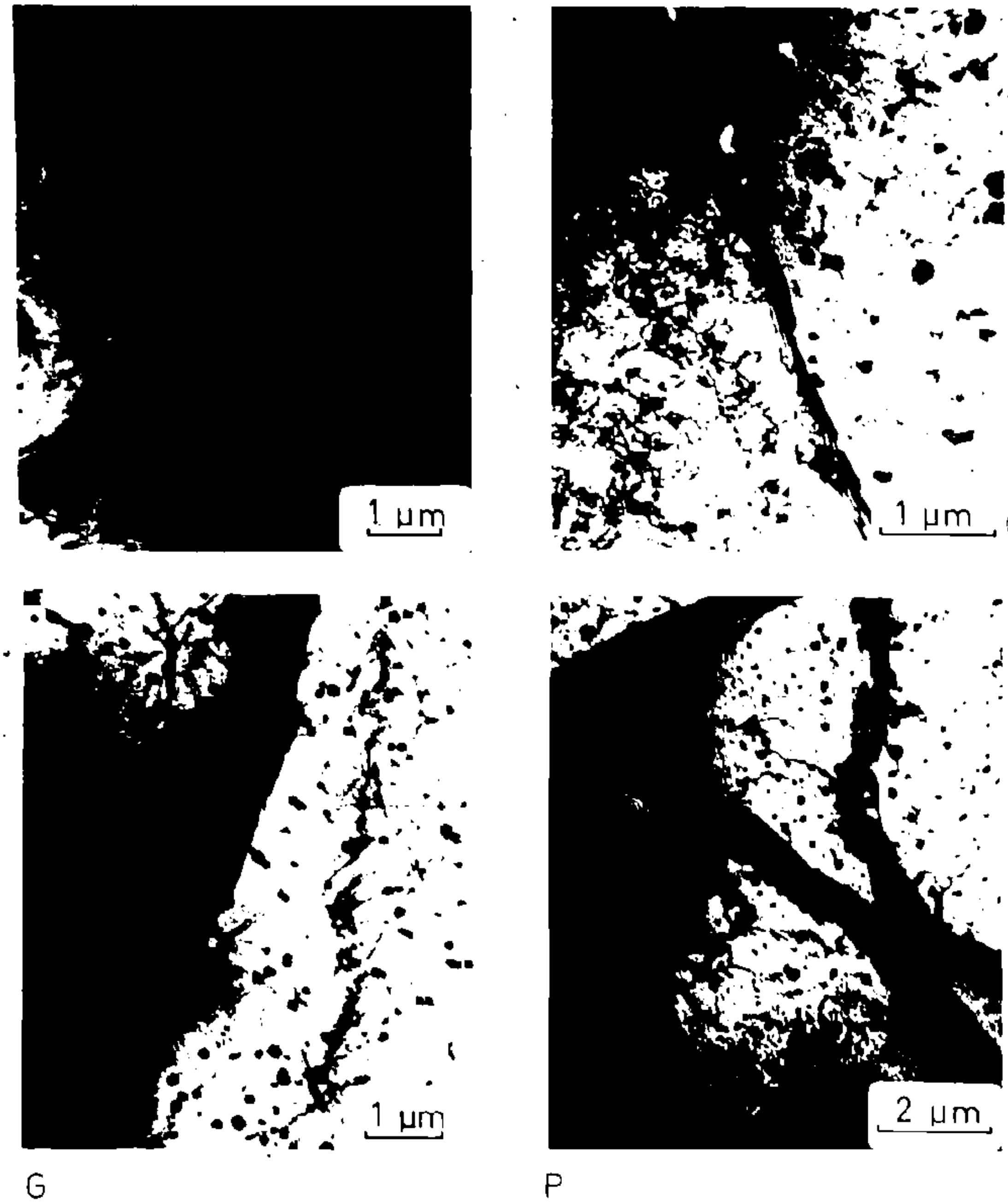

T.E.M. showing as-received (above) & modified (below).

Figure 4-11 Effect of thermal treatments on the fine structure of materials G and P.

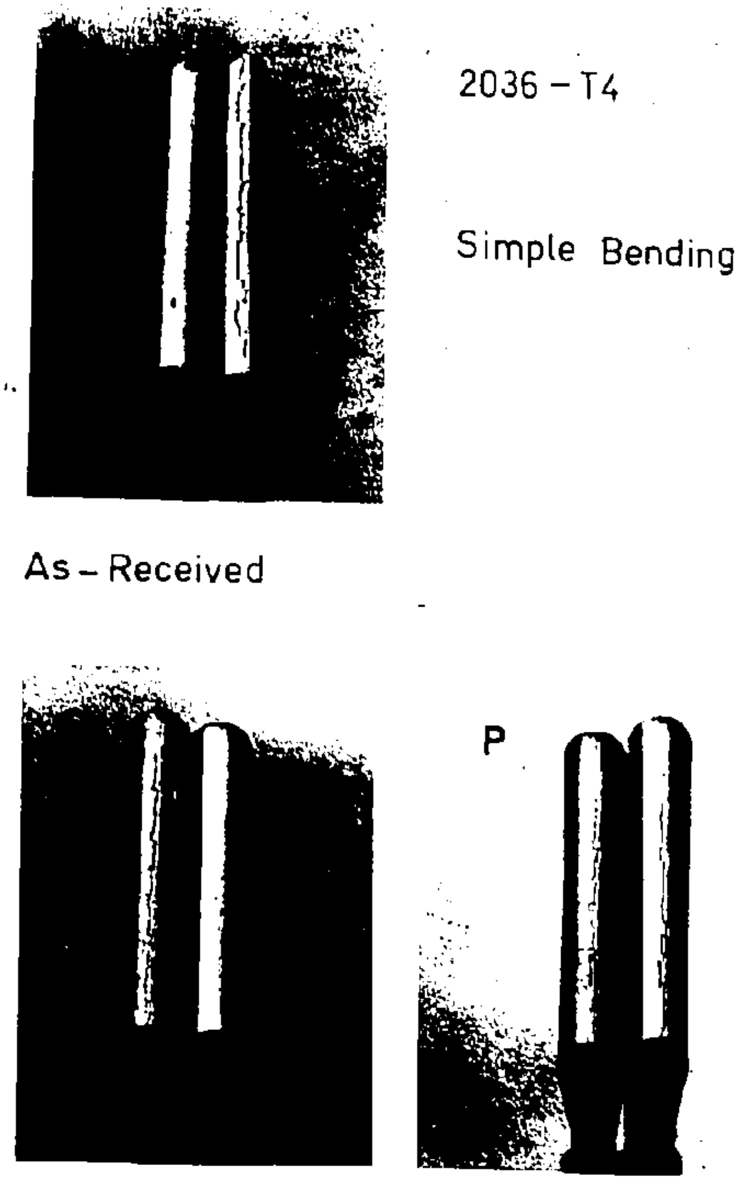

Figure 4-12 Change in surface features of small radius bend specimens following structural modifications.

point could be extremely useful in comparing the quench sensitivities of different alloys, and also as a production quality control device to check on the effectiveness of the solution treatment and quenching operation.

4.4 Strain Localisation

Two forms of heterogeneous deformation can be distinguished during large strain deformation of alloy 2036-T4. These are the growth and linking of voids as described in Chapter 2 and evidenced in the fractographs presented in Section 4.2, and the development of coarse slip and its subsequent condensation into fracture events. Evidence for coarse slip and resultant "superband" formation in aluminum alloys was reviewed in Chapter 2 and the influence of this on fracture characteristics of 2036-T4 will now be discussed.

Simple bend tests on polished specimens of materials G and P allowed the development of heterogeneous deformation to be followed through to the critical condition of condensation into a major fracture event. Early deformation showed events which have previously been described by Hahn and Rosenfield (1975), i.e., cracking of some of the large constituent particles, deformation in the vicinity of some of the grain boundaries due to grain rotation, and development of bands of coarse slip. Up to the stage of the coarse slip, both materials showed similar deformation events. However, once the localisation of slip occurred, more incipient cracks were noted in material P, especially where the bands of deformation impinged on grain boundaries.

Figure 4-13 shows the surface deformation experienced by mater-

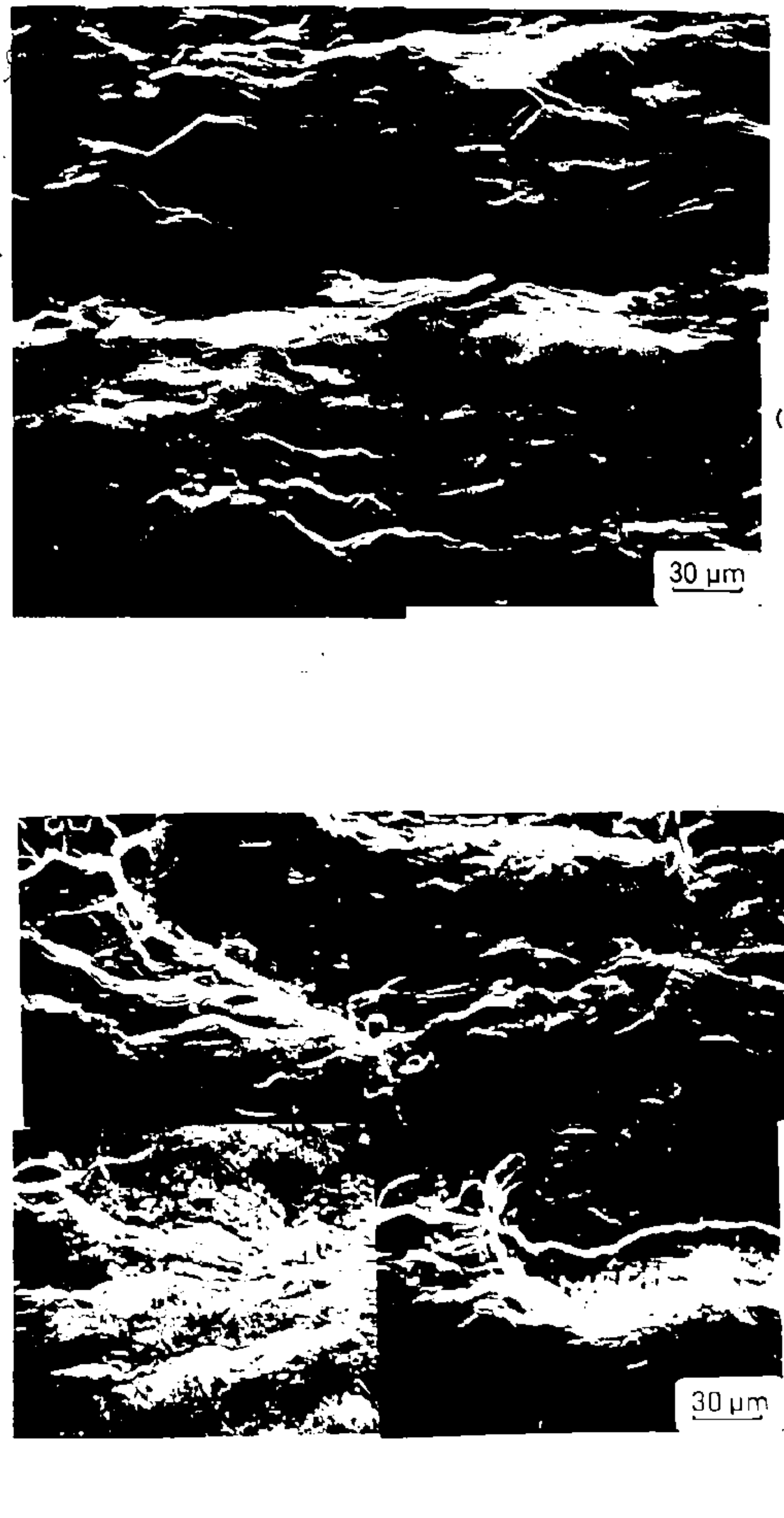

Figure 4-13 Surface deformation which has developed on polished specimens after bending to the same strain.
(a) material G.
(b) material P.

ials G and P after bending to approximately the same (high) strain. Material G exhibits the characteristic parallel bands of coarse slip and shows incipient cracking in the regions of grain boundaries and constituent particles. Material P has already passed through the stage described above for G, and has reached the point where local fracture events have occurred within the parallel deformation bands. However, the main aspect to note is the fact that many of these local fracture events are linked by transverse cracks (between bands) which largely follow grain boundary regions. Further deformation of material G confirmed that local surface cracks do form in this material also, but there is little evidence for link-up between the cracks. Hence, it is suggested that the critical event for the localisation of deformation into a major surface crack involves the linking of parallel deformation bands due to weaknesses in the grain boundaries. Such weaknesses could be the result of grain boundary precipitation.

Before concluding this chapter, two further observations regarding strain localisation will be noted without discussion because time constraints precluded any investigation of these. The first concerns the development of a localised neck in uniaxial tension and is illustrated by Figure 4-14. Specimen (a) has been pulled in tension continuously up to this point of necking, but specimen (b) was unloaded at maximum load and then re-loaded at a lower strain rate to induce serrations in the plastic flow. The serrations appear on the specimen surface as a type of Luder's band, each band corresponding to a single serration in the load-elongation curve. These bands may be oriented in either direction at approximately 55° to the tensile axis. The development of the

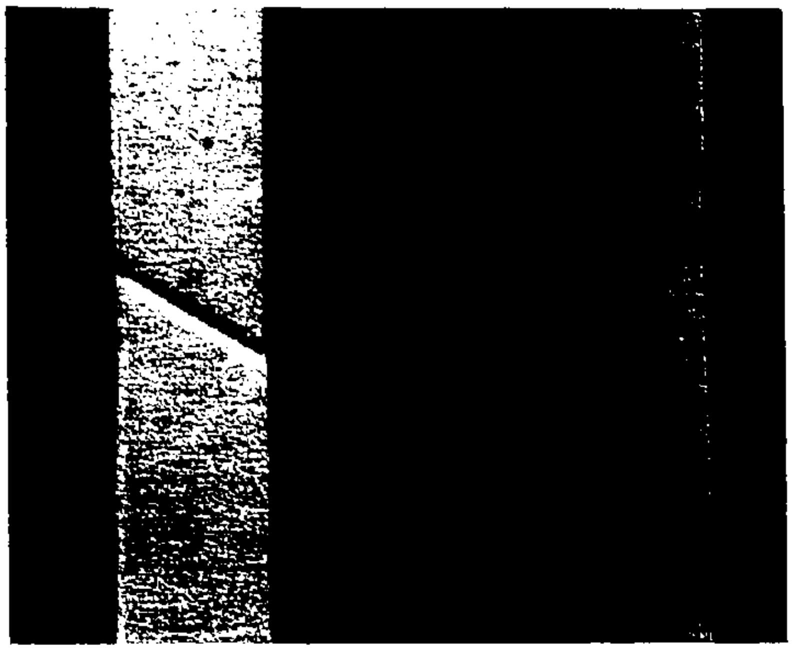

(a) (b)

Figure 4-14 Strain localisation in uniaxial tension. (a) test continuous up to necking; (b) specimen unloaded at maximum load and then re-loaded at lower strain rate.

localised neck was observed to occur by the localisation of the serration events into one particular band of material, with each further serration contributing to the severity of the localised neck and also its shear offset. A similar sequence of events (as registered on the load-elongation plot) occurred during fracture at normal strain rates, but there was no evidence for the Luder's band phenomenon.

The second observation concerns the local shearing events which constitute the final fracture of these materials in the plane strain and equi-biaxial tension deformation modes. Figure 4-15 indicates the interaction of unstable shear bands to produce the final fracture profile and shows that many of these may develop at approximately the same plastic strain. Furthermore, examination of the details of an incipient shear failure, (Figure 4-16), suggests that grain boundaries tend to influence the local path of the macroscopic shear failure, as do particles within the matrix (French and Weinrich, 1979).

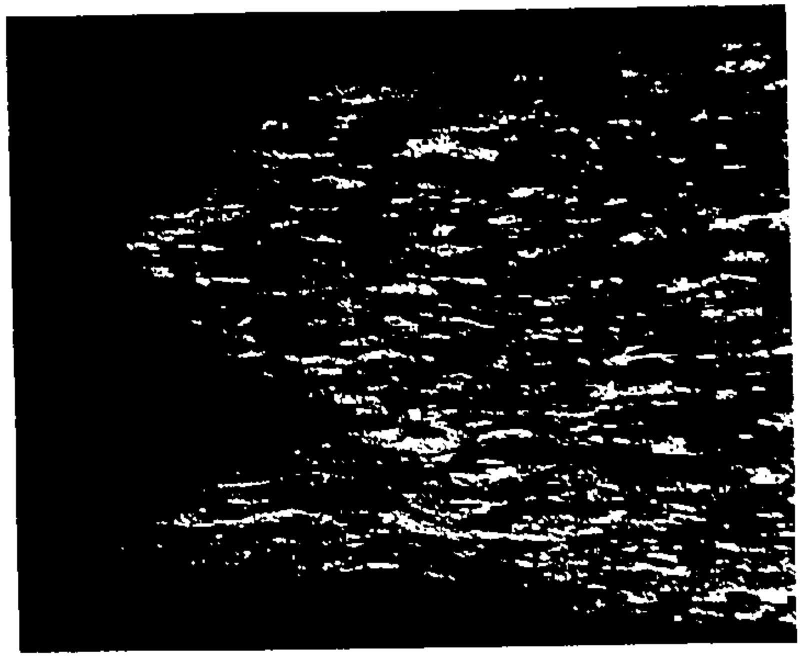

Figure 4-15 Interaction of shear bands to result in final fracture. Other incipient shear bands are shown by the arrows.

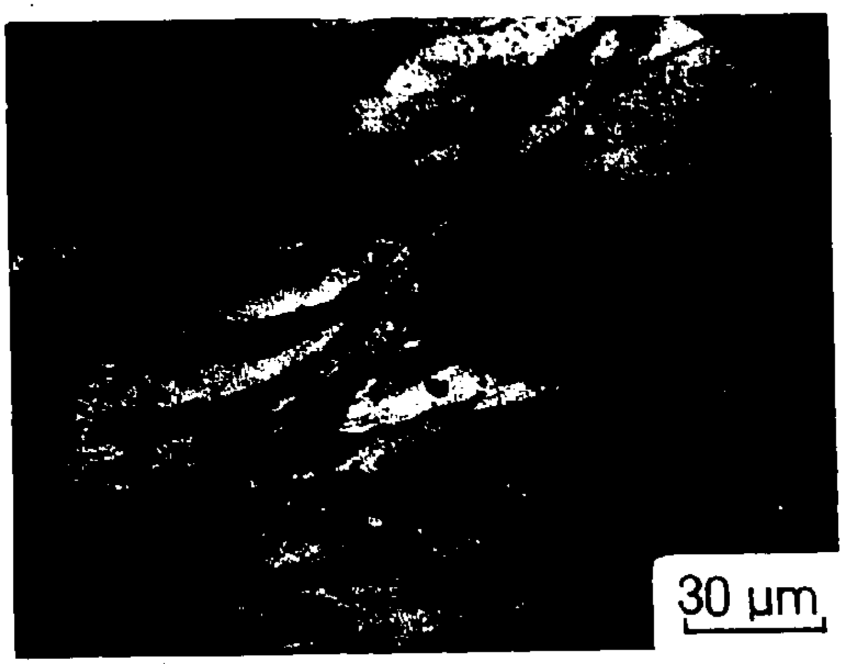

Figure 4-16 Details of shear failure in relation to grain structure.

CHAPTER 5

High Strain Deformation

From information regarding the nature of the engineering problem and from indicators given by the uniaxial tensile parameters and formability studies, it is obvious that significant differences exist between the materials in the strain regime approaching fracture. It was pointed out in Chapter 2 that material behaviour at large strains may be influenced by a variety of parameters, including the work hardening rate $(\frac{d\sigma}{d\varepsilon})$, the strain rate sensitivity $(\frac{d\sigma}{d\dot{\varepsilon}})$, and the rate of change of the hardening rate with strain $(\frac{\partial\theta}{\partial\varepsilon})$ and strain rate $(\frac{\partial\theta}{\partial\dot{\varepsilon}})$. Some of the possible influences of microstructural features on these parameters were also discussed in Chapter 2. The objective of the present chapter is to investigate the deformation of the 2036-T4 materials at high strains and indicate, where possible, the effects of the various microstructural features on the mechanical behaviour. This will involve average properties of the materials as distinct from the local variables known to influence the formability of these materials through their effects on fracture as discussed in Chapter 4.

5.1 Bulge Testing of 2036-T4: Experiment and Results

Utilisation of the hydraulic bulge test allowed the available range of strains to be increased beyond that attainable in uniaxial tension and so facilitated the study of the work hardening characteristics at large strains of the different batches of 2036-T4. Details on the bulge testing apparatus have been presented previously (Duncan et al, 1976) and it will be noted only that a 6-inch diameter circular die was used to produce equi-biaxial deformation in the region of the pole.

Additional points concerning the errors and assumptions will be made in the subsequent discussion section with reference to the present problem. A general review of the relationships involved in obtaining data from the bulge test is found in Appendix I, together with the basic test procedure.

Tests were performed with the extensometer placed parallel, perpendicular, and at 45° to the rolling direction of the sheet to elucidate any anisotropy of deformation within the plane of the sheet. The direction of fracture was also noted in relation to the prior rolling direction, as this is important in interpreting results of fracture strain measurements (see Chapter 4). It must also be noted that the final strain reading taken during the manual testing procedure does not indicate the fracture strain since small changes in pressure following this reading can produce significant changes in local strain. In the majority of tests, the materials fractured with the pressure remaining constant ~~or~~ decreasing very slightly from its maximum value.

Equivalent stress - equivalent strain curves presented in this chapter were generated by drawing a curve of best fit through the data points of at least two bulge tests for each case. Figure 5-1 indicates the typical scatter of these data for two tests with the extensometer oriented in the same direction. The determination of the work hardening rates was accomplished by estimation of the tangent to the average $\bar{\sigma}$-$\bar{\varepsilon}$ curve at various points along the curve. This was done on curves

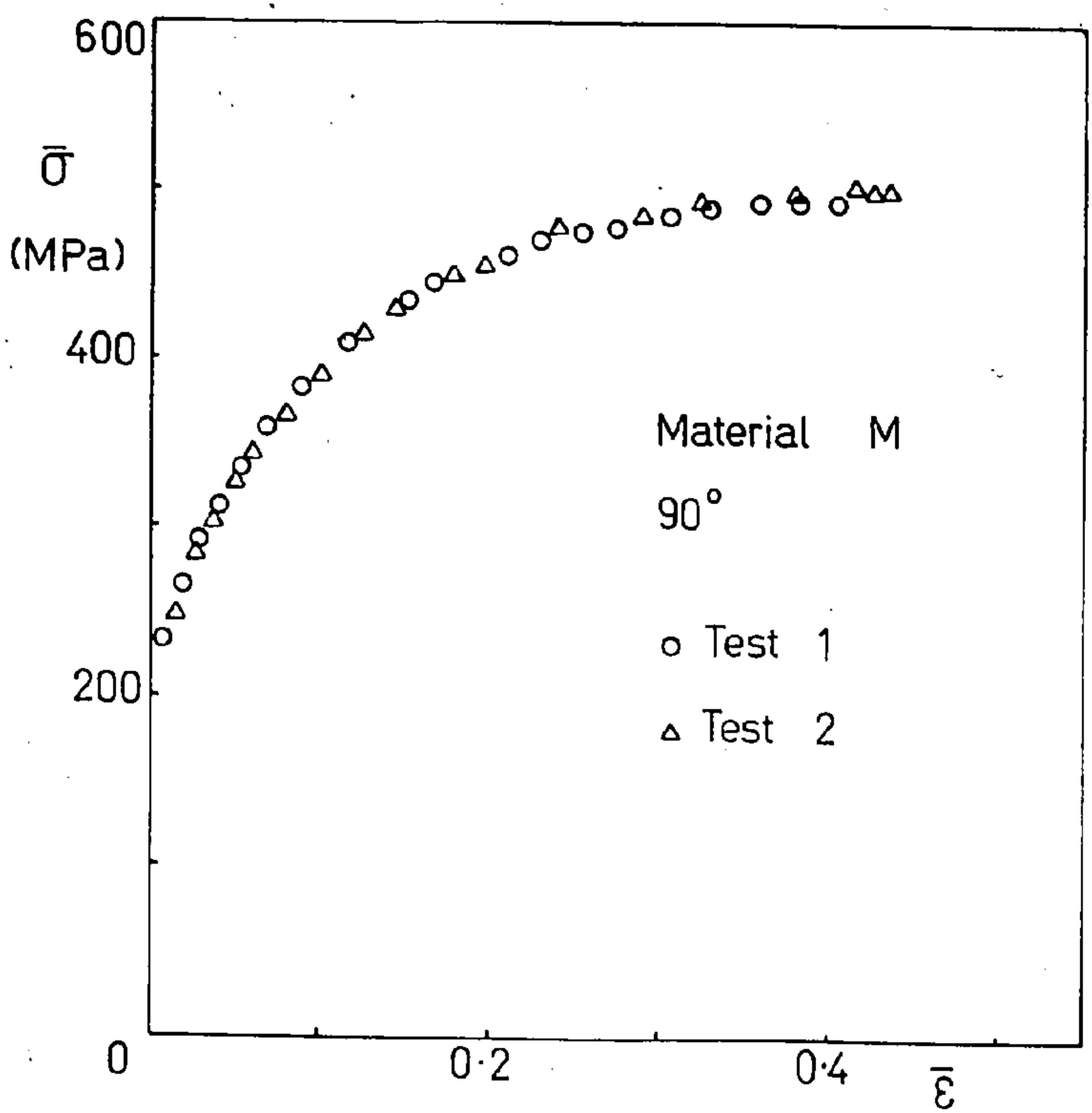

Figure 5-1 Diagram showing scatter of data points used to determine bulge test $\bar{\sigma}$-$\bar{\epsilon}$ curves. (Extensometer placed perpendicular (90°) to rolling direction.

of roughly twice the scale shown in this thesis to obtain greater accuracy.

Bulge testing of each lot of 2036-T4 showed that the $\bar{\sigma}$-$\bar{\varepsilon}$ curves developed depended upon the direction of placement of the extensometer, hereinafter referred to as the test direction. Curves for material M in the three directions are shown in Figure 5-2. Also included for comparison are uniaxial tensile curves for the longitudinal (0°) and transverse (90°) testing directions. The bulge test curves have not been adjusted to account for anisotropy using the Hill analysis (Hill, 1950). The tendency to divergence of the curves at large strains was observed to varying extents in all materials, and although the 45° test curves lay between those for 0° and 90° tests, they did not necessarily bisect the other curves. However, it is the divergence of the curves which is significant for this suggests that anisotropic deformation occurs at large strains. Figure 5-3 illustrates the effect of this divergence on typical plots of the work hardening rate as a function of imposed strain.

Figure 5-4 compares the $\bar{\sigma}$-$\bar{\varepsilon}$ curves for the different 2036-T4 materials taken from two test directions. Material M shows the highest strength level, while materials G and P have lower but similar strength levels. Average values of the final strain readings (prior to fracture) are shown in Table 5-1, and it is obvious that there is a major difference between strains in the 0° and 90° test directions. A crude measure of the formability of the materials in equi-biaxial tension, the bulge height, is given for each material in Table 5-2.

Comparison of the work hardening behaviour of the three materials during bulge testing was made on the basis of plots of the work

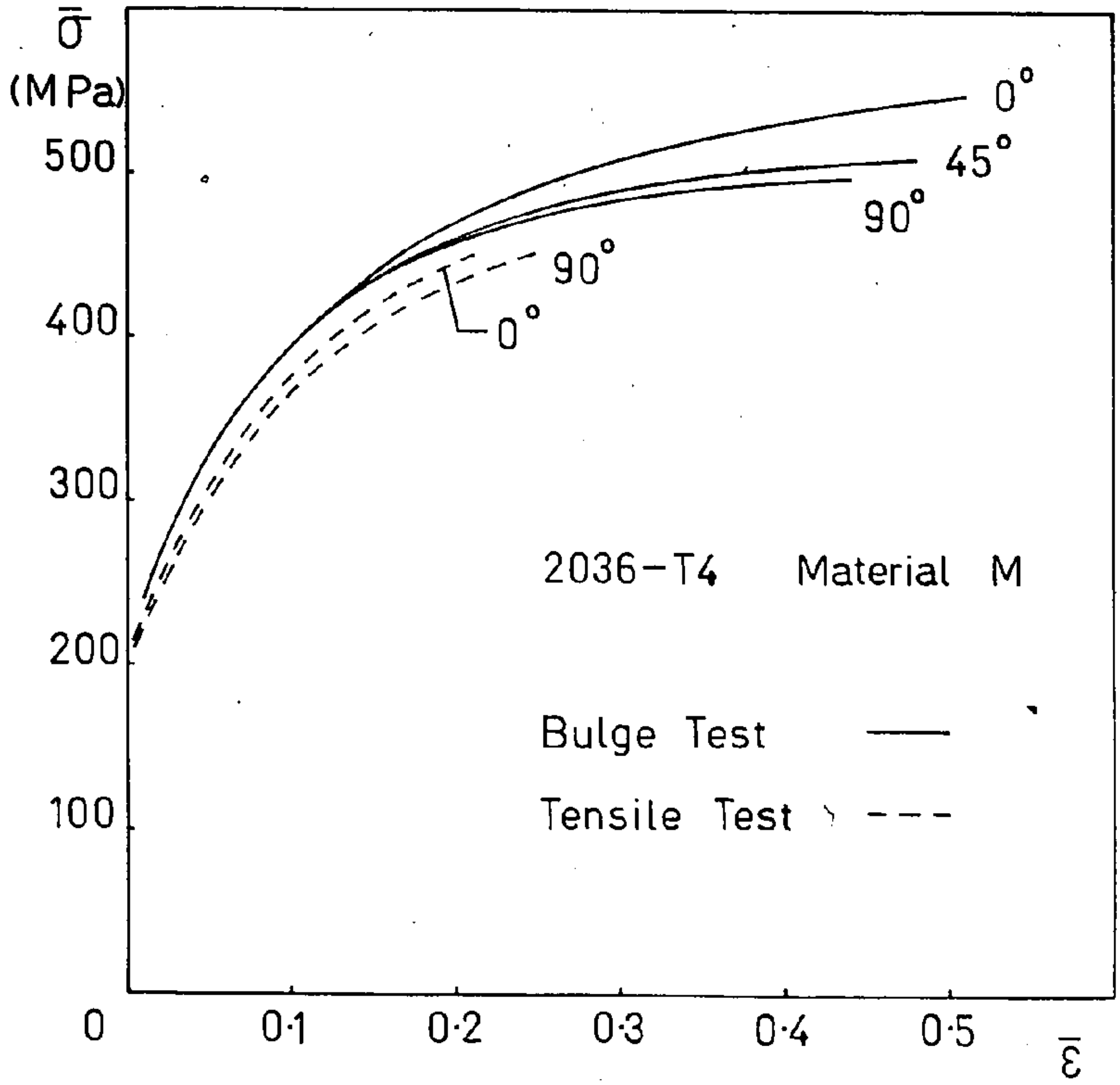

Figure 5-2 $\bar{\sigma}$-$\bar{\varepsilon}$ curves in tension and bulge testing which indicate the dependence on test direction.

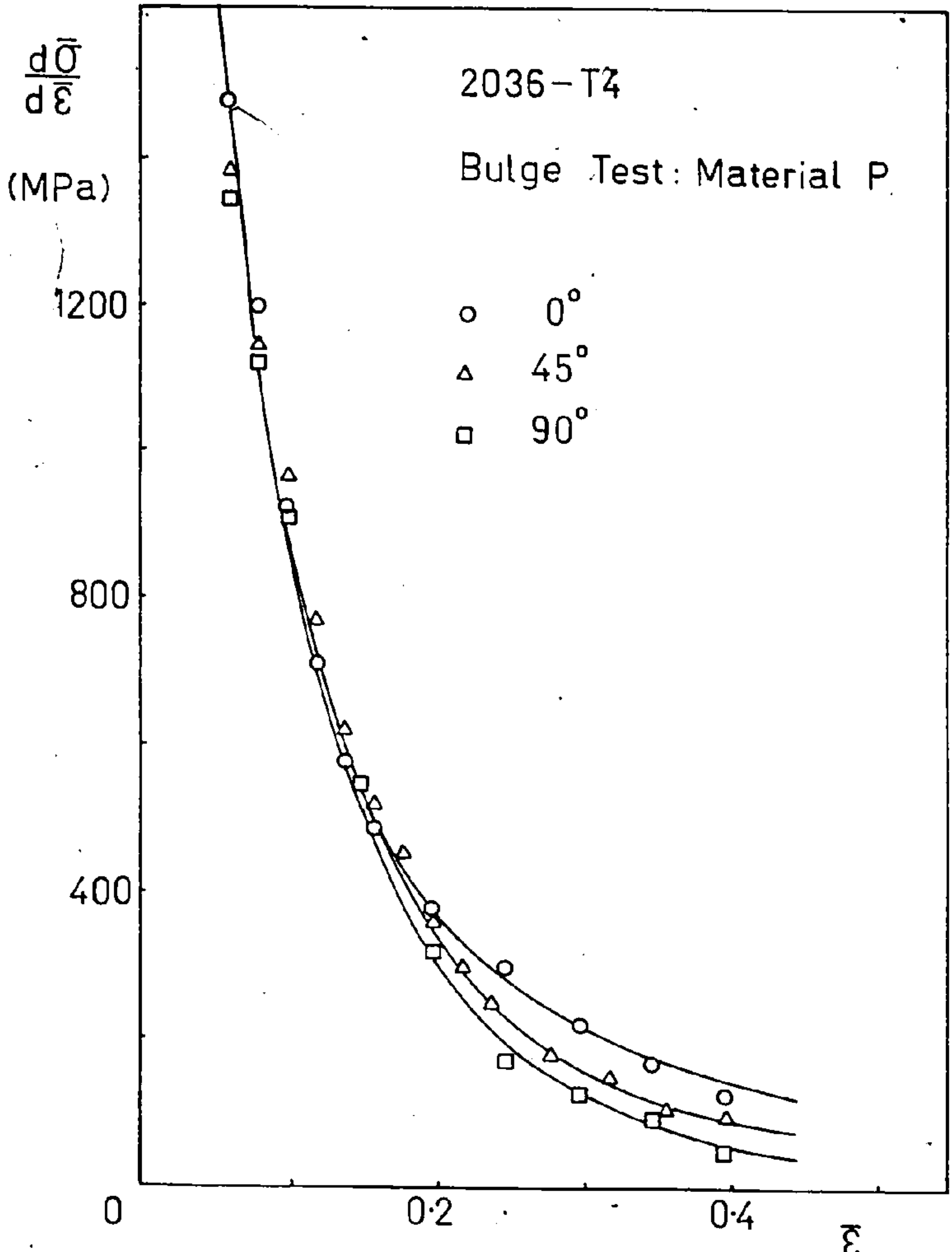

Figure 5-3 Work hardening rate vs strain curves for bulge tests in three directions of extensometer placement.

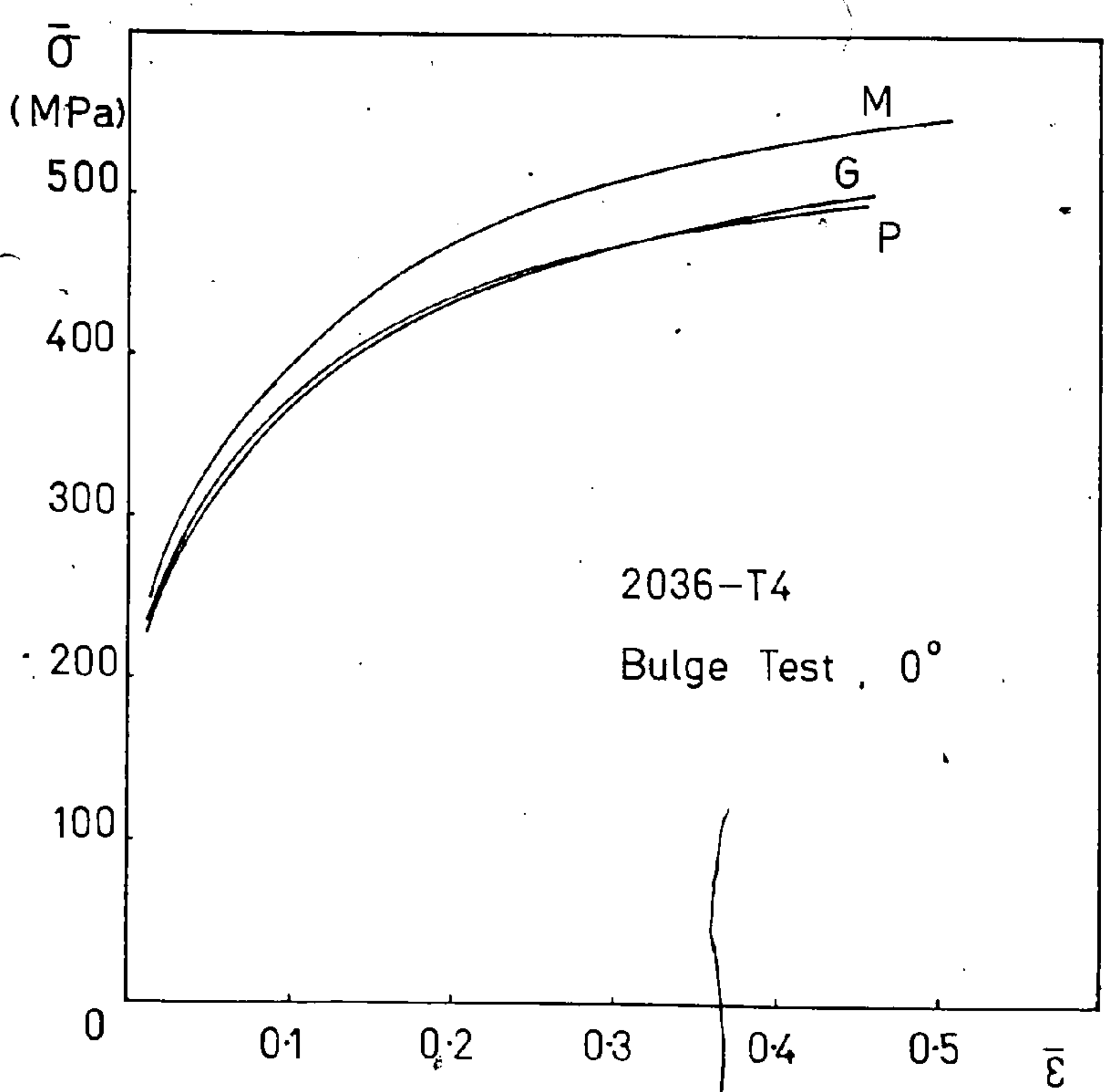

Figure 5-4(a) Comparison of 0° bulge test $\bar{\sigma}$-$\bar{\varepsilon}$ curves for three 2036-T4 materials.

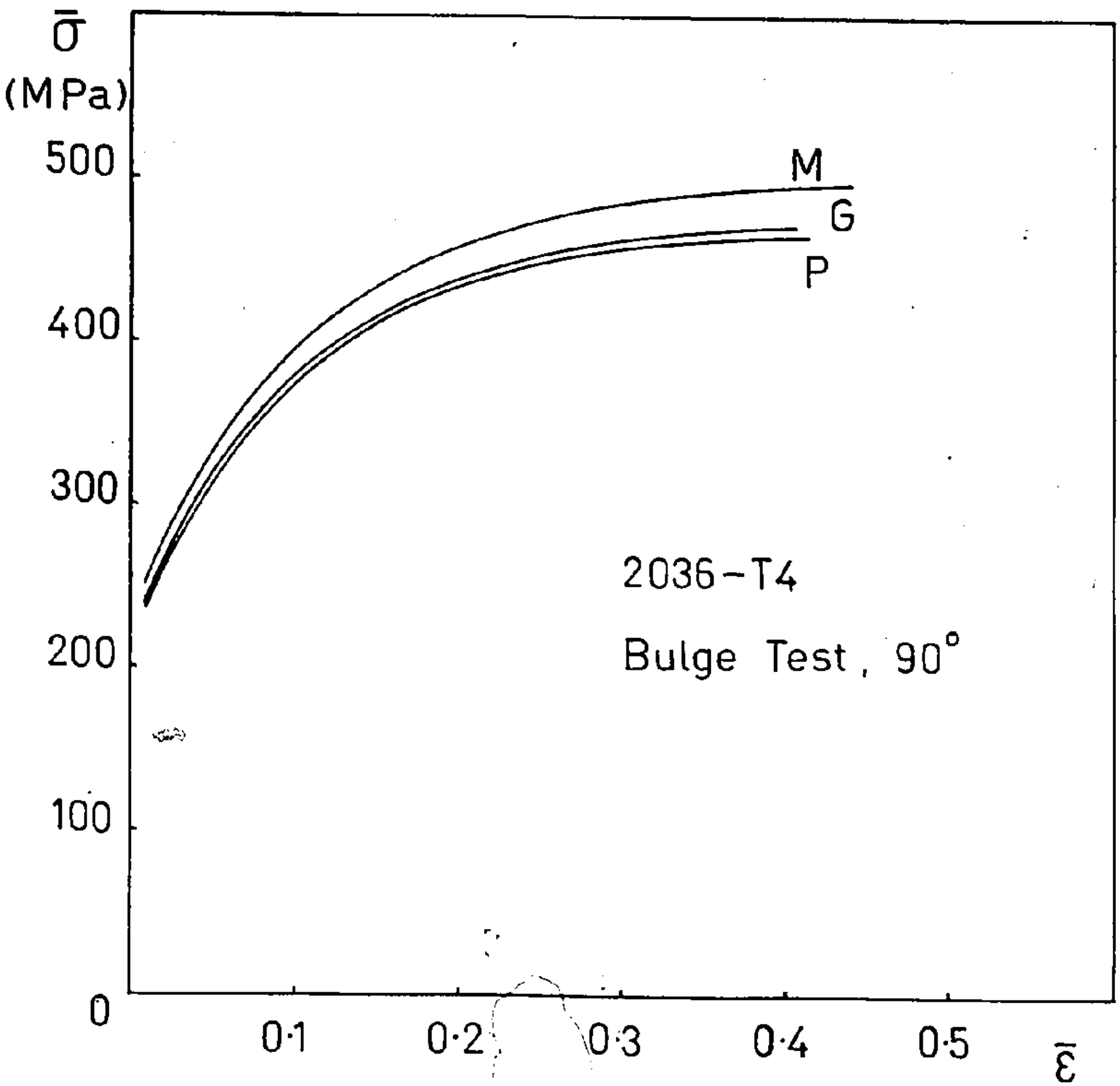

Figure 5-4(b) Comparison of 90° bulge test curves for three 2036-T4 materials.

Table 5-1

Final Strain Readings
-Hydraulic Bulge Test

MATERIAL	FINAL $\bar{\epsilon}$		
	0°	45°	90°
G	.447	.436	.395
M	.488	.457	.403
P	.457	.405	.402

Table 5-2

Material	Average Bulge Height (mm)	Range of Heights (mm)
G	45.7	44.9 - 46.4
M	48.3	46.5 - 50.95
P	45.8	44.6 - 46.9

hardening rate $(\frac{d\bar{\sigma}}{d\bar{\varepsilon}})$, and the work hardening rate normalised by the flow stress $(\frac{1}{\bar{\sigma}} \cdot \frac{d\bar{\sigma}}{d\bar{\varepsilon}})$ as a function of imposed strain $(\bar{\varepsilon})$. The normalised work hardening rate was chosen to remove the effect of the higher flow stress of material M on the value of its work hardening rate at a given strain. Comparison of the work hardening rates for each material in each of the three test directions showed that they followed the same trends, but for reasons to be given in the discussion, only the data for tests in the 45° direction will be presented. Figure 5-5 shows graphs of the $\frac{d\bar{\sigma}}{d\bar{\varepsilon}}$ and $\frac{1}{\bar{\sigma}} \frac{d\bar{\sigma}}{d\bar{\varepsilon}}$ as functions of $\bar{\varepsilon}$ for each material in the 45° direction. Figures 5-5(a) and (b) indicate the similarity of data from the different materials, and Figure 5-5(c) shows the high strain portion of Figure 5-5(b) using a smaller ordinate scale.

5.2 Discussion of Large Strain Deformation

5.2.1 The Bulge Test

The low strain regime of the hydraulic bulge test $\bar{\sigma}$-$\bar{\varepsilon}$ curve is considered to be inaccurate because of difficulties in recording the correct strain and curvature readings under conditions where elastic flexing of the sheet and non-symmetric deformation are known to occur. Wycliffe (1977) has discussed the errors in the values of $\bar{\sigma}$, $\bar{\varepsilon}$ and $\frac{d\bar{\sigma}}{d\bar{\varepsilon}}$ resulting from the gauge readings, and has shown that the error in the calculated value of $\bar{\sigma}$ can be large at the beginning of the test. This error, combined with that associated with determining the strain, can result in large differences in the work hardening rates at low levels of strain. At strains approaching fracture, the scale reading error associated with the high pressure gauge is relatively large, and

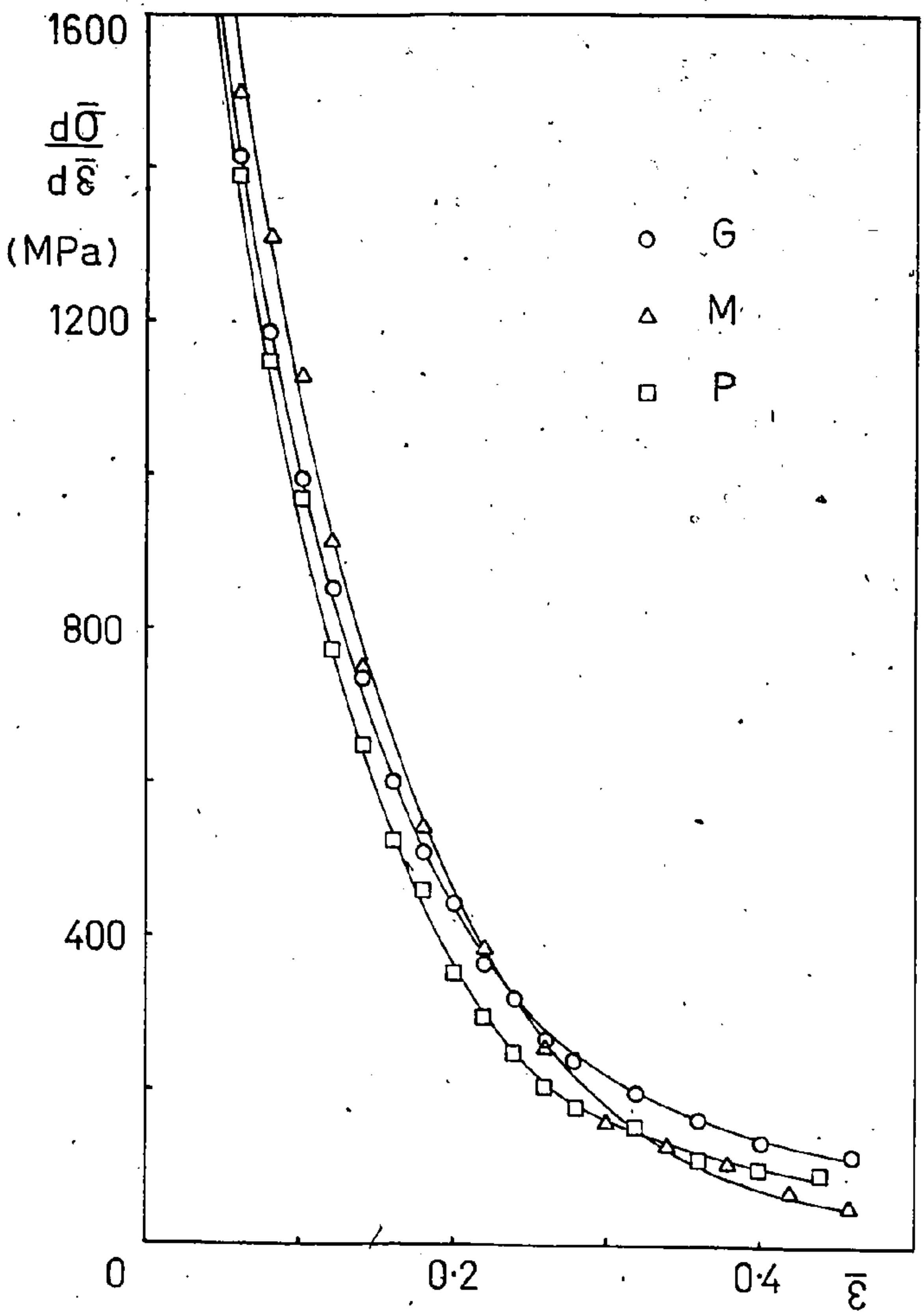

Figure 5-5(a) Work hardening rate vs strain for three 2036-T4 materials; 45° bulge tests.

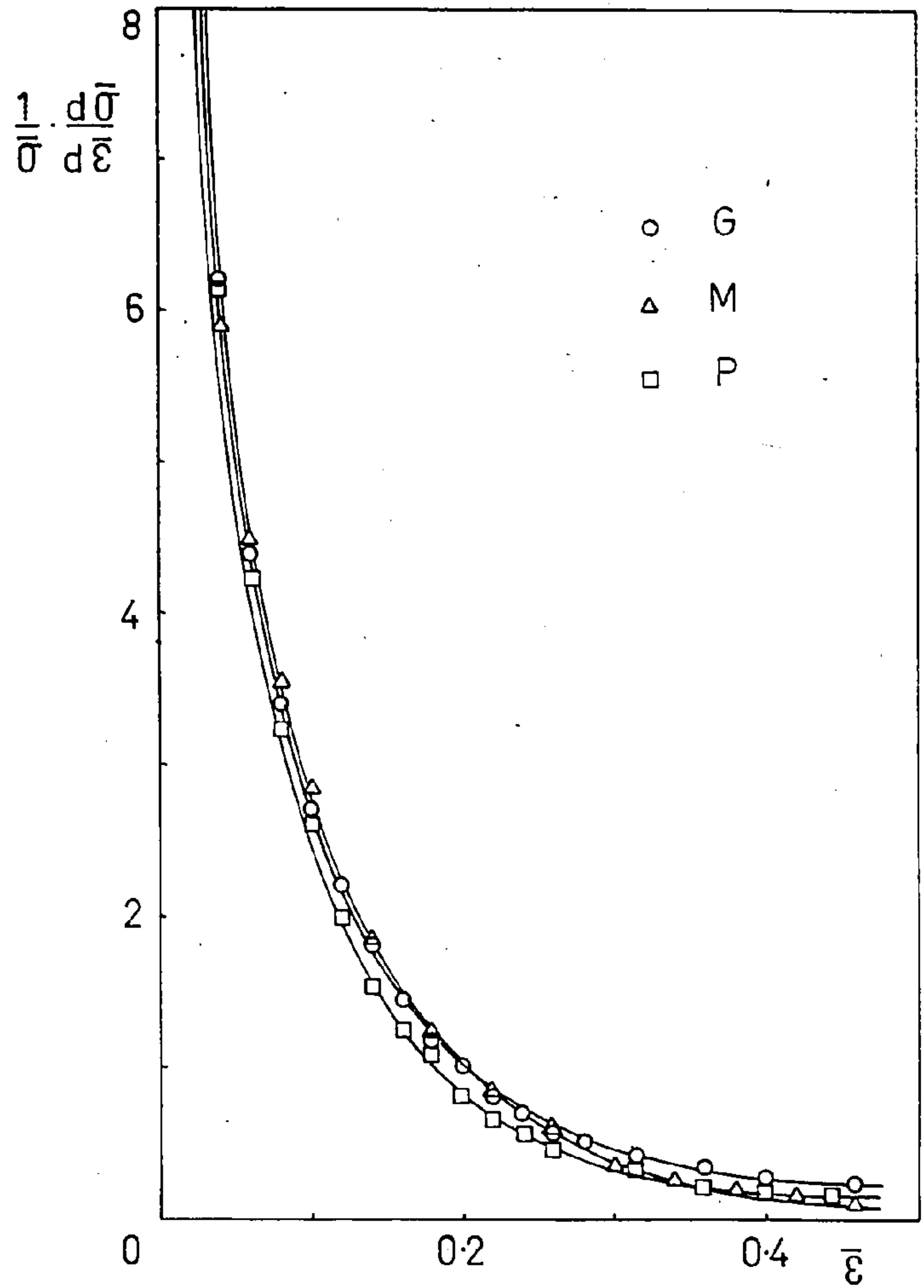

Figure 5-5(b) Normalised work hardening rate vs strain.

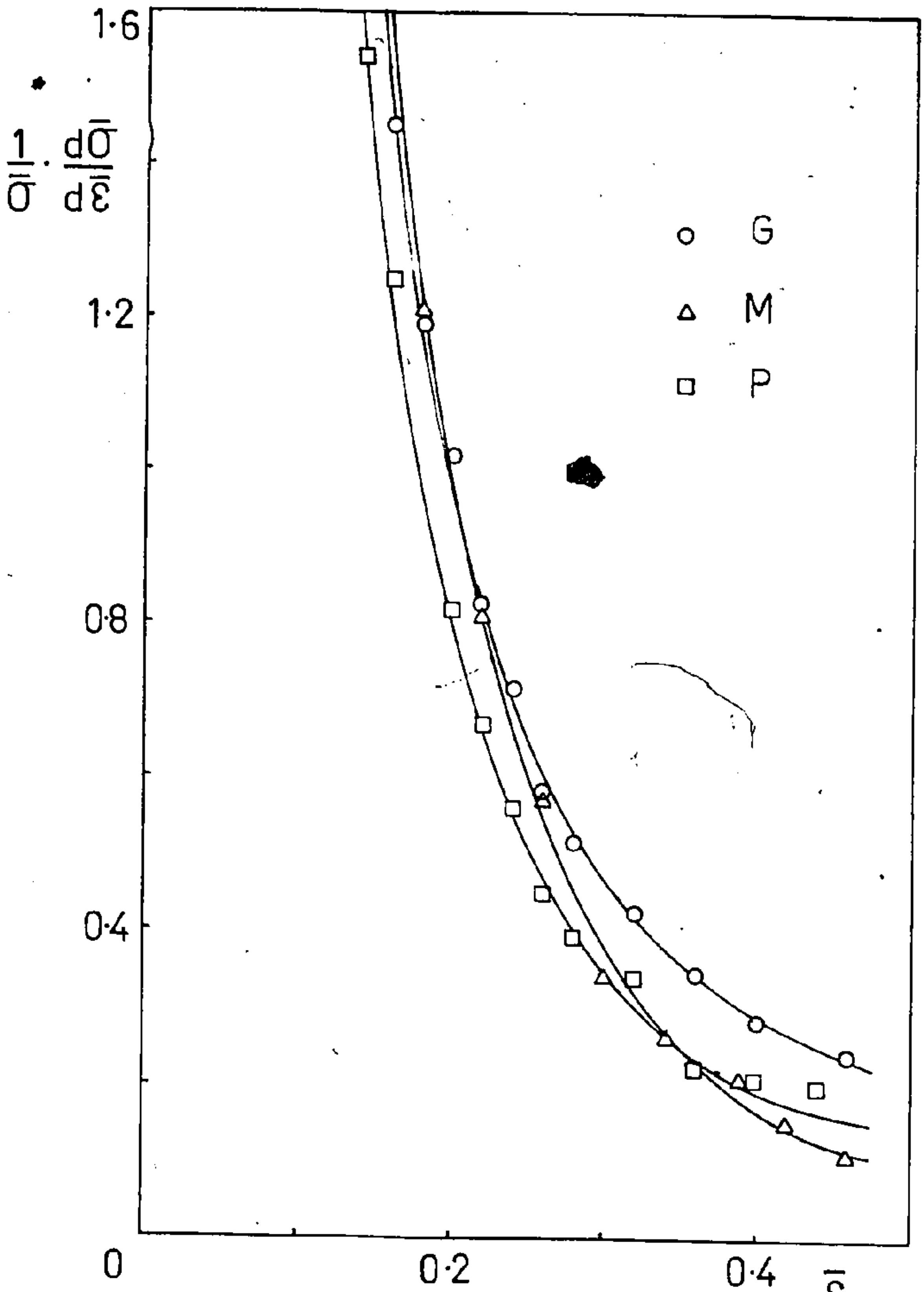

Figure 5-5(c) Normalised work hardening rate vs strain; details of high strain region.

this introduces uncertainty into the data since small increases in the pressure reading correspond to quite large increases in the strain reading. This uncertainty is compounded in the calculation of the stress $\bar{\sigma}$ as both the pressure and strain variables appear in the formula (see Appendix I); the latter arises via the assumptions made regarding the current thickness. For example, scale reading errors of half a division in each extensometer and spherometer dial gauge (i.e., ±.005 in.), and an error of ±15 lbs in the high pressure gauge, result in an error in the calculated value of $\bar{\sigma}$ of approximately ±3% or 15 MPa at the fracture stress. This is roughly half the value of the divergence of the curves at large strains, but a consistent approach to multiple testing would reduce the uncertainty of each test and increase the accuracy of comparison of different materials and different test directions.

An unfortunate consequence of the manual bulge testing procedure is the lack of control of the deformation rate. Also, during the time involved in reading the spherometer and extensometer gauges, some stress relaxation occurs which affects the deformation upon re-application of the pressure. However, if the pressure is noted at the instant of stopping, there will be no reading error introduced as a result of the relaxation. Comparison with other data on the same materials determined by continuous testing (A.D.D.R.G. Aluminum Cooperative Group, 1979) shows that the differences are quite small, and thus, it is assumed that the manual testing technique does not influence the conclusions concerning comparison of materials.

Figure 5-2 indicates the increase in strain attainable by the bulge test over the uniaxial tensile test. The divergence of the bulge test curves is an important consequence of the anisotropic nature of the deformation of these materials, and has been observed by the author to occur also in other aluminum alloys, such as 6010-T4 and 5182-0. In all cases, the imposed strain is greatest in the longitudinal direction, whether it is measured directly from the bulge test extensometer or from the analysis of the deformed grid circles. The grid circle analysis performed on samples strained to different levels indicates that the anisotropy of strains develops late in the test.

It is suggested that this effect cannot be predicted from parameters such as the normal plastic anisotropy (r) determined in uniaxial tension, since the effect develops only after considerable deformation and is not noticeable at the lower strains (where r-value measurements are made). Previous workers (Duncan et al, 1976) have already shown that the biaxial $\bar{\sigma}$-$\bar{\varepsilon}$ curves for many aluminum alloys are not predicted from uniaxial data via the Hill (1950) analysis. Herø and Naess (1978) have further suggested that differences in $\bar{\sigma}$-$\bar{\varepsilon}$ curves between uniaxial and biaxial tension may indicate either that the concept of isotropic work hardening is not correct or that the shape of the yield locus is different from the theoretical prediction. It has also been suggested (Embury,1979b) that the accumulation of damage may depend on both the strain path and the distribution of intermetallics in the material.

Because of the divergence of the $\bar{\sigma}$-$\bar{\varepsilon}$ curves, there is a difficulty in establishing a deformation curve which is characteristic of the material under the conditions of balanced biaxial loading. The discrepancy in strains parallel and perpendicular to the rolling direction indicates that the spherical shell assumption may be invalid at large strains and hence, the computation of the equivalent stress will be in error. A possible source of this error is outlined in the following argument.

The equivalent stress - equivalent strain curve determined for equi-biaxial deformation can be considered as a curve representing the through-thickness uniaxial stress-strain relationship for the material. This only requires the assumption that hydrostatic stress does not alter yielding in an anisotropic material. It is further assumed that the stress is equi-biaxial, or at least that

$$p = t\left(\frac{\sigma_1}{R_1} + \frac{\sigma_2}{R_2}\right)$$

where $R_1 = R_2$, as mentioned previously. Schematically, then;

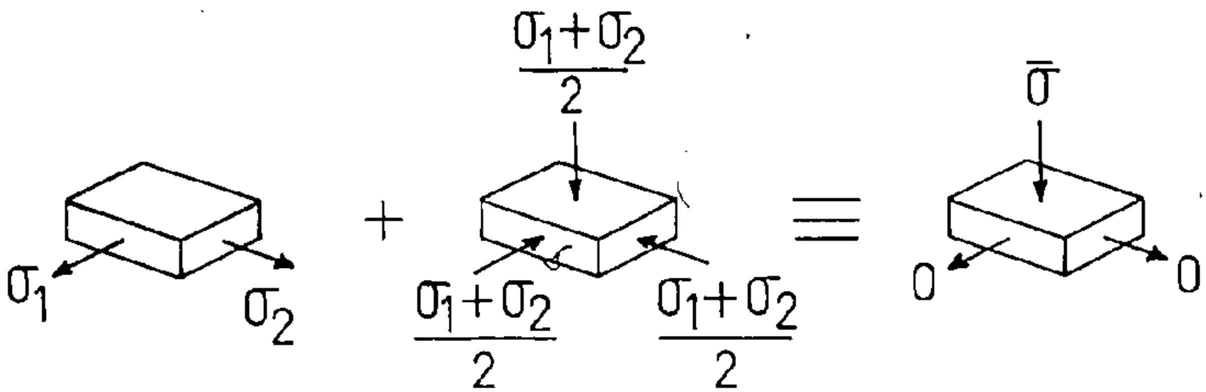

However, if strain measurements are made in both the rolling and transverse directions within the sheet plane, then, for the purposes of determination of the stress-strain relationship;

$$\varepsilon_t = -(\varepsilon_0 + \varepsilon_{90}) \ ,$$

implying that if $\varepsilon_0 \neq \varepsilon_{90}$, and one writes $\varepsilon_t = -2\varepsilon_0$ or $\varepsilon_t = -2\varepsilon_{90}$, then there will be an error in ε_t, and hence, an error in the (calculated) value of the current thickness. In the present case, $\varepsilon_0 > \varepsilon_{90}$, thus, the calculated value of the stress $\bar{\sigma}$ will be an overestimate of the actual value when the extensometer is placed along the rolling direction of the sheet, and an underestimate for the transverse orientation. This is observed in the experimental curves of Figure 5-2.

If the orientation of the material element is

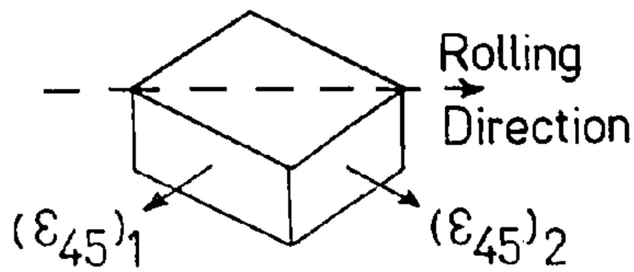

then it is likely that $(\varepsilon_{45})_1 = (\varepsilon_{45})_2$ and hence,

$$\varepsilon_t = -2(\varepsilon_{45})_1 = -2(\varepsilon_{45})_2.$$

Thus, one would expect that data obtained from the 45° placement of the extensometer gives some average representation of the material behaviour and are subject to the least error. The divergence of the 0° and 90° curves will indicate the presence of any anisotropy but will be subject to larger errors.

Differences between longitudinal and transverse strains in sheet deformed by bulge testing is an important observation, but appear to be typical for aluminum alloys (Duncan, 1979). It was further noted during the present study that the extent to which the longitudinal strain exceeded the transverse strain depended upon the position on the bulge at which the strains were measured. This is illustrated in Figure 5-6 which shows the results of strain measurements on grid circles during traverses across the pole of the bulge in two orthogonal directions,

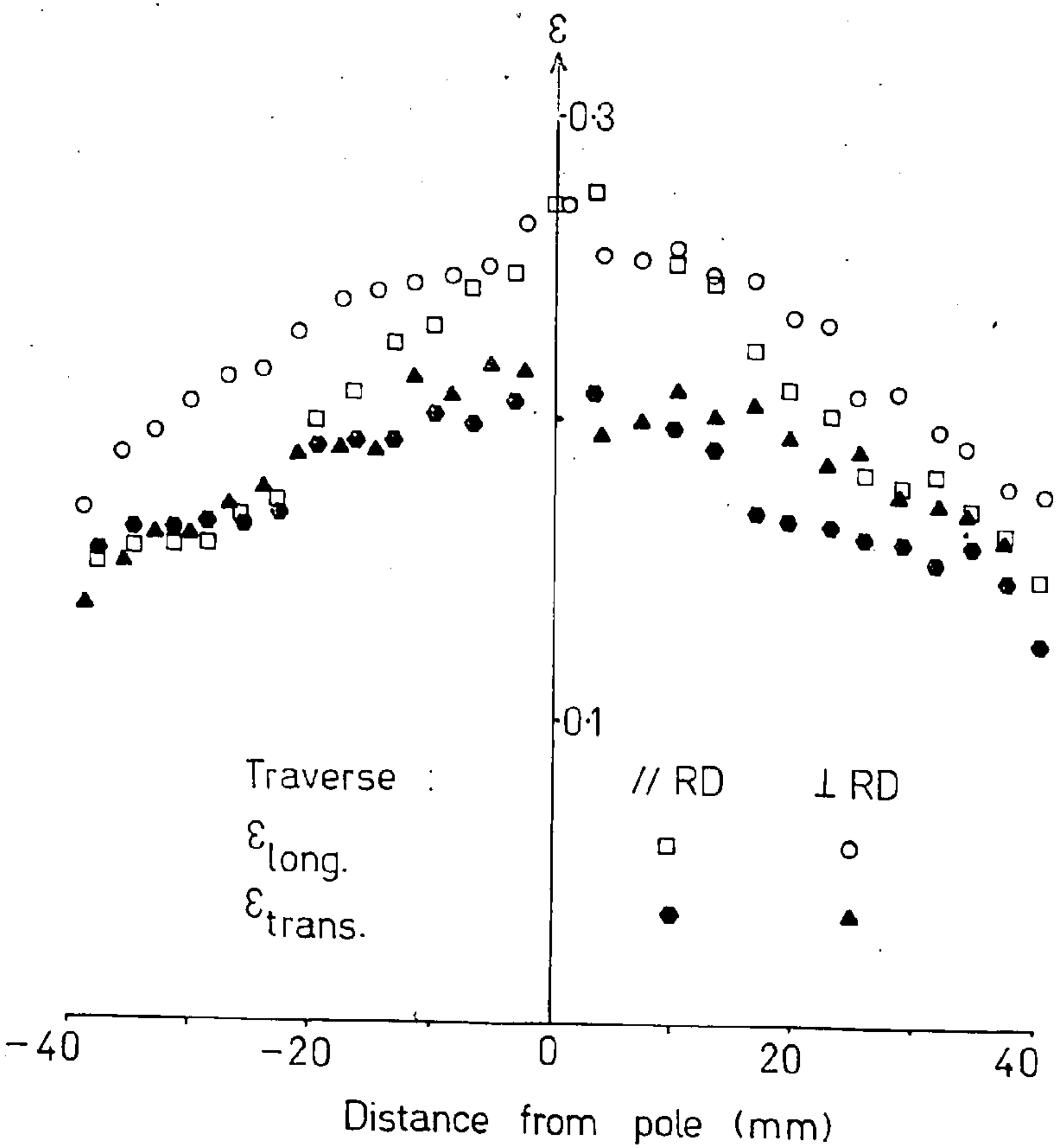

Figure 5-6 Variation in surface strains across the pole of the bulge; 2036-T4 material G.

i.e., parallel (||) and perpendicular (⊥) to the rolling direction. It is seen that the levels of transverse strains are similar in both traverses, but the level of the longitudinal strains is highest for the traverse perpendicular to the rolling direction. This trend was observed in all three materials, and its existence supports the premise that the assumptions used to generate the $\bar{\sigma}$-$\bar{\varepsilon}$ curve are questionable.

5.2.2 Work Hardening

The primary purpose of the hydraulic bulge test was to provide information concerning the work hardening characteristics of the materials at large strains. Referring to Figure 5-5, it is seen that:

a) the differences between the work hardening rates of the three materials are generally small (Figure 5-5(a)), and are comparable to the differences exhibited by one material tested with the extensometer parallel and perpendicular to the rolling direction (Figure 5-3),

b) the level of work hardening of material P is lowest over most of the strain range (for either parameter of work hardening),

c) materials G and M show similar levels of normalised work hardening up to strains of about 0.3 after which material M decreases rapidly (Figure 5-5(c)), and

d) material G maintains the highest hardening rate at large strains.

The level of work hardening of material P is consistent with its inferior uniaxial tensile properties and also its press performance.

The differences between work hardening characteristics of materials G and M are more difficult to interpret. On the basis of the normalised work hardening rate, these materials should exhibit similar behaviour in bulge deformation, but the bulge height data contained in Table 5-2 indicate that material M is superior. This is in agreement with the trends provided by plots of the work hardening rate ($\frac{d\bar{\sigma}}{d\bar{\varepsilon}}$) vs strain such as shown in Figure 5-5(a), where the data for material M lies above the other data up to strains of approximately 0.3. It therefore appears that a description of the work hardening behaviour of a material without cognisance of the strength level may be misleading in terms of its formability under certain conditions of loading.

The behaviour of material M, i.e., its uniaxial tensile properties (Table 3-1), and its ability to distribute strains during bulging as evidenced by the maximum bulge heights (Table 5-2), final strain readings (Table 5-1) and work hardening characteristics (Figure 5-5), suggests that this material should perform well in the press; but this is not so. Either the complex loading trajectory during production cannot be compared to either the uniaxial or equi-biaxial tensile deformation, or the controlling events occur after the localisation of flow begins. It is difficult to distinguish between these alternatives because of the different levels of uniform strain associated with the different loading trajectories. However, the rapid decrease in hardening rate of material M at high strains in the bulge test may be related to its marginal performance during production.

The work hardening rate at high strains is influenced by the accumulation of damage within the material and by the dynamic recovery processes which are occurring simultaneously with the strain events, as discussed in Chapter 2. leRoy (1978) has suggested that failure of 2036-T4 is governed by a maximum shear stress criterion wherein the localisation of strain is very acute and occurs with little accumulation of damage (eg., particle decohesion and voiding) prior to the final failure. The current study revealed very little evidence of severe void formation away from the immediate fracture site. Hence, it is suggested that the general decrease in work hardening at large strains is due largely to dynamic recovery, although the local work hardening behaviour of the three materials just prior to fracture will be influenced by subtle differences in their microstructure. This aspect was not investigated, but it is suggested that the rapid decrease in work hardening of material M may have its origins in these subtle differences. For example, Wycliffe (1977) has shown that small changes in the amount of Mn in solid solution in 3003-type alloys have a significant effect on the hardening rates at large strains, and Parker (1978) suggests that the amount of Mg in solid solution in 2036-T4 exerts an influence on strain hardening behaviour through its effect on the strain rate sensitivity (Mg being a very mobile solute). Further work is necessary to develop a better understanding of the effects of structure on work hardening.

It is evident that differences in the work hardening behaviour of the three materials are only marginal compared to the difference in the fracture characteristics as discussed in Chapter 4. Hence, it would be misleading to correlate the press performance only with the work hardening characteristics, for these apply to deformation in a volume of material far greater than the volume associated with the fracture event and thus do not represent the local behaviour of material at fracture.

CHAPTER 6

THE INFLUENCE OF AGEING ON MECHANICAL BEHAVIOUR

In this chapter, some results concerning the influence of the age-hardening process on the mechanical behaviour of alloy 2036 will be presented. The behaviour in uniaxial and equi-biaxial tension, the formability, and the fracture characteristics were investigated. The age-hardening process constitutes a simple method of achieving controlled variations in some of the structural features, and hence, this type of study is important in attempting to relate various aspects of mechanical behaviour to microstructure.

6.1 Microstructural Changes During Ageing of 2036

Material G was chosen as the basis for this portion of the study. Details of the solution heat treatment and ageing conditions are shown in Table 6-1. Note that the as-received T4 material was used as a basis for comparison, additional heat treatments being performed on this material to achieve the other ageing conditions. Figure 6-1 shows the effect of ageing time on the yield strength of 2036; data for the natural ageing agrees well with the results of Evancho and Kaufman (1977). The various tempers used in the present study are indicated on the graph. It was decided to artificially age the T4 materials because of the similarity of this treatment to the paint bake cycle performed on formed components in the automotive industry.

Changes in the microstructure with ageing condition were deter-

Table 6-1

Details of Thermal Treatments Performed on 2036

W	(as quenched)	solution treat at 500°C for 1 hour, followed by cold water quench and held at 0°C for 2 hours before testing
T4	(naturally aged)	as-received
T6	(peak aged)	aged at 190°C for 9 hours
T7	(overaged)	aged at 300°C for 20 hours

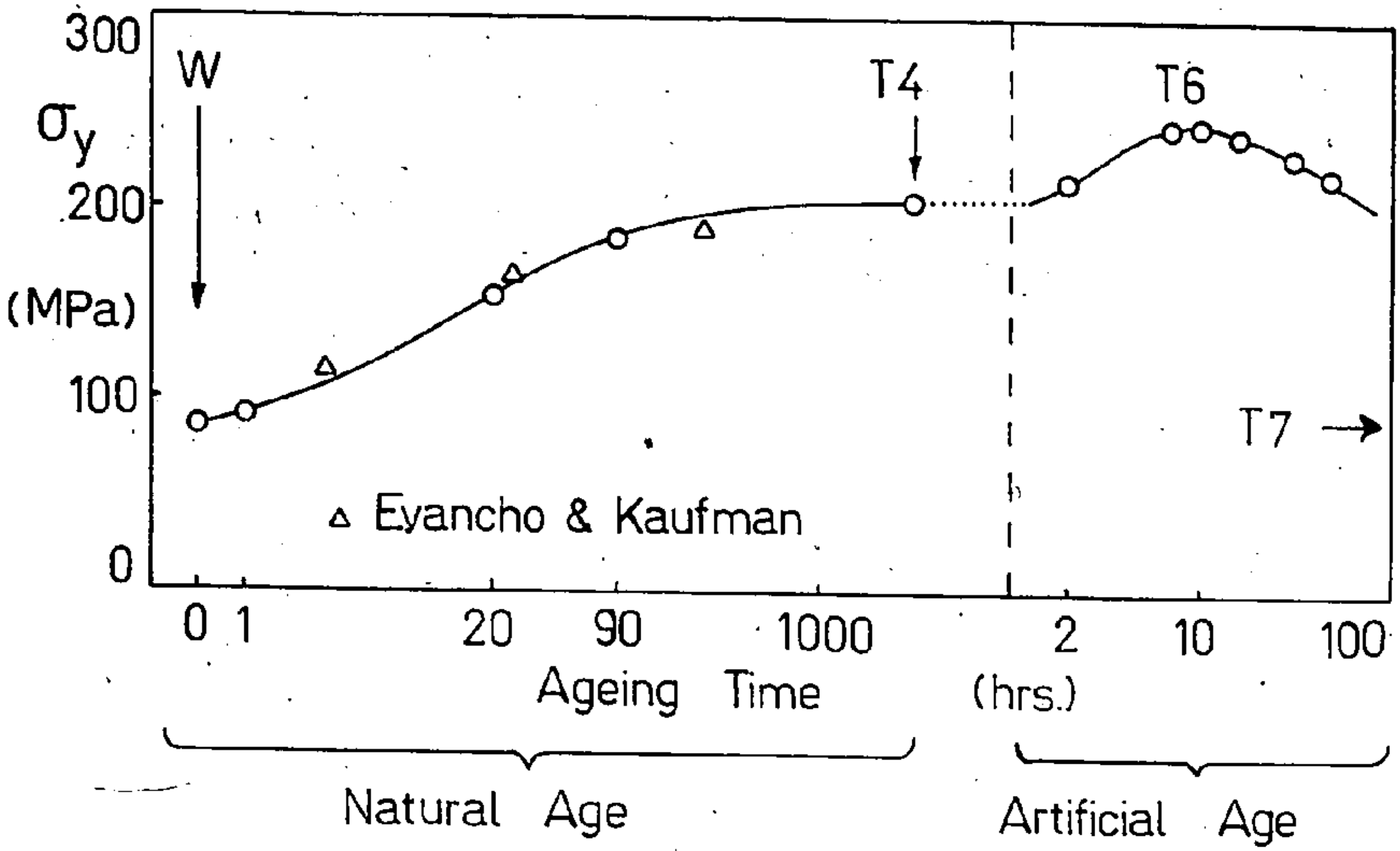

<u>Figure 6-1</u> Effect of ageing time on yield stress of 2036 alloy (composition of material G). Artificial ageing was performed on the T4 material.

mined by T.E.M. studies and are illustrated in Figure 6-2 for the T4, T6 and T7 conditions. No study of the W temper was performed. The T4 structure has been described in Chapter 3. Material in the T6 condition exhibits orthogonal platelets of precipitate consistent with θ' due to ageing at this temperature (Kelly and Nicholson, 1963). The orientation of the foil normal in this case is <100> with the platelets parallel to the foil surface invisible. There is also an increase in the amount of grain boundary precipitate compared to the T4 material, and evidence of a precipitate-free zone adjacent to the grain boundaries. The width of the precipitate-free zone is approximately 1000 Å, and is less than would be expected if the material had been artificially aged directly following the quench due to the precipitation of the zones in the T4 material.

Overageing (T7) has resulted in coarsening of the precipitates to maximum dimensions of 2000 - 3000 Å with interparticle spacings of 6000 Å. Although not shown in this micrograph, there was a significant increase in the amount of grain boundary precipitation. Figure 6-2(d) shows dislocation loops (surrounding the precipitates in the T7 condition). These result from the loss of coherency of the interface as the particle grows.

6.2 Effect of Ageing on Mechanical Behaviour

Uniaxial tensile tests and automated hydraulic bulge tests* were performed on the different tempers of material. Figure 6-3 shows the $\bar{\sigma}$-$\bar{\varepsilon}$ curves developed for longitudinal tensile and bulge tests, while

* Bulge tests performed at Alcoa Laboratories, Pa., U.S.A.

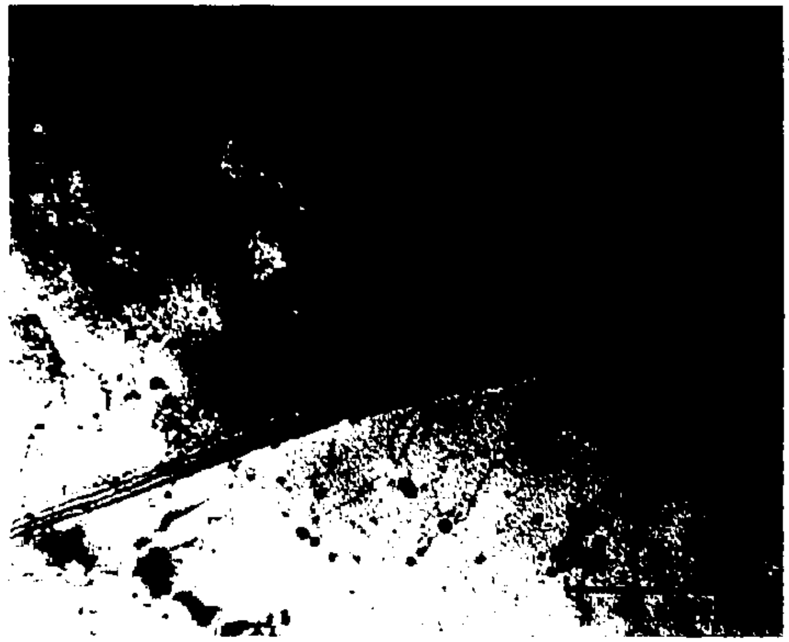

Figure 6-2(a) T.E.M. 2036-T4

Figure 6-2(b) T.E.M. 2036-T6

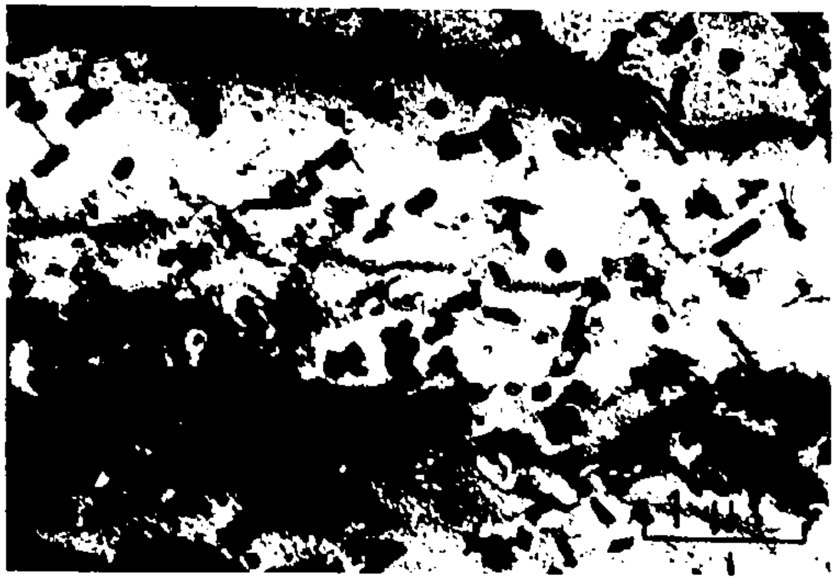

Figure 6-2(c) T.E.M. 2036-T7

Figure 6-2(d) T.E.M. 2036-T7

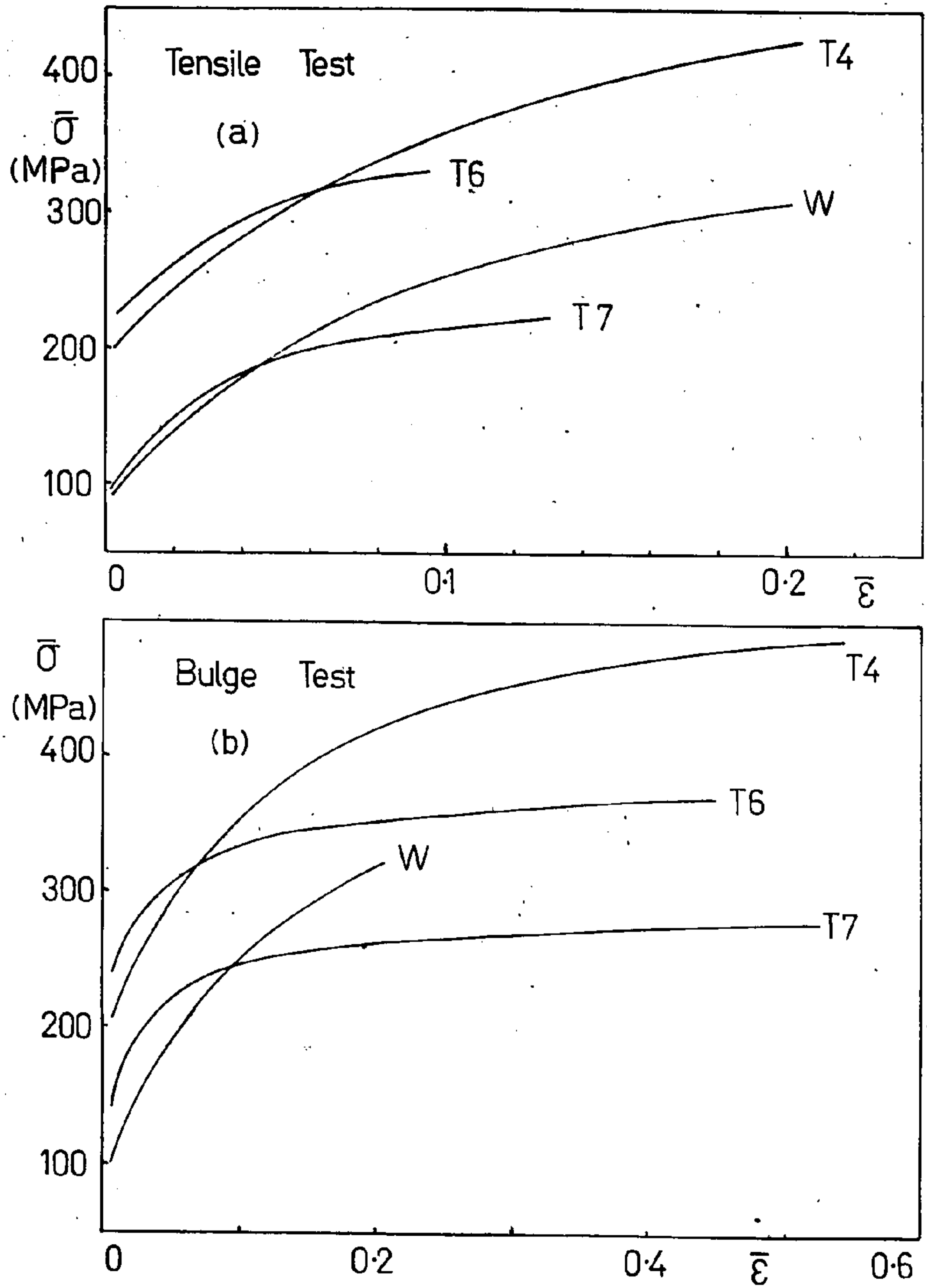

Figure 6-3 Longitudinal $\bar{\sigma}$-$\bar{\varepsilon}$ curves for 2036.

Table 6-2 gives the average tensile test parameters. In uniaxial tension, the as-quenched (W) material exhibited inhomogeneous deformation in the form of serrated yielding and the curve shown in Figure 6-3(a) represents the mean level of the serrations. In balanced biaxial tension, this same material exhibited a form of inhomogeneous deformation which caused premature failure in a region well away from the pole of the bulge. This type of failure has been reported in Al-Mg-Si alloys by Campbell et al (1979) and will be discussed later in this chapter.

It is clear from the graphs of Figure 6-3 that the materials can be divided into two groups on the basis of their work hardening characteristics. The W and T4 tempers have the same work hardening behaviour (i.e., the yield stress is controlled by distinct interaction with solute atoms or shearable particles, but the hardening is determined by dislocation accumulation in the matrix). Thus, the curves are displaced along the ordinate by the contribution to the yield stress due to the precipitation of zones. Curves for the T6 and T7 tempers are similar in shape, indicating that the operative mechanisms of work hardening and dynamic recovery are similar for both material conditions. These tempers show a greater rate of work hardening at low strains than the W/T4 tempers, but this rapidly drops to a very low value after strains of ~ 0.1. It should be noted that the T6 material is peak aged only with respect to the yield stress, the decrease in work hardening rate causing its tensile stress to fall below that of the T4 material.

Before presenting information regarding the formability of the different tempers of 2036, some observations on the types of failure which occurred during bulge testing will be noted. It was noted in

Table 6-2

Longitudinal Tensile Test Parameters

CONDITION	σ_y (MPa)	σ_u (MPa)	e_{total} (%)
2036-W	92	252	22.4
2036-T4	200	347	22.6
2036-T6	225	301	11.1
2036-T7	91	196	16.6

Table 6-3

Bulge Heights Obtained from Plane Strain Tests

Temper	Average Bulge Height (mm)
2036-W	26.5
2036-T4	25.9
2036-T6	19.2
2036-T7	23.1

Chapter 4 that the T4 material failed in a catastrophic manner either parallel or perpendicular to the rolling direction, and examples of these are shown in Figures 6-4(a) and (b). The T6 material failed in a less catastrophic manner along the rolling direction (Figure 6-4(c)), while the T7 failure was very gradual and was initiated away from the pole but also in the rolling direction (Figure 6-4(d)).

As mentioned earlier in this chapter, the as-quenched material exhibited a very unusual form of fracture which is related to the occurrence of serrated yielding in uniaxial tension. After the imposition of small plastic strains ($\sim$0.05) in biaxial loading, the sample began to deform in the plane strain region (along the side of the bulge) by the propagation of circular regions of non-uniform deformation, as shown by the arrow in Figure 6-4(e). Final failure occurred in one of the regions of localised flow well away from the pole of the sample.

The nature of the failure of the W temper material in bulge testing suggests that material in this condition may be very susceptible to failure in a plane strain loading situation. However, plane strain rigid punch tests performed on the W temper material showed an average bulge height comparable to the T4 material (Table 6-3). It is possible that the friction associated with this test acts in a manner to prevent the localisation of deformation and resulting premature failure for it is common industrial practice to form many age-hardenable aluminum alloys in the freshly quenched condition: In such cases, there are considerable friction forces acting between the sheet and the punch or die.

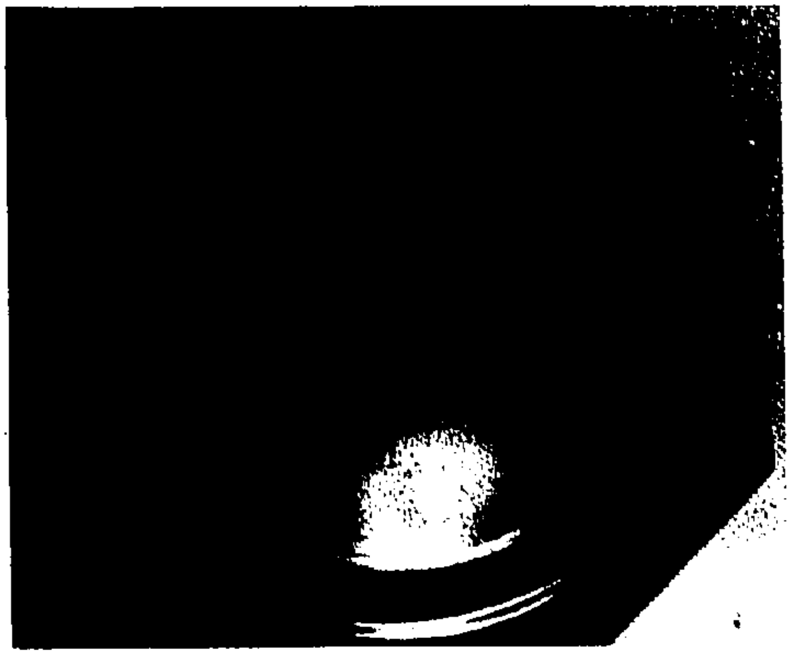

Figure 6-4(a) Bulge test failure of 2036-T4 along the rolling direction.

Figure 6-4(b) Bulge test failure of 2036-T4 perpendicular to the rolling direction.

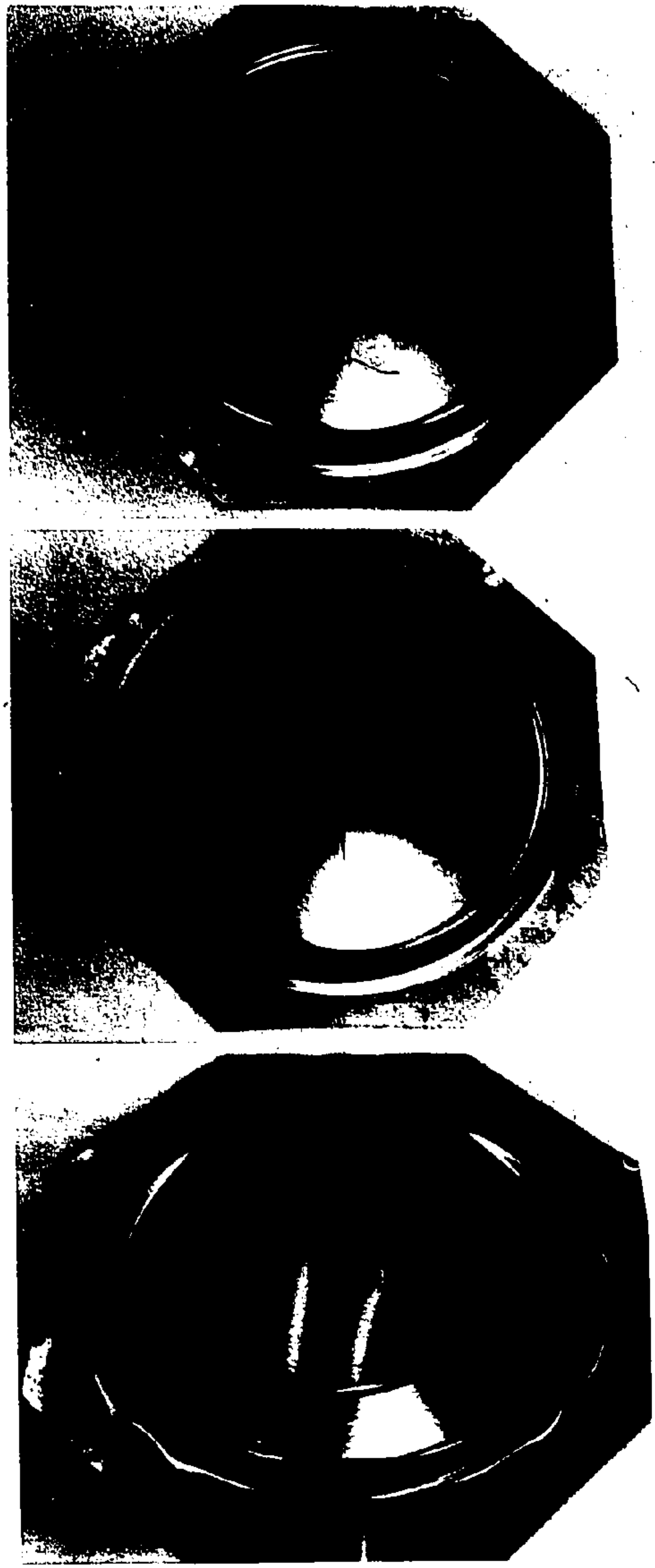

(c) 2036-T6

(d) 2036-T7

(e) 2036-W

Figure 6-4 Bulge test failures

6.3 Effect of Ageing on Formability

Approximate F.L.D.'s and fracture maps were determined for the T4, T6 and T7 materials in the manner described in Chapter 4. Only longitudinal tensile and plane strain tests were performed, and no W temper material was included in the study because it was not possible to retain a grid on the sheet during the solution heat treatment. Limit strains in equi-biaxial deformation were taken as those strains at the pole of the bulge, although for the artificially aged materials, fracture was initiated in a region of general biaxial deformation some distance from the pole.

Figure 6-5 shows that the F.L.D. for the T4 material lies above those for the artificially aged tempers over the entire range of strain space investigated. With regard to the fracture maps, it becomes necessary to divide the strain space into two regions, i.e., from uniaxial tension to plane strain tension, the level of the T4 fracture map is consistently below the fracture levels of the T6 and T7 materials. However, as equi-biaxial deformation is approached, there tends to be a clustering of the fracture levels. The levels of the fracture maps in the region of negative minor strains indicate that the post-uniform ductility of the artificially aged material is superior to the naturally aged material, although this assumes less importance to the total formability when the difference in the limit strains is so great. It is much more difficult to interpret the biaxial strain region of the diagram and further comments regarding this will be left to the discussion section of this chapter.

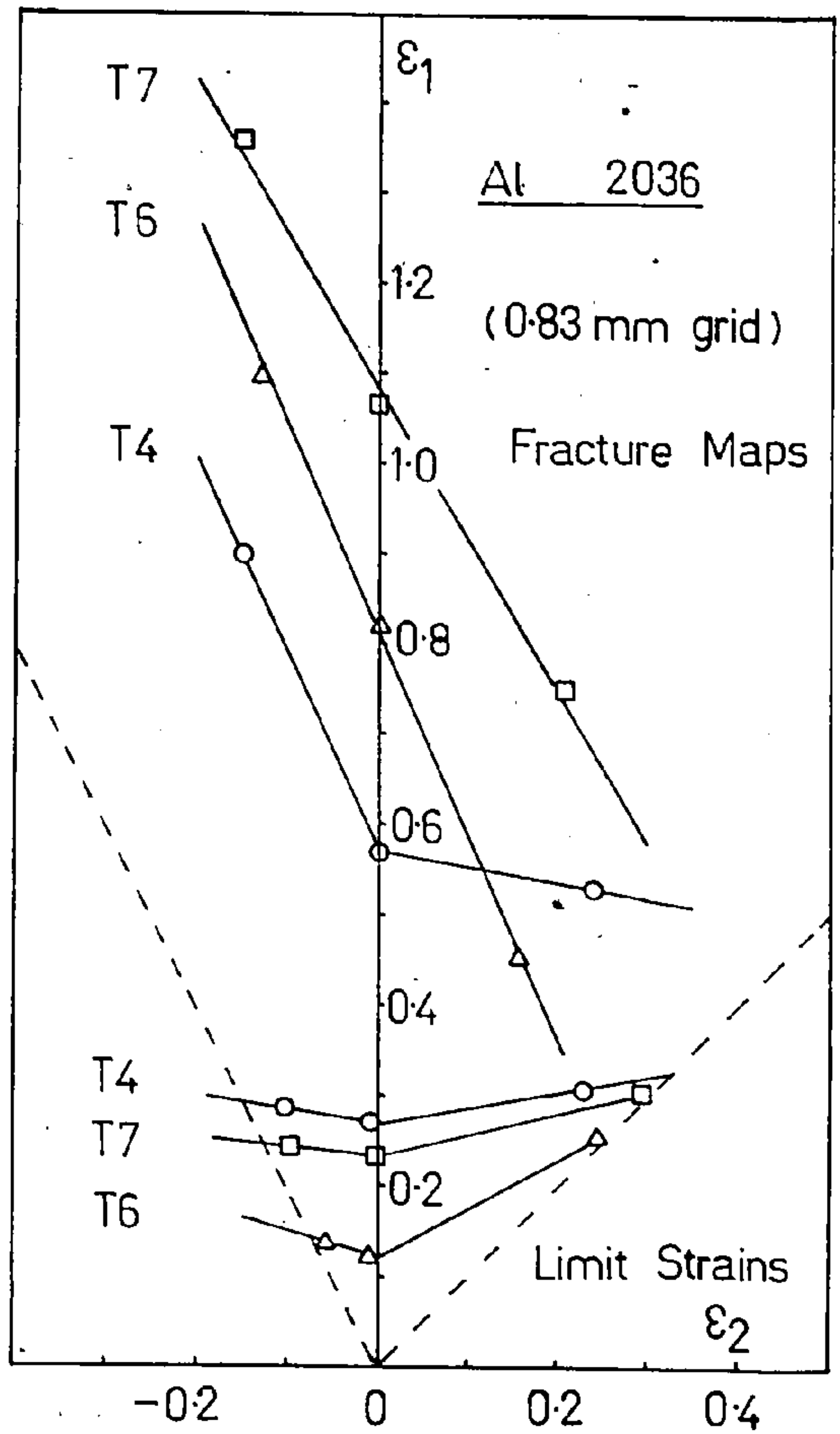

Figure 6-5 Approximate F.L.D.'s and fracture maps for the different ageing conditions of alloy 2036.

6.4 Effect of Ageing on Fracture

The general consequences of the ageing of alloy 2036 on the features of tensile fracture surfaces are illustrated in Figure 6-6 and summarised below.

- W - predominantly fibrous failure by linking of large voids nucleated at constituent particles; some evidence of fibrous shear; very little evidence of void sheets between large dimples.
- T4 - combination of intense voiding and fibrous shear; evidence of void sheets between major voids due to the presence of dispersoid particles (see also Figure 6-5).
- T6 - similar to T4 fracture but with voids of greater depth and less evidence of void sheets; some local regions of intergranular appearance.
- T7 - predominantly fibrous failure with very deep voids; matrix material appears to be very deformed with many small voids; little evidence of void sheets.

Fractures in equi-biaxial tension all exhibited macroscopic shear although details of the fracture surfaces reveal combinations of shear failure, fibrous failure, and intergranular failure dependent upon the temper. Major features of the fracture surfaces are presented in Figure 6-7. The comments regarding the details of the tensile fractures generally apply to the bulge test fractures, but some additional comments are necessary. In all bulge test failures, there is more evidence of ductile shear. Significant regions of intergranular failure appearance are present in the T6 material and these regions show numbers of small dimples

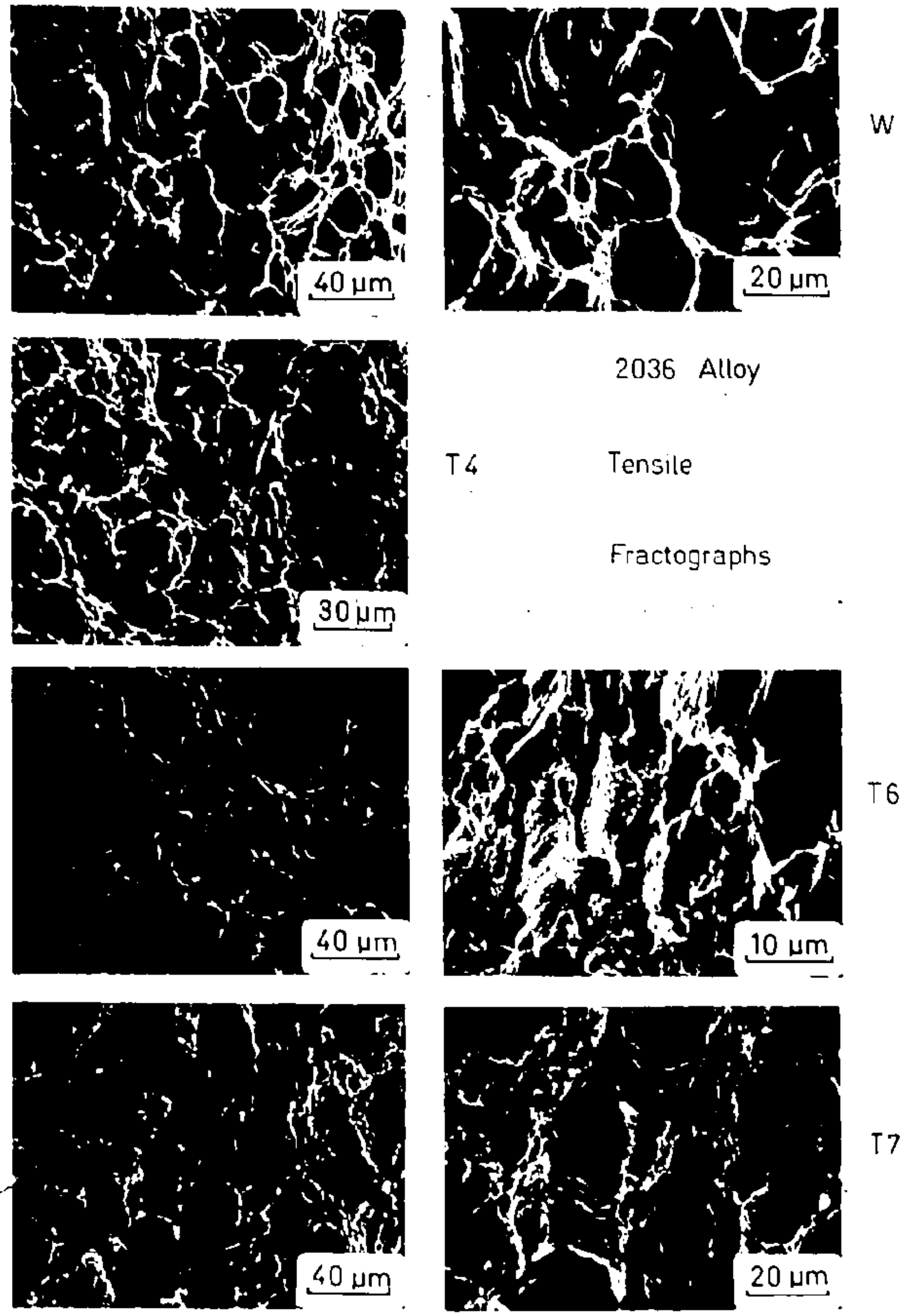

Figure 6-6 Effect of ageing on fracture surfaces in uniaxial tension deformation.

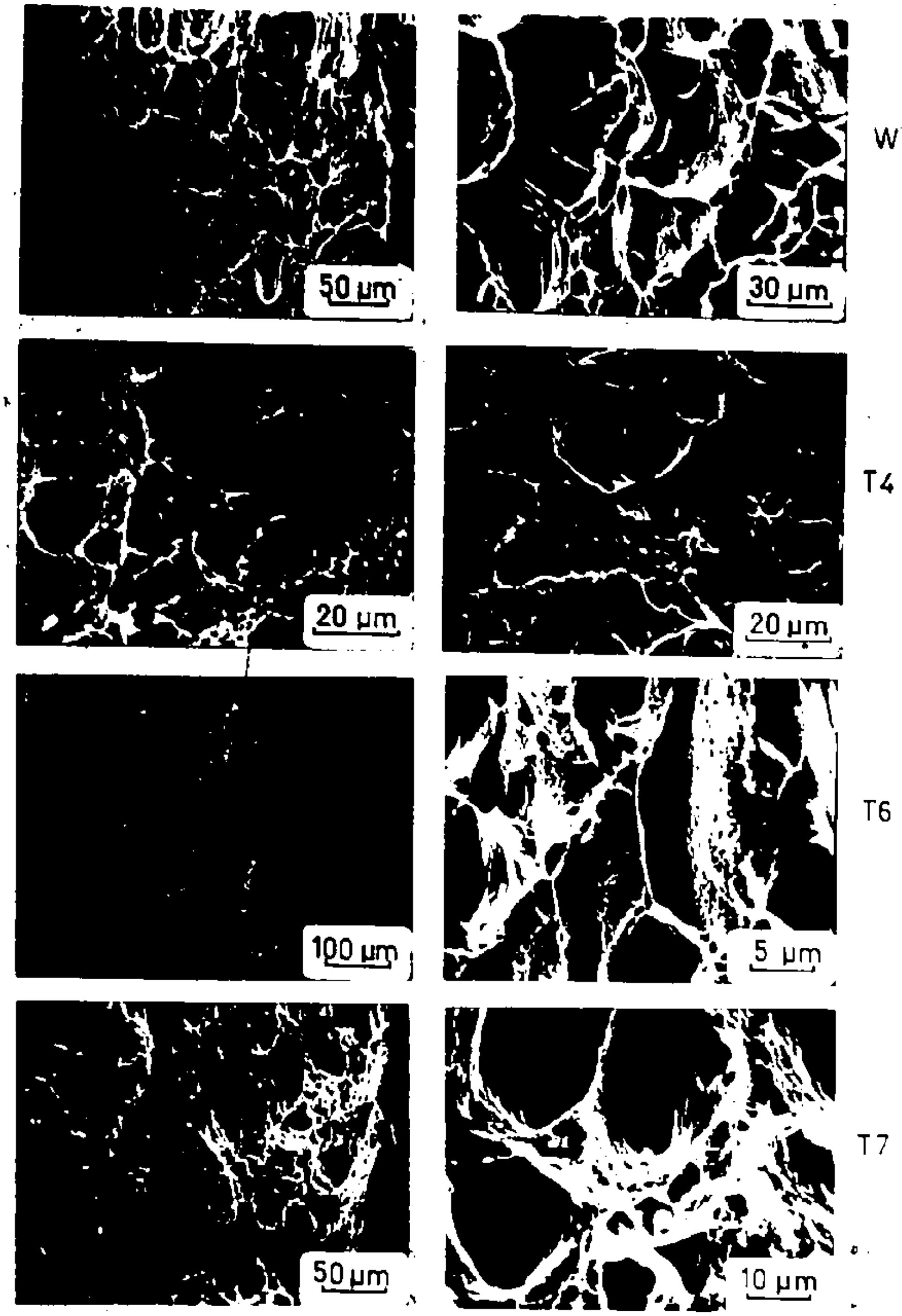

2036 Alloy Bulge Test Fractographs

Figure 6-7 Effect of ageing on fracture surfaces in equi-biaxial tension.

covering the surfaces of the intergranular facets.

The T7 fractures show very large, elongated dimples, suggesting that the void growth stage for this material is long compared to the other tempers. The material between these voids exhibits a very high density of small voids with dimensions generally less than for the void sheets in the T4 temper.

Plane strain fracture surfaces for the T4 and T7 materials were similar to those of the bulge test except that the dimensions of the voids were less in plane strain. However, some unusual features were observed on the W and T6 fracture surfaces. The W fracture surface was divided into two regions; the inner section (closest to the punch) showed a typical fibrous shear failure, while the outer section exhibited a very flat shear fracture, shown in Figure 6-8(a). Closer examination of this region, (Figure 6-8(b)), revealed no evidence of void coalescence, but showed series of fine striations parallel to the plane of the sheet. The T6 fracture surface ~~also~~ contained two major regions. Figure 6-9(a) shows a narrow region of shear similar to that in the W temper material, bounded by the typical fibrous shear/intergranular combination. Figures 6-9(b) and (c) provide more details of the transition between the two regions.

6.5 Discussion of Ageing Effects

An attempt to interpret the influence of ageing on formability must take cognisance of a variety of pieces of both complementary and conflicting evidence. This complex situation arises because one must consider the influence of both the microstructure and the state of stress

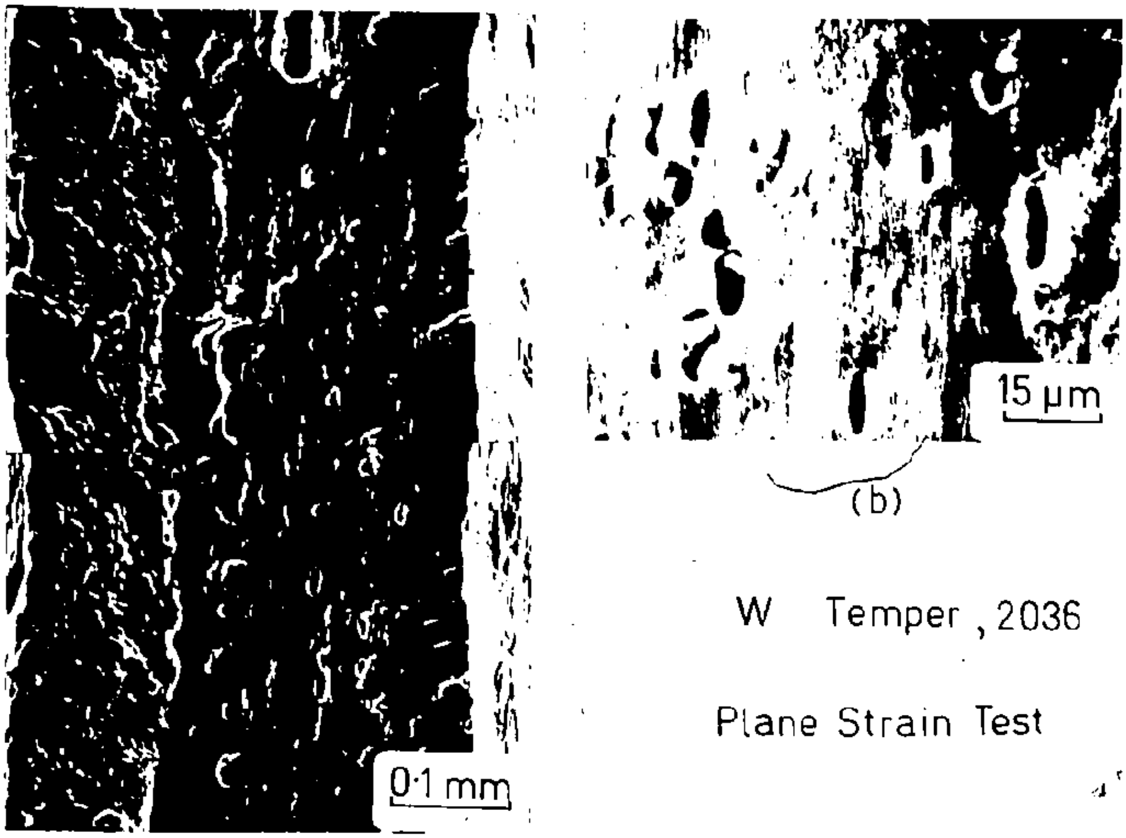

(a) (b)

W Temper , 2036

Plane Strain Test

Figure 6-8 Plane strain fracture surface of 2036-W.

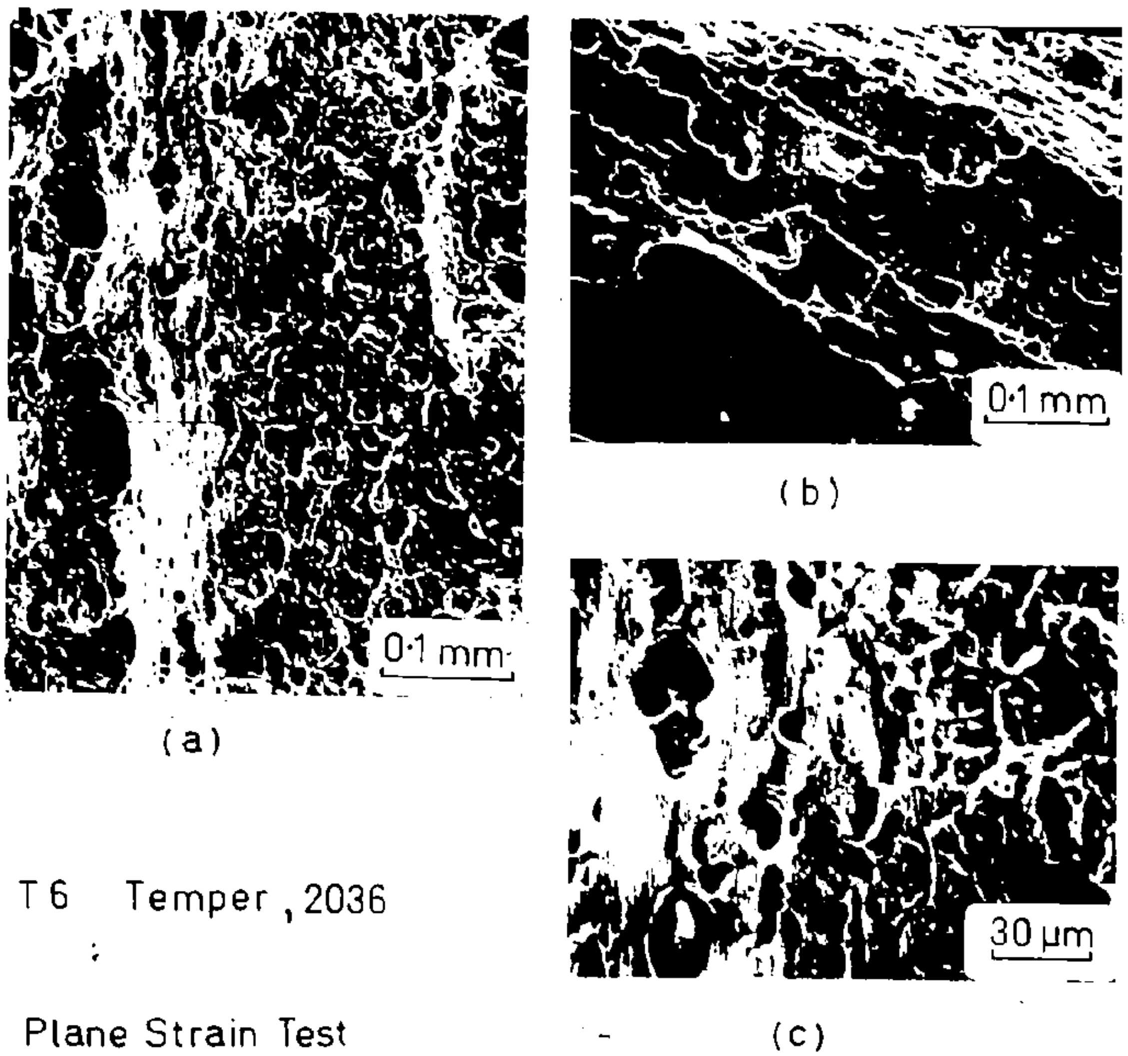

Figure 6-9 Plane strain fracture surface of 2036-T6.

on the limit strains, the fracture events, and the characteristics of the work hardening rate at large strains. Thus, one cannot simply ascribe a superior rating to a given temper, eg., T4 compared to T6 or T7, but must offer a more qualified statement indicating the basis for the comparison.

It has been established by commercial practice and is supported by the results of the present study, that the formability of the T4 temper is generally superior in stretching operations to that of the as-quenched or artificially aged materials. There are cases, however, where the annealed (extremely overaged) material performs very well, eg., the drawing of automotive bumpers. In comparing the behaviour of the various tempers in relation to their formability, it is of value to consider the ability to sustain deformation at large strains. It is important to note that the behaviour at large strains as exemplified by the bulge test data in Figure 6-3(b) or the plane strain bulge heights in Table 6-3, does not correlate well with the elongation behaviour in uniaxial tension (Table 6-2). This emphasises the difficulties of relying solely on data from tensile tests to predict the forming behaviour.

The utility of the T4 material is illustrated by the plots of work hardening rate as a function of strain (Figure 6-10(a)), based on the stress-strain curves in equi-biaxial tension (Figure 6-3(b)). Although the naturally aged material does not have the highest initial work hardening rate, it is able to sustain its hardening rate to much larger strains. However, in this type of plot, there appears to be very little difference in the behaviour of the T6 and T7 materials. Differences between these materials become apparent in plots of the work hardening rate vs. flow stress (Figure 6-10(b)), where the data is simply

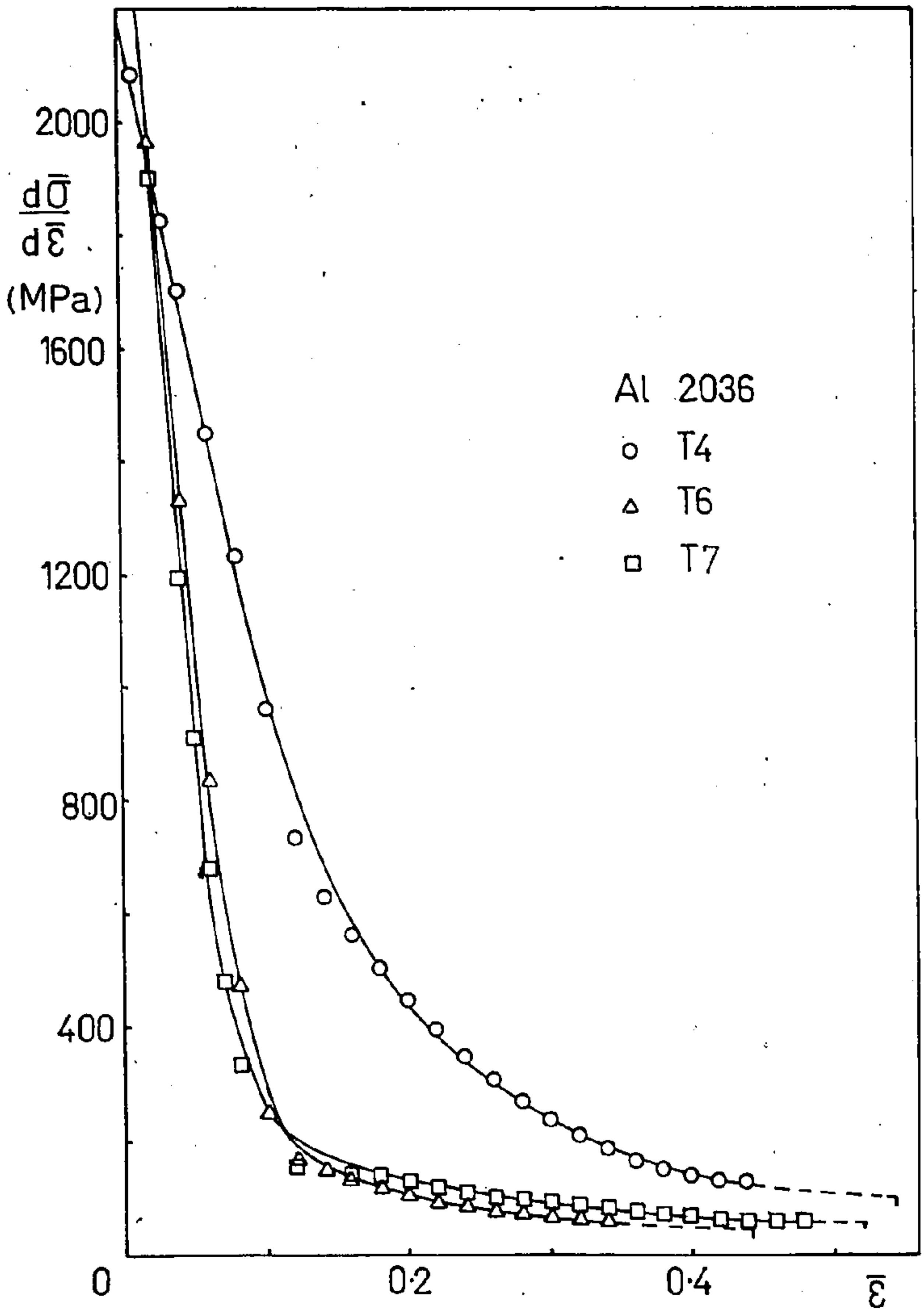

Figure 6-10(a) Work hardening rate vs strain for equi-biaxial deformation of different tempers of 2036.

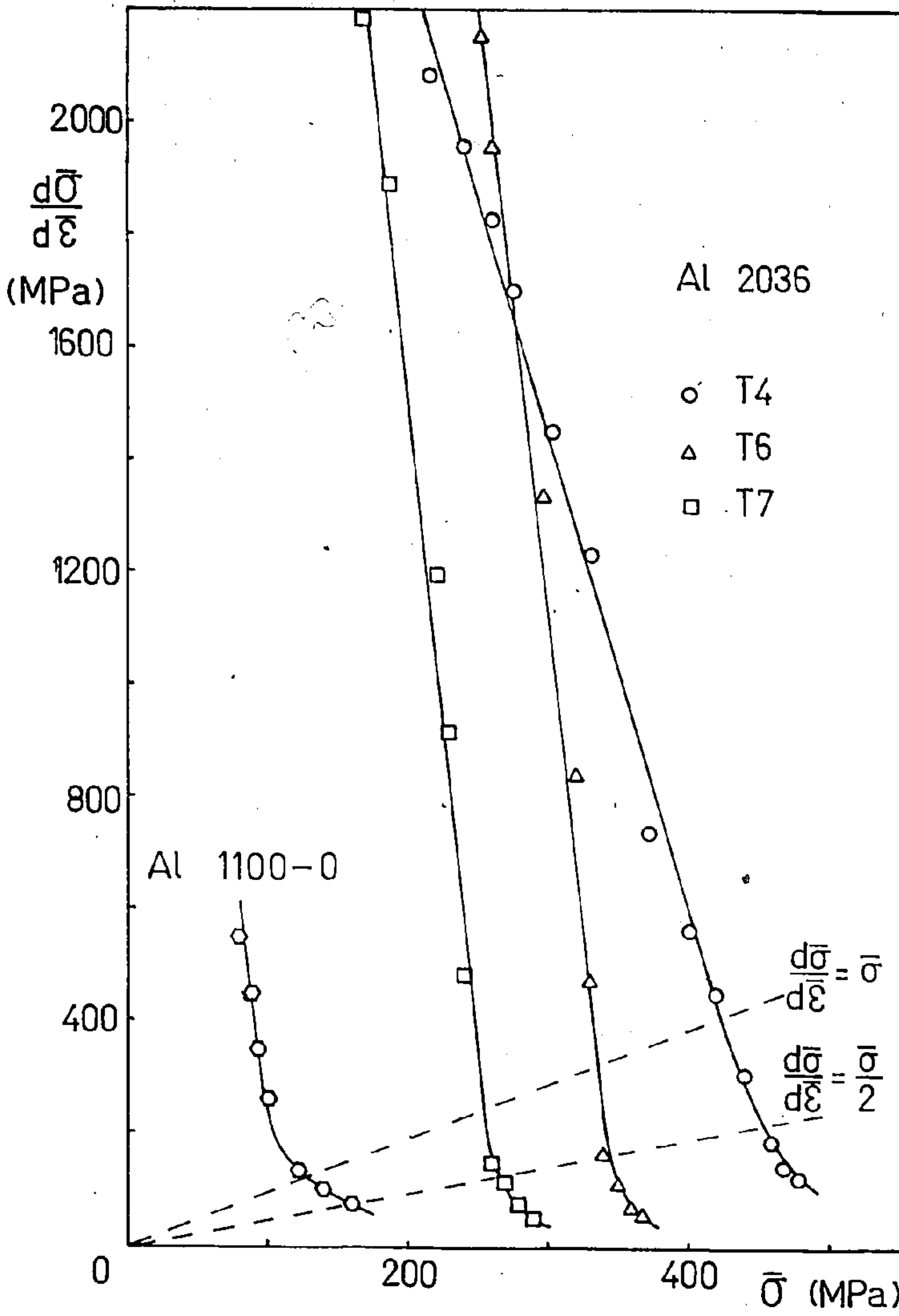

Figure 6-10(b) Work hardening vs stress.

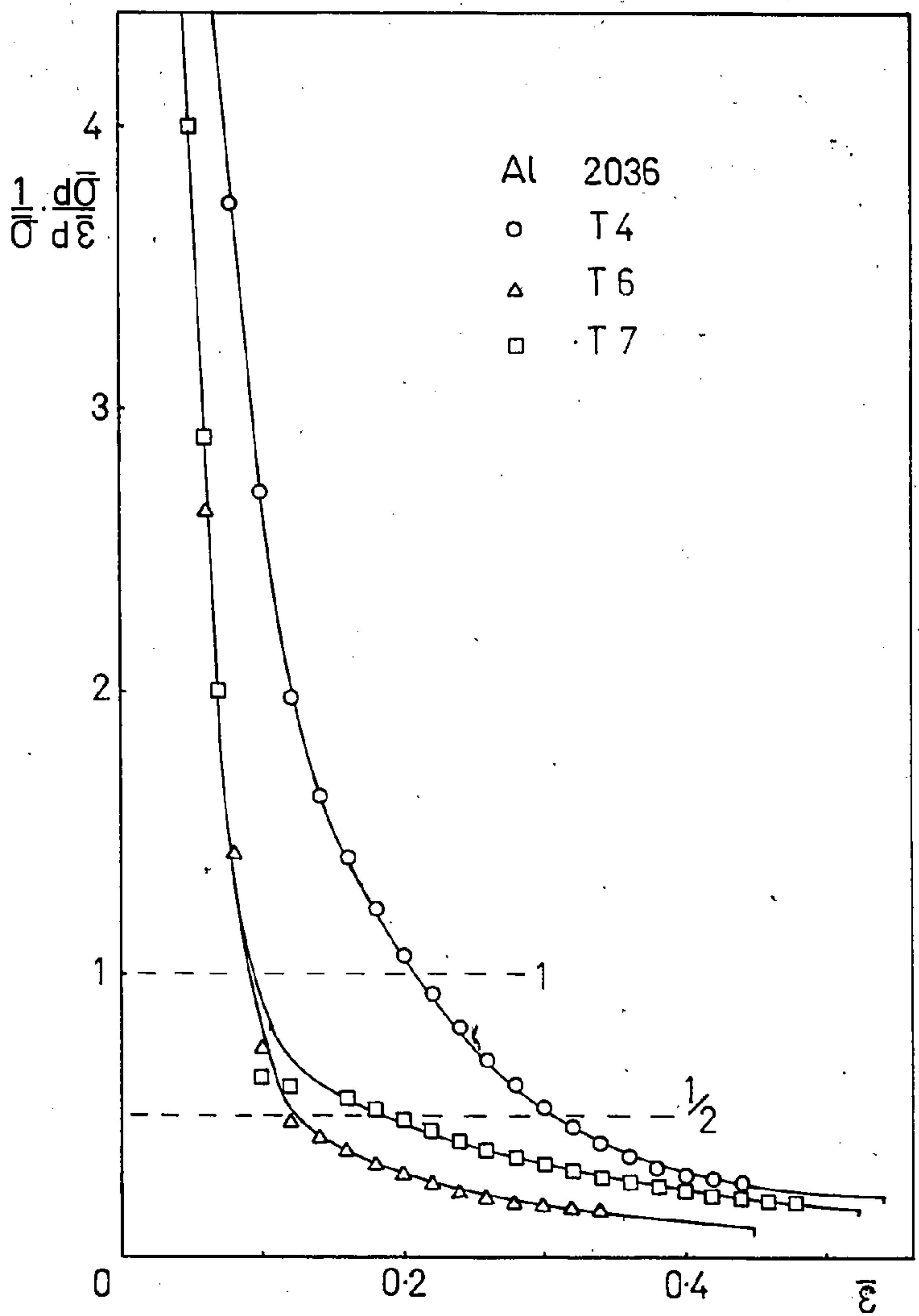

Figure 6-10(c) Normalised work hardening rate vs strain.

translated along the stress axis in relation to the initial yield stress. The similarity in work hardening rates for the T6 and T7 materials is clearly evident. Diffuse and local instability conditions expressed by the Considère and Hill conditions (Equation 2-4) are also shown on this plot.

At this stage, it is germane to consider structural explanations for the observed work hardening rates. It was mentioned in Chapter 2 that the work hardening behaviour of a material with coherent precipitates (i.e., T4 temper) should be similar to that of the matrix, and the present comparison of $\bar{\sigma}$-$\bar{\varepsilon}$ data (Figure 6-3) of the W and T4 tempers supports this. However, the work hardening behaviour of the artificially aged materials is more difficult to explain. The initial work hardening rate is high in accord with the theories of Fisher, Hart and Pry (1953), and Ashby and Smith (1960) reviewed in Chapter 2 (see also Figure 2-3), but the rapid decrease is inexplicable in terms of these theories. It is suggested that subsequent to the build-up of the "geometrically necessary" dislocations around the non-deformable precipitate particles, the particles are unable to support the local stress levels and they shear or void under increasing imposed plastic strain. Continued deformation should then occur at reduced work hardening rates comparable to that of the matrix material. The nature of the matrix in this case is expected to differ considerably from the matrix of the underaged material, especially with respect to the amount of solid solution present, and also the scale of the substructure (which influences the rate of dynamic recovery). It is reasonable to assume from the phase diagram of the Al-Cu system (Beton and Rollason, 1957-58), that the artificial ageing treatment essentially produces a matrix of commercial purity aluminum. The work hardening behaviour of 1100-0 alloy (annealed, commercial purity) in bulge testing has been replotted from Wycliffe (1977) in Figure 6-10(b), and it is seen that this is in reasonable agreement with the work hardening data for the present artifically aged materials subsequent to the initial period of deformation. The 1100-0 material shows differences in hardening approaching fracture, but this is expected because of differences in the fracture mode and mechanism.

As mentioned in the previous paragraph, there is a substantial difference in the matrices of the underaged and overaged materials which is reflected in the work hardening behaviour. It is possible to rationalise this difference in terms of the proposals of Lloyd et al (1978) regarding the influences on dynamic recovery in the matrix. The underaged materials are strengthened by solid solution (W) and by precipitation of zones (T4) both of which may reduce the efficiency of the dynamic recovery process compared to the T6 or T7 conditions, and thus maintain their levels of work hardening to higher strains.

Further information regarding the work hardening behaviour may be gained by considering plots of $\frac{1}{\bar{\sigma}} \cdot \frac{d\bar{\sigma}}{d\bar{\varepsilon}}$ vs $\bar{\varepsilon}$ as done in Chapter 5. Figure 6-10(c) shows that this representation effectively separates the T6 and T7 data at large strains and allows the relative formability in terms of the bulge heights of Table 6-3, for example, to be rationalised. It is also noted that the fracture strains are similar despite the differences in work hardening behaviour and, more importantly, the events which appear to catalyse the fracture (as illustrated by the fractography results).

The difficulty of generalising these results to include deformation under different stress states is exemplified by the F.L.D.'s and fracture maps of Figure 6-5. Increasing the work hardening capacity forces the F.L.D. to higher levels over the entire range of strain space investigated, and it has been suggested (Duncan and Bird, 1978), that a concurrent decrease in the fracture map may occur as a result of this. However, the positions of the present fracture maps indicate that the fracture of these materials is influenced by a number of additional factors, including the fracture stress (Sowerby and Sareen, 1977), the stress trajectory, and the fracture mode. Furthermore, it is possible that differences in the strain rate sensitivity of the different material tempers (Harun and McCormick, 1979) may influence the position of the fracture map via effects on the post-uniform ductility. In general, then, situations where formability is determined either fully or partially by fracture related events must be assessed with reference to a number of material variables, some of which are common to the assessment of F.L.D.'s.

It is difficult to interpret the fractographic features without T.E.M. studies of the materials in the plastic strain regime just prior to fracture. In all cases, the distribution of major dimples corresponds to the distribution of the constituent particles. However, the distribution of the minor dimples changes with the ageing condition. The as-quenched material shows very few minor dimples and these are similar in apperance to the void sheets observed in the T4 condition, indicating that the dispersoid particles are responsible for these. However, in the T6 and T7 conditions, there appears to be a further distribution of minor dimples of smaller sizes than associated with the void sheets.

The cause of these dimples is uncertain, but possible mechanisms of formation include the nucleation of voids by grain boundary precipitates, coarse matrix precipitates, and selected sites within cell walls at the edge of the precipitate-free zone, as discussed by Schwellinger (1979). It is not known at what stage in the deformation these smaller voids are nucleated, but it is possible for the case of the coarse matrix precipitates in the artificially aged material that the shearing or voiding process suggested to explain the work hardening behaviour may be an influencing factor. Further detailed studies are necessary to substantiate this proposal.

CHAPTER 7

Conclusions

Commercial age-hardenable sheet aluminum alloys are extremely complex alloy systems whose microstructural features are critically dependent upon the thermal and mechanical history of their production. Characterisation of the different 2036-T4 materials suggests that variations in the processing of this alloy, eg., chemical composition, solidification rate, solution heat treatment, etc., can produce differences in the microstructure of this alloy which, although they do not markedly influence the basic tensile test parameters routinely used in quality control, have an important influence on post-uniform deformation and fracture-related events. The significance of these events is illustrated by considering deformation modes close to plane strain tension which occur frequently during press forming operations where bending is involved. In these cases, it is likely that the press formability is related to the deformation behaviour at large strains where the competition between continued plastic flow and the localisation of strain or fracture events is more important than the flow properties which are essentially described by the traditional forming limit diagrams.

The susceptibility of these materials to failure in plane strain tension has been utilised in small radius bend tests to qualitatively discriminate between the materials on the basis of the condensation of strain into localised fracture events. Furthermore, it is apparent that the quench sensitivity of alloy 2036 influences both the localisationtion of strain (i.e., development of coarse slip), and the linking of local fracture events (due to the presence of grain boundary precipitates) during plane strain bending. This suggests that a useful index for the comparison of different materials or processing techniques may be provided by an accurate determination of the plane strain ductility.

Material behaviour at large strains, as exemplified by hydraulic bulge testing, indicates a major dependence upon the fine scale features of the microstructure (i.e., the ageing condition), but only a minor dependence on the large scale features (within the range provided by the three as-received 2036-T4 materials). The ability to sustain work hardening differs greatly between the underaged and overaged conditions of a given alloy for deformation in either uniaxial or equi-biaxial tension. This is evident in the relative levels of F.L.D.'s for the different ageing conditions. However, the relationship between the fine scale particle dispersion and the ability to sustain the work hardening rate is not clear, and further work is needed to elucidate the controlling phenomena. Fracture characteristics are seen to depend not only on the ageing condition, but also on the state and level of stress in the material prior to fracture, and the mechanism by which the fracture is catalysed. In this respect, the determination of fracture maps is useful because these allow the effects of the above variables to be presented.

APPENDIX

The Hydraulic Bulge Test

An octagonal blank is rigidly clamped at the periphery and deformed to a symmetrical dome as hydraulic pressure is applied at one side.

Due to symmetry, the state of stress and strain at the pole is:

$$\sigma_1 = \sigma_2 = \sigma \quad \text{(balanced biaxial tension)}$$

and

$$\varepsilon_1 = \varepsilon_2 = \varepsilon.$$

The pole of the specimen being equivalent to a thin spherical shell subjected to internal pressure:

$$\sigma = \frac{PR}{2t} = \frac{PR}{2t_o} \times \frac{t_o}{t}$$

where P = hydrostatic pressure (directly read),

t = current thickness

t_o = initial thickness (measured before the test).

The strain at the pole is determined from measuring the elongation of the diameter of a circle on the surface of the diaphragm concentric with the axis of the dome:

$$\varepsilon_1 = \varepsilon_2 = \ln\left(\frac{D}{D_o}\right) = \varepsilon = -\frac{\varepsilon t}{2}$$

where D_o = original diameter

D = current diameter (measured by a mechanical extensometer)

Test Procedure

Hydraulic pressure is supplied and the readings of pressure, spherometer and extensometer are taken at regular intervals, leading to the determination of current true stress - true strain point (using the expressions given) until failure of the specimen occurs.

The results can be used to generate a true stress - true strain curve over a wide range of strains as well as the corresponding constitutive equation.

REFERENCES

1. Aluminum Association, "Aluminum Standards and Data", 5th ed., 1976.

2. Ashby, M.F., Phil. Mag., 14, 1157, 1966.

3. Ashby, M.F. and Smith, G.C., Phil. Mag., 5, 298, 1960.

4. Azrin, M. and Backofen, W.A., Met. Trans., 1, 2857, 1970.

5. Beaver, P., Private communication, 1978.

6. Beevers, C.J. and Honeycombe, R.W.K., Acta. Met., 10, 17, 1962.

7. Beton, R.H. and Rollason, E.C., J. Inst. Metals, 86, 77, 1957-58.

8. Bird, J.E., Private communication, 1979.

9. Boyd, J.D., Drennan, D.C., Martin, C.J., Price, C.W., Rosenfield, A.R., Williams, D.N., Thompson, D.S., Technical Report AFML-TR-72-199, Batelle Memorial Institute, Columbus, Ohio, 1972.

10. Broek, D., in "A Study of Ductile Fracture", Ph.D. Thesis, and NLR Report TR 71021 U, 1971.

11. Brown, L.M. and Embury, J.D., Proc. 3rd Int. Conf. Strength of Metals and Alloys, Cambridge, England, 1973.

12. Brown, L.M. and Ham, R.K., in "Strengthening Methods in Crystals", edited by A. Kelly and R.B. Nicholson, Elsevier, England, 1971.

13. Bryant, A.J., J. Inst. Metals, 94, 94, 1966.

14. Bryant, A.J., J. Inst. Metals, 97, 311, 1969.

15. Byrne, J.G., Fine, M.E., and Kelly, A., Phil. Mag. [8] 6, 1119, 1961.

16. Campbell, K., Dover, I.R., Ramachandran, T.R. and Embury, J.D., Submitted to Metals Forum, 1979.

17. Chakrabarti, A.K. and Spretnak, J.W., Met. Trans. 6A, 733, 1975.

18. Chaturvedi, M.C., Chung, D.W. and Doucette, R.A., Metal Science, 34, January 1979.

19. Chin, G.Y., Hosford, W.F. and Backofen, W.A., Trans. A.I.M.E., 230, 437, 1964.

20. Chung, N., Embury, J.D., Evensen, J.D., Hoagland, R.G. and Sargent, C.M., Acta. Met., 25, 377, 1977.

21. Cooper, M. and Robinson, K., Acta. Cryst., 20, 614, 1966.

22. Datsko, J. and Yang, C.T., Trans. A.S.M.E., 309, November 1960.

23. Duncan, J.L., Private communication, 1979.

24. Duncan, J.L. and Bird, J.E., Proc. 10th I.D.D.R.G. Congress, Warwick, U.K., 1978.

25. Duncan, J.L., Kolodziejski, J. and Glover, G., Proc. 9th I.D.D.R.G. Congress, Ann Arbor, U.S., 1976.

26. Embury, J.D., in "Strengthening Methods in Crystals", edited by A. Kelly and R.B. Nicholson, Elsevier, England, 1971.

27. Embury, J.D., to be published in Proc. 1st Int. Conf. Aluminum Technology, A.S.M., Argentina, 1979a.

28. Embury, J.D., Private communication, 1979b.

29. Embury, J.D. and Nes, E., Z. Metallkde., 65, 45, 1974.

30. Embury, J.D. and Nicholson, R.B., J. Aust. Inst. Metals, 8, 76, 1963.

31. Evancho, J.W. and Kaufman, J.G., Society of Automotive Engineers, Paper #770307, 1977.

32. Fisher, J.C., Hart, E.W. and Pry, R.H., Acta. Met., 1, 336, 1953.

33. Flemings, M.C. and Mehrabian, R., in "Solidification", A.S.M., Metals Park, Ohio, U.S., 1969.

34. Foreman, A.J.E. and Makin, M.J., Phil. Mag., 14, 911, 1966.

35. French, I.E. and Weinrich, P.F., Met. Trans., 10A, 297, 1979.

36. Garrett, G.G. and Knott, J.F., Met. Trans., 9A, 1187, 1978.

37. Ghosh, A.K., Met. Trans., 5A, 1607, 1974.

38. Ghosh, A.K., Metals Eng. Quarterly, 15-3, 53, 1975.

39. Glover, G., Duncan, J.L. and Embury, J.D., Metals Technology, 153, March, 1977.

40. Goods, S.H. and Brown, L.M., Acta. Met., 27, 1, 1979.

41. Goodwin, G.M., Society of Automotive Engineers, Paper #680093, 1968.

42. Gricus, F.V. and Drittler, O.E., in "Formability Topics - Metallic Materials", A.S.T.M. STP 647, 1977.

43. Griffis, C.A. and Spretnak, J.W., J. Iron Steel Inst., Japan, 9, 372, 1969.

44. Haberfield, A.B. and Boyles, M.W., The Metallurgist, 7, 453, 1975.

45. Hahn, G.T. and Rosenfield, A.R., Met. Trans., 6A, 653, 1975.

46. Hardy, H.K., J. Inst. Metals, 82, 239, 1954-55.

47. Hart, E.W., Acta. Met., 15, 351, 1967.

48. Harun, H.J. and McCormick, P.G., Acta. Met., 27, 155, 1979.

49. Herø, H., Proc. 10th I.D.D.R.G. Congress, Warwick, England, 1978.

50. Herø, H. and Næss, S.E., Metals Technology, 264, August, 1978.

51. Hill, R., in "Mathematical Theory of Plasticity", Oxford University Press, England, 1950.

52. Hill, R., J. Mech. Phys. Solids., 1, 19, 1952.

53. Hirsch, P.B., Howie, A., Nicholson, R.B., Pashley, D.W. and Whelan, M.J., "Electron Microscopy of Thin Crystals", Butterworths, London, 1965.

54. Hirth, J.P. and Weertman, J., in "Work Hardening", Gordon and Breach,

New York, 1968.

55. Hoffman, O. and Sachs, G., "Theory of Plasticity", McGraw-Hill, New York, 1953.

56. Holl, H.A., J. Inst. Metals., 97, 200, 1969.

57. Hornbogen, E., in "Nucleation", edited by A.C. Zettlemoyer, Marcel Dekker, New York, 1969.

58. Keeler, S.P., Society of Automotive Engineers, Paper #650535, 1965.

59. Kelly, A. and Nicholson, R.B., Prog. Mat. Sci., 10, 151, 1963.

60. Kocks, U.F., Trans. Metall. Soc. A.I.M.E., 98, 76, 1976.

61. Kocks, U.F., Argon, A.S. and Ashby, M.F., Prog. Mat. Sci., 19, 1975.

62. Krafft, J.M. and Irwin, G.R., A.S.T.M. STP 381, 114, 1965.

63. leRoy, G.H., Ph.D. Thesis, McMaster University, Hamilton, Ontario, Canada, 1978.

64. leRoy, G.H. and Embury, J.D., Proc. I.C.F.4, Vol. 1, 15, 1977a.

65. leRoy, G.H. and Embury, J.D., in "Formability - Analysis, Modeling and Experimentation", Chicago, 1977b, A.I.M.E.-A.S.M., 183.

66. Lloyd, D.J., Private communication, 1979.

67. Lloyd, D.J., Sang, H., Embury, J.D., Wycliffe, P. and leRoy, G.H., Mat. Sci. Eng., 36, 35, 1978.

68. Low, J.R., Van Stone, R.H. and Merchant, R.H., NASA Tech. Rep. No. 2, Research Grant N.G.R. 38-087-003, Carnegie-Mellon University, Pittsburgh, 1972.

69. Lücke, K. and Mecking, H., in "Inhomogeneity of Plastic Deformation", A.S.M., Metals Park, Ohio, 223, 1972.

70. Marciniak, Z., "Aspects of Material Formability", Metalworking Research Group, McMaster University, Hamilton, Ontario, 1974.

71. Marciniak, Z. and Kuczynski, K., Int. J. Mech. Sci., 9, 609, 1967.

72. McClintoch, F.A., J. Appl. Mech., 35, 363, 1968.

73. Minh, H.V., Sowerby, R. and Duncan, J.L., Int. J. Mech. Sci., 17, 339, 1975.

74. Mondolfo, L.F., "Aluminum Alloys - Structure and Properties", Butterworths, London, 1976.

75. Mott, N.F. and Nabarro, F.R.N., Bristol Conf. on Strength of Solids, 1948, (Physical Society).

76. Munson, D., J. Inst. Metals, 95, 217, 1967.

77. Nabarro, F.R.N., Basinski, Z.S. and Holt, D.B., Adv. Phys., 13, 193, 1964.

78. Painter, M.J. and Pearce, R., "Instability and Fracture in Sheet Metal", I.D.D.R.G., Amsterdam, 1972.

79. Parker, B., Private communication, 1978.

80. Prakash, V. and Entwistle, K.M., J. Inst. Metals, 87, 262, 1958-59.

81. Rice, J.R. and Tracey, D.M., J. Mech. Phys. Solids, 17, 201, 1969.

82. Rogers, H.C., Trans. A.I.M.E., 218, 498, 1960.

83. Rolf, R.L. and Patrick, E.P., in "Formability Topics - Metallic Materials", A.S.T.M. STP 647, 1977.

84. Rosenfield, A.R., Metall. Reviews, 13, 29, 1968.

85. Ryum, N., Acta. Met., 17, 269, 1969.

86. Schwellinger, P., Scripta Met., 13, 497, 1979.

87. Silcock, J.M., J. Inst. Metals, 89, 203, 1960-61.

88. Sowerby, R. and Sareen, B.K., in "Formability Topics - Metallic Materials", A.S.T.M. STP 647, 1977.

89. Sperry, P.R., J. of Metals, 7, 145, 1955.

90. Staley, J.T., A.S.T.M. STP 605, 71, 1975.

91. Tadros, A.K. and Mellor, P.B., Int. J. Mech. Sci., 20, 121, 1978.

92. Thomas, G. and Nutting, J., J. Inst. Metals, 82, 610, 1953-54.

93. Van Horn, K.R., "Aluminum - Vol. I", A.S.M. Metals Park, Ohio, 1967.

94. Van Lancker, M., "Metallurgy of Aluminum Alloys", Chapman and Hall, London, 1967.

95. Van Stone, R.H. and Psioda, J.A., Met. Trans., 6A, 668, 1975.

96. Voce, E., J. Inst. Metals, 74, 537, 1948.

97. Wang, N.M. and Wenner, M.L., Int. J. Mech. Sci., 16, 135, 1974.

98. Weatherly, G.C., Ph.D. Thesis, University of Cambridge, England, 1967.

99. Wilm, A., Metallurgie, 8, 650, 1911.

100. Wilson, D.V. and Acselrad, O., Proc. 10th Congress I.D.D.R.G., Warwick, England, 1978.

101. Wilson, R.N., J. Inst. Metals, 97, 80, 1969.

102. Wycliffe, P.A., M.Sc. Thesis, McMaster University, Hamilton, Ontario, Canada, 1977.

103. Zinkham, R.E., Dedrick, J.H. and Jackons, J.H., Proc. 5th Int. Leichtmetalltagung Leoben, Austria, Aluminum-Verlag GMBH, Dusseldorf, Germany, 1968.